Design and Experimental Verifications of a Low Power Ferroelectric-Based Structural Health Monitoring System on Hot Spot Applications

Yih-Yan Lin

A dissertation
submitted in partial fulfillment of
the requirements for the degree of

Doctor of Philosophy

University of Washington
2014

Reading Committee:
Minoru Taya, Chair
I.Y. (Steve) Shen
Yasuo Kuga

Program Authorized to Offer Degree:
Mechanical Engineering

University of Washington

Abstract

Design and Experimental Verifications of a Low Power Ferroelectric-Based Structural Health Monitoring System on Hot Spot Applications

Yih-Yan Lin

Reading Committee:
Minoru Taya, Chair
I.Y. (Steve) Shen
Yasuo Kuga

A new structural health monitoring (SHM) system, which consists of a piezoelectric drive and a ferroelectric-based sensor unit, is proposed. Unlike the current SHM system, the proposed SHM system has only a sensor unit and a drive unit, a low-power source to operate the system, and requires no heavy weight memory unit to record data.

For the ferroelectric-film-based sensor unit, a polarization fatigue measurement system is developed and a numerous sets of polarization fatigue tests on ferroelectric films with millions of repetitions are conducted. The polarization fatigue data of the ferroelectric thin films provide the reduction of their polarization under a certain number of cyclic electric fields. For the drive unit, a bulk piezoelectric ceramic is mounted on a structural component sending out voltage, which is induced by the deformation on the structural component. By electrically connecting the drive unit to the sensor unit and an interface circuit in between, we utilize the polarization fatigue data of ferroelectric-film-based sensor unit to record only a critical number of cycles of a dynamic load history of larger magnitudes. The proposed SHM system is verified by a numerous sets of random-amplitude dynamic tests, which demonstrate that the proposed SHM system performs reliable accuracy for counting cycles, whose amplitude is larger than a specific value.

To protect the fragile piezoelectric ceramic based drive unit, we analyze the reduction of stress if the piezoelectric patch is mounted on a structural component with an adhesive layer in between. We develop a theoretical model to analyze the elastic and viscoelastic behaviors of the load transfer design statically as well as dynamically. Finite element analysis is conducted to verify the accuracy of the theoretical model.

Table of Contents

List of Figures

List of Tables

Chapter 1 Introduction

Most structural failures in engineered system result from cyclic mild conditions of variable stress, strain, or temperature rather than a single intense shock of excitation. It is well-recognized that a catastrophic failure occurs after a large number of mild load cycles where a single load of the same magnitude would not do any harm to the mechanical components. The aging of aerospace structures due to alternative loading has been the one of the major threats to aviation safety. From decades ago, the United Airlines Flight accident induced 111 fatalities in 1989 [1], up to recent years where the China Airlines flight accident caused all 225 fatalities in 2002 [2]. Recently, in the Fukushima nuclear plants in Japan, the Tokyo Electric Power Company did not have the information on which structural components were damaged and the magnitude and number of cycles of such stress loading on them. This prevented them from performing the swift actions needed to avoid meltdown.

In chapter one, the literature about the development of structural health monitoring (SHM) system will be reviewed in Sec. 1.1, the proposed SHM will be briefly introduced in Sec. 1.2, and the structure of this dissertation will be organized in Sec.1.3.

1.1. Literature Review

Since the first mechanical fatigue phenomenon was discovered in 1837 [3], there have been continuing efforts to develop the analysis technique that predicts the remaining life of the structure due to the fatigue [4][5], and damage assessment to evaluate how much the strength reduced because of the fatigue [6][7][8], which are well-established but still being employed in present days. For practical tests to inspect the damaging defects, non-destructive testing (NDT) and evaluation methods are widely used in industry for checking the quality of a mechanical component. A series of inspection instruments and techniques have been evolved to serve NDT, which provides an accurate evaluation on the location and size of the defect. However, the need for quick and real-time inspection is sacrificed due to the requirement of human intervention, the investigations of the damage might affect even disable the function of the material. The generalized measurement system which provides real-time inspection consists of detector stage, which senses the physical signals, a signal conditioning stage, which amplifies the relatively small signal and filters out noises from the detectors, and the displaying-recording stage, which interprets and stores the data from the previous stage. A typical example of the measurement system composed of strain gauges to sense the strain on a structural component as the detector stage, an instrumentation amplifier and frequency filter as a signal conditioning stage, and a monitor and a hard disk drive as the final stage. Unlike NDT, which diagnoses the material failure after usage, the evolving structural health monitoring (SHM) systems expanded from the limited function of the typical measurement system, including a real-time sensing, data acquisition and data interpretation system, system has been proposed and developed for decades to serve engineers to evaluate the current conditions of a mechanical component and estimate the expected life of it. The SHM systems use an automatic technique to reduce or even eliminate the amount of human intervention, which enable the on-board system to function while the machine is operating, whereas traditional NDT are typical grounded-based technique. An ideal SHM system, integrated with sensor/actors, signal processing, and computation components, aims to diagnose or even prognose “the state of health” of the material or structural component in every moment during the life of a ground/aero vehicle, any structure of civil infrastructure or energy-generating system (wind turbine blades and nuclear power stations) [9]. Many sensing techniques are used to achieve the monitoring [10]. The current SHM systems can be roughly classified into the following families: vibration-based, impedance-based, fiber-optics-based, and piezoelectric-based SHM.

The premise of the vibration-based SHM is that the damage of the structural component induces the changes in structural characteristics, such as mass, stiffness, damping as well as boundary conditions. The variations of these structural characteristics affect the vibration response of the structure, such as natural frequencies [11], frequency response function [11], mode shapes [12] and its derivative [13] ,or flexibility coefficients [14][15][16], etc. By inspecting the shift of these vibration responses and back calculate the inverse problem, the changes of the structural characteristics can be identified and how serious the structural component has been damaged can be evaluated. Pandey *et al.* [12] first introduced the concept of mode shape curvature to localize the damage. They applied a continuous beam model to a simply supported beam containing damaged parts at several locations to demonstrate the presented method. As an extension of this work, Ho and Ewins [17] presented changes in the mode shape slope squared as damage indicating features. As another damage indicator based on mode shapes, Pandey *et al.* [18] presented the changes in the dynamically measured flexibility matrix can be accurately estimated from a few low frequency vibration modes of the structure. To determine the best candidates of damage signatures, including natural frequencies, mode shapes, and modal flexibility, Zhao and DeWolf [19] presented a sensitivity study, and made a conclusion that modal flexibility was more likely to indicate damage than the other candidates. Subsequent study presented by Bernal and Gunes [20][21] incorporated in modal flexibility matrices into the damage locating vector method to localize damage. To achieve a well-performed evaluation by vibration-based SHM requires well-equipped dynamic analyzer and appropriate algorithms for signal processing, such as Fast Fourier Transform or wavelet transform, to condition the raw signals to meaningful information. The more accurate evaluation of the structure may lead to higher cost and bulky equipment.

Fiber-optic based SHM embeds optical fibers in the composite materials. The fabricated Bragg gratings on the optical fiber are able to transmit a wavelength shift due to the crack to the data acquisition and computation system to demodulate the signals[22][23][24][25][26]. The fiber can be deployed along the structural component to monitor strain at various locations, or embedded in manufactured parts, such as composite components. Fiber optics sensors have advantages of nonintrusive features on the order of human hair in diameter, extremely lightweight, their immunity to electromagnetic interference, and proven to be robust [27]. The accuracy of the strain measurement can also be enhanced by forming the fiber into rosettes [28]. However, fiber optics sensors are sensitive to thermal effect and required thermal insulation and temperature compensation design. The data acquisition, signal modulation / demodulation, and computation of the received optical information is a critical issue that may complicate the system and lead to high cost.

SHM system with piezoelectric sensors/actuators, in general, emits elastic waves through the structure by a piezoelectric patch. The responses of structure due to the appearance of crack from a defect are measured by an array of the other piezoelectric patches. Tracking the changes in reflection and transmission velocity as well as wave attenuation are able to locate the possible location of the defects and evaluate the possible degree of damage. The damaged material can be imaged by analyzing the responses of the Lamb waves so that several signal processing and algorithms for analyzing the signal were developed. Ing and Fink [29] were the first to present the time-reversal Lamb waves to diagnose damage of a structural component. Lin *et al.* [30] and Giurgiutiu *et al.* [31] generated the Lamb waves with piezoelectric wafer active sensors (PWAS), mounted on the surface of the structure to provide inexpensive, non-intrusive, and minimal invasion to the devices. To analyze the responses of the driven Lamb waves, signal processing and imaging method are also critical issues. Wang *et al.* [32] investigated the applicability of the time-reversal concept of Lamb waves in plate-like structures both theoretically and experimentally, and proposed imaging method to represent damage in the plate structure from the signals extracted from the time-reversal Lamb waves. Recently, a Lamb wave mode decomposition method developed by Yeum *et al*. [33] and Alexander *et al*. [34] subsequently, adopting ring or annular shape of transducers, is presented to allow transduces operate in multiple frequency range.

Electro-Mechanical Impedance (EMI)-based SHM system is first proposed by Liang *et al.* [35]. In the EMI technique, a piezoelectric patch bonded on the surface of the structural component acting as an actuator is actuated harmonically by high frequency electric field, and produces a structural response to the monitored structural component. The other piezoelectric patch on another location of the surface of the structural component acting as a sensor, receives the mechanical impedance of the structural component, which is directly related to the electrical impedance (or electrical admittance) of the PZT. The mechanical impedance response of the structural component driven by the piezoelectric patch harmonically is function of mass, damping, stiffness, as well as boundary conditions (BCs) of the structural component. The change of the impedance is a signature of flaws in the structural component resulting to changes of mass, damping, stiffness of the mechanical model of the structural component. Subsequent to Liang’s work, Sun *et al.* [36] then experimentally used electrical impedance method to acquire FRF for a single location and to transfer frequency response function between two locations on a structure [37]. This technique and its applications have been proven effective in experiments, including aircraft structures [38], civil structural components [39] and concrete structures [40]. Park *et al.* [41] developed a wave propagation approach to evaluate the state of the structure. Park et al characterized the damage in the structural component by analyzing the frequency response function and modal data of the structure. Park *et al.* [42] summarized future issues of the mechanical impedance method from both hardware and software standpoints. Impedance methods continue to attract the attention of researchers and engineers to either improve the measuring devices or develop the damage-identification algorithms. In order to miniaturize the bulky impedance-measuring device, Pecairs *et al.* [43] developed an operational amplified-based device to record electrical impedance of a PZT patch and its performance has been demonstrated. Park *et al.* [44] develop an auto-regressive model combined with the active-sensing mechanical impedance method to statistically identify the damage of a structural component. The issues that EMI-based SHM has to be improved include the difficulties in handling the fragile PZT sensors and in bonding them to the structure, typically the bulky and expensive analyzers required for impedance measurement, the complexities of acquiring and processing data in large-scale complex structures, and high power consumption.

1.2. Proposed Structure Health Monitoring System

Although the development of SHM is greatly improved recently, in accuracy of the localization of damage, responding time, etc., the current families of SHM systems, no matter if they employ vibration-based, fiber-optics based, or EMI based technique, they are bulky and required a sensor system to transfer various types of physical parameters to electric signals, a data acquisition system to collect these electric signals into the memory, a memory system to store the data, a computational system to analyze the data, and a power system to operate the whole system. These techniques might be precise and accurate enough for a detailed diagnosis but they carry a lot of weight for the power and memory system. Some of the techniques, optical fiber based SHM for example, are difficult to reduce the cost of the optical fibers sensors and demodulation system for current technology. Therefore, we propose a SHM system enables to record the critical information of the loading history on a structure [45][46]. This innovative device performs two major characteristics. First, it collects critical data only and ignores trivial loading information. Second, it is a low-power-consumption device with almost zero-weight of ferroelectric thin film based sensor, which are both important breakthroughs for the current loading history recording devices.

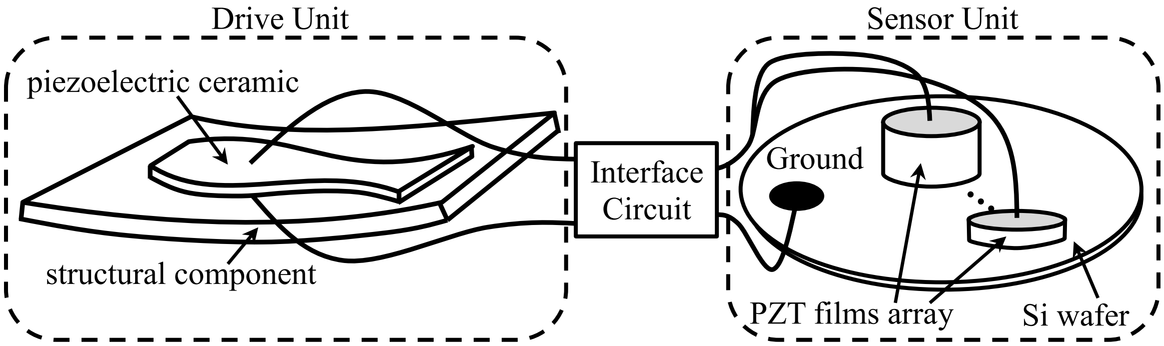

Figure 1-1 Structural Health Monitoring

1.3. Organization of the Dissertation

The content and structure of this dissertation is arranged as follows:

In chapter one, we present the motivations of this research, the literature review of several types of SHM system that are in majority of applications, and the proposed SHM system, which is able to achieve low lost and weight but still perform a certain accuracy.

In chapter two, we present a literature review of piezoelectric sensors and the theoretical background, which is the drive unit of proposed SHM system. Based on the theoretical model, equivalent circuit models are presented and verified experimentally. Finite element simulations for the dynamic behaviors of drive unit are also performed to double verify the theoretical predictions and experimental results of the drive unit.

In chapter three, we present a literature review of the polarization fatigue in ferroelectric thin films, which is how the sensor unit of proposed SHM system function. The fabrication process of the proposed sensor unit is introduced thereafter. To conduct polarization fatigue measurement, the each part of the measurement system is presented in detail and the experimental results of the polarization figure of sensor units are shown in the end of chapter 3.

In chapter four, we present the interface circuit that enables a more accurate performance of the proposed SHM system. The proof-of-concept of experimental results and their analyses are presented thereafter.

In chapter five, we present the analyses of load transfer design, which is designed to protect the piezoelectric ceramic based drive unit from fracture. Both elastic and viscoelastic as well as static and dynamic analyses are performed. To verify the close-form solutions, finite element analyses by using commercial software are conducted and show good agreement.

In chapter six, we summarize the work that this dissertation has achieved and point out a direction to improve the proposed SHM system.

Chapter 2 Characteristics of Piezoelectric Materials

The prefix piezo- in the word piezoelectrics originated from Greek means pressure. The term piezoelectrics, combined piezo- and electrics, implies the nature of piezoelectric materials - the reciprocal relationship between mechanical and electric field. The discovery of the piezoelectric effect is contributed mainly by Pierre and Jacque Curie in 1880 [47], who demonstrated this special effect by crystals, such as quartz, tourmaline, or Rochelle salt. In general, for piezoelectric materials, a mechanical deformation of a piezoelectric crystal induces electrical dipoles within the material wiggled with respect to the motion, generates electrical charges clustered on their surfaces, and induces electric field, called converse piezoelectric effect; the mainly application (as well as the drive unit of proposed SHM system) of converse piezoelectric effect are sensors. On the contrary, an external electric field applied on a piezoelectric solid re-orients the electrical dipoles within the materials and induces mechanical deformation, named direct piezoelectric effect; the mainly applications of direct piezoelectric effect are actuators.

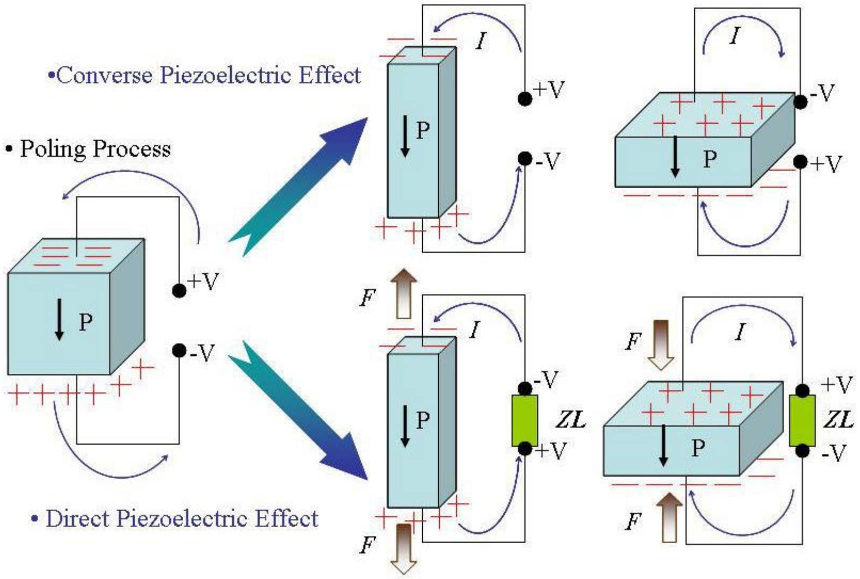

Figure 2-1 Direct and converse piezoelectric effect

In this chapter, we first review the literatures about the research of piezoelectric energy harvesters, since the drive unit of the proposed SHM basically transfers mechanical energy to electrical energy, which is what the typical piezoelectric energy harvester does. Next, we introduce the constitutive equations of piezoelectric materials. Then, the governing equation of output voltage from a piezoelectric patch mounted on a beam based on the constitutive equations and the electric circuit equation will be derived. The governing equation of the output voltage can then be graphically translated to current-source and voltage-source equivalent circuit models. The frequency response function of the output voltage can then be derived based on the coupled constitutive equations and coupled electric circuit equations. To verify the derived theoretical model, the experiments and finite element analysis of the drive unit output will be conducted, which show agreement to theoretical model, experiment results, as well as finite element simulations.

2.1 Literature review

A piezoelectric energy harvester is typically a device with one or two piezoelectric layers mounted on the surface of a cantilever beam and a proof mass at the beam tip to enhance the vibration. The energy harvester beam is usually located on a vibrating host structure and the dynamic strain induced in the piezoelectric layers generates an AC voltage output across the electrodes coating on the top and bottom surfaces of piezoelectric layers. The mathematical model for energy conversion was first developed by William and Yates [48] and the subsequent work presented by Amirtharajah and Chandrakasan [49], who considered the energy conversion device as a single-degree-of-freedom (SDOF) model and used lumped parameter modeling to analyze electromagnetic transductions of energy conversion. Glynne-Jons *et al.* [50] were the first to apply the SDOF model to the piezoelectric vibration-powered microgenerator and analyzed the energy of the system. Based on the SDOF model that Glynne-Jons *et al.* [50] developed, Roundy *et al*. [51] coupled the mechanical equilibrium to the electric loop equations through piezoelectric constitutive equations [52], and built up an equivalent circuit model to analyze the energy conversion device. duToit *et al.* [53] applied Hamilton's principle and employed variational principle to analyze the output power of the energy harvester. The SDOF modeling provides an insight to the response at a single resonant frequency and the corresponding vibration mode by simple expressions.

To further investigate the aspects of the physical system, such as mode shapes, stress/strain distributions, as well as the electrical response. Lu *et al.* [54] applied Euler-Bernoulli beam theory and piezoelectric constitutive equations to obtain vibration mode shapes which give the electric displacement to relate the electric outputs corresponding to the specific mechanical mode shape. However, this model was oversimplified and piezoelectric backward coupling effect, which dominates the inaccuracy in the off-resonant frequencies.

Erturk and Inman [55] presented clarifications and corrections to the SDOF models as well as the oversimplified distributed parameter modeling of the cantilever beam based energy harvester. Erturk and Inman [56][57] presented their subsequent research considering the backward piezoelectric coupling and using convergent series of orthogonal eigenfunctions to perform modal expansion. Such mathematical models are able to estimate the transient response by modal expansion and the response for arbitrary excitation frequencies away from resonant frequencies. The design of shape and location of the electrodes are also involved in their research.

2.2 Piezoelectric Constitutive Equations and Material Constants

The behavior of a piezoelectric material can be described by four sets of constitutive equations expressed in IEEE index notations [52].

$$\begin{cases} T_p = c^E_{pq} S_q - e_{kp} E_k \\ D_k = e_{kq} S_q + \varepsilon^S_{ki} E_i \end{cases} \qquad (\text{2-1- a, b})$$

$$\begin{cases} T_p = c^D_{pq} S_q - h_{kp} D_k \\ E_k = -h_{kq} S_q + \beta^S_{ki} D_i \end{cases} \qquad (\text{2-2- a, b})$$

$$\begin{cases} S_p = s^E_{pq} T_q + d_{kp} E_k \\ D_k = d_{kq} T_q + \varepsilon^T_{ki} E_i \end{cases} \qquad (\text{2-3- a, b})$$

$$\begin{cases} S_p = s^D_{pq} T_q + g_{kp} D_k \\ E_k = -g_{kq} T_q + \beta^T_{ki} D_i \end{cases} \qquad (\text{2-4- a, b})$$

where T_p and S_p denote the mechanical stress and strain; E_k and D_k represent the electric field and the displacement (or charge density). The mechanical, electrical, and piezoelectric constants determine the relation between material parameters of these physical properties. The relationships between stress and strain are determined by the mechanical stiffness c_{pq} and the mechanical compliance s_{pq}. The relationships between electric fields and electrical displacement are determined by impermittivity matrix β_{ki} and the permittivity matrix (or dielectric matrix) ε_{kp}.For piezoelectric constants, d_{kp}, e_{kp}, g_{kp} and h_{kp} are the piezoelectric strain/charge, stress/charge, strain/voltage, and stress/voltage constants, which connect the relationships between electrical (electrical fields E_k and electrical displacement D_k) and mechanical (stress T_p and strain S_p) properties. The subscripts i, k=1~3 and p, q =1~6, which follow the IEEE index notation. The superscripts '*E*' and '*D*' indicate that the electric field and electrical displacement (charge density) are held constant.

Each one of the (a) sets of equations in Eqn.(2-1- a, b) to Eqn.(2-4- a, b) are actuator equations and identical to each other; each one of the (b) sets of equations in Eqn.(2-1- a, b) to Eqn.(2-4- a, b) are sensor equations and identical to each other as well. That is to say, selecting any one of the (a)'s equations and any one of the (b)'s equation in Eqn.(2-1- a, b) to Eqn.(2-4- a, b) could be a complete pair of sensor/actuator equations to describe the behavior of piezoelectric materials.

For the mechanical and electrical constants, the relationships can be expressed in the form of reciprocity as

$$\begin{array}{ll} [s_{pq}^{D}]^{-1} = [c_{pq}^{D}]^{-1} & [s_{pq}^{E}]^{-1} = [c_{pq}^{E}]^{-1} \\ [\varepsilon_{ki}^{T}]^{-1} = [\beta_{ki}^{T}]^{-1} & [\varepsilon_{ki}^{S}]^{-1} = [\beta_{ki}^{S}]^{-1} \end{array}, \tag{2-5}$$

which are identical to the ones typically formed in theory of linear elasticity and electromagnetics.

Table 2-1 The definitions of piezoelectric constants and the relationships between these constants.

Piezoelectric constant	Definition		Relationship
d_{kp}	The ratio between the induced strains S_p while applying an external electric field with constant stress E_k^T.	$\frac{S_p}{E_k^T}$	$d_{kp} = e_{kq} s_{qp}^E$
	The ratio between the induced electrical displacement D_k while applying an external stress with constant electric field T_p^E.	$\frac{D_k}{T_p^E}$	$d_{kp} = g_{ip} \varepsilon_{ki}^T$
e_{kp}	The ratio between the induced stresses T_p while applying an external electric field with constant strain E_k^S.	$\frac{T_p}{E_k^S}$	$e_{kp} = d_{kq} c_{qp}^E$
	The ratio between the induced electrical displacements D_k while applying an external strain field with constant strain S_p^E.	$\frac{D_k}{S_p^E}$	$e_{kp} = h_{ip} \varepsilon_{ki}^S$
g_{kp}	The ratio between the induced strains S_p while applying an external electrical displacement field with constant stress D_k^T.	$\frac{S_p}{D_k^T}$	$g_{kp} = h_{kq} s_{qp}^D$
	The ratio between the induced electrical fields E_k while applying an external stress with constant electrical displacement T_p^D.	$\frac{E_k}{T_p^D}$	$g_{kp} = d_{ip} \beta_{ki}^T$
h_{kp}	The ratio between the induced stresses T_p while applying an external electrical displacement with constant strain D_k^S.	$\frac{T_p}{D_k^S}$	$h_{kp} = e_{kq} s_{qp}^E$
	The ratio between the induced electrical fields E_k while applying an external strain with constant electrical displacement S_p^D.	$\frac{E_k}{S_p^D}$	$h_{kp} = e_{kq} s_{qp}^E$

2.3 Coupled Electrical Circuit Equation of Drive Unit

The drive unit of the proposed SHM system, which transfers mechanical excitations (stress or strain) into electrical signals (electric field, voltage or current), is designed as a piezoelectric laminate attached on the surface of the hot spot on a host structural component. The mechanical energy of the structural component can be transferred to electrical energy by the converse piezoelectric effect. To analyze this electro-mechanical system and quantize the behavior of the drive unit, theory of piezoelectric plate developed by Tiersten [33], applied theory of thin plate to piezoelectric effect, is suitable for analyzing the drive unit due to their geometric similarity. We select e-type constitutive equation, Eqn.(2-1- a, b), of piezoelectric materials for the following analysis shown below [58]

$$\begin{cases} S_p = s_{pq}^E T_q - e_{kp} E_k \\ D_k = e_{kp} S_p + \varepsilon_{ki}^S E_i \end{cases} . \tag{2-6}$$

A piezoelectric laminate consists of two layers of piezoelectric laminates placed on top of a structural component, shown in Figure 2-2, is widely used in energy harvesting devices in general [59][56][60]. The piezoelectric ceramic patches attached on the vibrating host structural component deformed with the vibrating structural component and generates electric field due to converse piezoelectric effect.

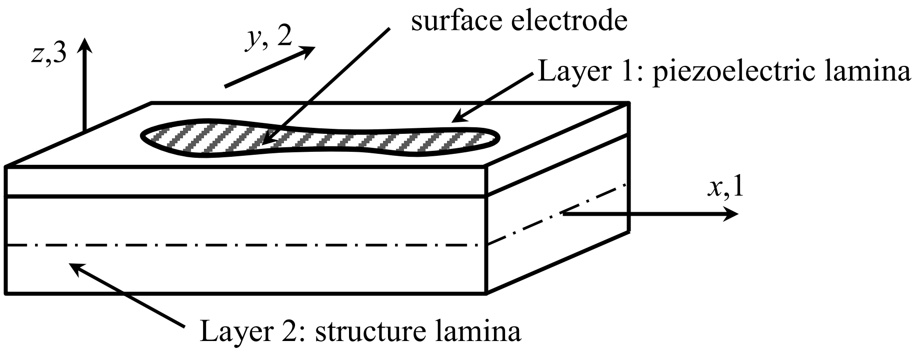

Figure 2-2 Schematic of a three-layer piezoelectric laminates

For most of the applications, piezoelectric laminates are much thinner than its longitudinal and lateral scales, theory of thin plate as well as plane stress assumption hold true for the mechanical analysis; therefore, for the plane stress problem, the normal stress T_3 is assumed to be zero; under the plane stress assumption, the magnitude of T_3 is several orders smaller than the other two stresses, T_1 and T_2. Form the Kirchhoff hypothesis [61], under small deformation condition, plane-remain-plane assumption result to the neglect of thickness shear stress terms, T_4 and T_5. In addition, the electrodes are placed on top and bottom of piezoelectric ceramic, which collects charges induced by electric field in z-direction only; E_1 and E_2 are ignored and E_3 are kept only. Therefore, the reduced two-dimensional constitutive equations of piezoelectric materials are

$$\begin{Bmatrix} T_1 \\ T_2 \\ T_6 \\ D_3 \end{Bmatrix} = \begin{bmatrix} c_{11}^E & c_{12}^E & 0 & e_{31} \\ c_{12}^E & c_{11}^E & 0 & e_{32} \\ 0 & 0 & c_{11}^E & 0 \\ e_{31} & e_{32} & 0 & \varepsilon_{33}^S \end{bmatrix} \begin{Bmatrix} S_1 \\ S_2 \\ S_6 \\ E_3 \end{Bmatrix} \tag{2-7}$$

The sensor equation of piezoelectric materials can be picked from the sensing part of the Eqn. (2-6) as follows.

$$D_3 = e_{31}T_1 + e_{32}T_2 + \varepsilon_{33}^T E \tag{2-8}$$

Substituting the relationship between piezoelectric strain/charge constant d_{kp} and piezoelectric stress/charge constant e_{kp}, the sensor equation Eqn.(2-8) leads to

$$D_3 = d_{31}T_1 + d_{32}T_2 + \varepsilon_{33}^T E \tag{2-9}$$

The sensor equation in Eqn.(2-8) or Eqn.(2-9) describe the mechanical stress/strain induces electric displacement D_3 of the electric dipoles in the piezoelectric materials.

To determine the charges q detected by the surface electrode on the piezoelectric laminate, we perfume electric analysis in theory of electrodynamics to determine the output charges, current, or voltage induced by the deformation of host structure [62].

Coulomb's law for dielectric materials states that the free charges ρ_f at position vector $\boldsymbol{r}$ induced by electric displacement $\boldsymbol{D}$ shows

$$\nabla \cdot \vec{D} = \rho_f(\vec{r}), \tag{2-10}$$

For a volume element $d\tau$ of any dielectric material, the Coulomb's law can be expressed as

$$\nabla \cdot \vec{D} d\tau = \rho_f(\vec{r}) d\tau . \tag{2-11}$$

The total charges q over volume V induced by the electric displacement $\boldsymbol{D}$ can be expressed in the form of volume integral as follows

$$\iiint_V \nabla \cdot \vec{D} d\tau = \iiint_V dq . \tag{2-12}$$

Apply Gauss's law, the divergence of electric displacement field is equal to its flux through a surface *S* which encloses a volume *V* as follows

$$\oiint_{s} \vec{D} \cdot d\vec{A} = q \,, \tag{2-13}$$

Eqn. (2-13) also implies that surface charge element d*q* on a surface electrode element $d\vec{A}$ is induced by the electric displacement $\vec{D}$ of dielectric materials between top and bottom electrodes by the form of

$$dq = \vec{D} \cdot d\vec{A} \,. \tag{2-14}$$

For a laminate structure shown in Figure 2-2, the induced electric charge on a surface element *dA* can be represented as $dq = D_3 dA$, which yields to

$$dq = (e_{31}S_1 + e_{32}S_2 + \varepsilon_{33}^{S} E_3) dA \,. \tag{2-15}$$

For surface element on a piece of piezoelectric laminate with top and bottom electrodes, the induced electric field E_3 ($E_3 = -V/h$; *V*: electric potential between electrodes, *h*: thickness of piezoelectric ceramic) between top and bottom surface elements of electrodes can be represented as

$$dq = (e_{31}S_1 + e_{32}S_2 - \varepsilon_{33}^{S} \frac{V}{h}) dA \tag{2-16}$$

The charges collected by the top and bottom electrodes with areas Σ are the surface integral of every charge element, which yields to

$$q = \oiint_{\Sigma} dq \,, \qquad (\ 2\text{-}17\ )$$

which also shows that the total charges generated by a piece of deformed piezoelectric ceramic is the collection of the charges induced by the piezoelectric materials between a pair of surface elements of top and bottom electrodes.

Applying Gauss' law to fine the charge signals detected by surface electrodes, the charge signals generated by the piezoelectric material is $q = \oiint_{\Sigma} dq$, which results to

$$q = \oiint_{\Sigma} (e_{31}S_1 + e_{32}S_2 - \varepsilon_{33}^{S}\frac{V}{h})dA \,. \qquad (\ 2\text{-}18\ )$$

Equivalent circuit – current source model

Taking time derivative to Eqn.(2-18) the electric current *i* = *dq*/*dt* leads to

$$i(t) = \frac{d}{dt}\oiint_{\Sigma}[e_{31}S_1(x,y;t) + e_{32}S_2(x,y;t)]dxdy - \frac{\varepsilon_{33}^{S}}{h}\frac{d}{dt}\oiint_{\Sigma} V(t)dxdy \,. \qquad (\ 2\text{-}19\ )$$

Since voltage remains spatially constant on the surface electrics, the electric current can be written as

$$i(t) = e_{31}\frac{d}{dt}\iint_{\Sigma}[e_{31}S_1(x,y;t) + e_{32}S_2(x,y;t)]dxdy - \frac{\varepsilon_{33}^{S}A}{h}\frac{dV(t)}{dt} \,, \qquad (\ 2\text{-}20\ )$$

where *A* is the overall surface area of the top or bottom electrode, and *C* ($C = \varepsilon_{33}^{S}A/h$) is the capacitance of the piezoelectric lamina.

The sensor equation shown in Eqn.(2-20) can be graphically represented by an equivalent circuit model shown in Figure 2-3.

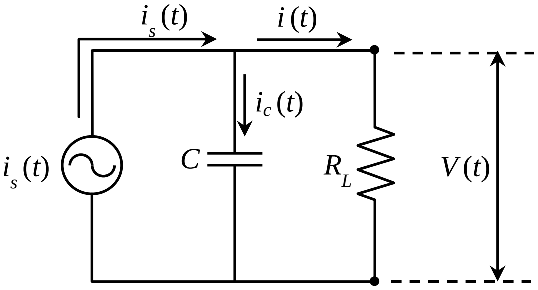

Figure 2-3 Equivalent circuit of the drive unit (current source model)

where $i_s(t) = e_{31}\frac{d}{dt}\iint_{\Sigma}[e_{31}S_1(x,y;t) + e_{32}S_2(x,y;t)]dxdy$ is the current source induced by the piezoelectric lamina, the current $i_C(t) = CdV(t)/dt$ that flows through the internal capacitor of the piezoelectric laminate, the current $i(t)$ sent to the external loading Z_L is the electric impedance of the external loading, and $V(t)$ is the output voltage that applies to the external loading, which is supposed to be sensor unit for SHM.

The governing equation of the sensor unit can be written as the ordinary differential equation as follows

$$\frac{d}{dt}V(t) + \frac{1}{Z_L C}V(t) = \frac{e_{31}}{C}\frac{d}{dt}\oiint_{\Sigma}[e_{31}S_1(x,y;t) + e_{32}S_2(x,y;t)]dxdy\,, \qquad (2\text{-}21)$$

To generalize the equivalent circuit model shown in Figure 2-3, the capacitance C and load resistance R_L are replaced to capacitance impedance $Z_C(\omega)$ and load impedance $Z_L(\omega)$ if they are both frequency-dependent. The generalized equivalent circuit of the drive unit are shown in Figure 2-4.

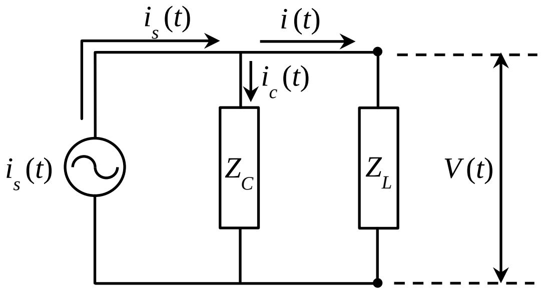

Figure 2-4 Generalized equivalent circuit of the drive unit (current source model)

From Kirchoff's current law, Eqn.(2-19) can be rewritten as

$$i(t) = \frac{d}{dt}\oiint_{\Sigma}[e_{31}S_1(x,y;t) + e_{32}S_2(x,y;t)]dxdy - i_C(t)\,, \qquad (2\text{-}22)$$

where $i_C(t) = V(t)/Z_L$ and $i(t) = V(t)/Z_C$ are current flowing through load Z_L and capacitance Z_C.

The output voltage of the drive unit results to

$$V(t) = \frac{d}{dt}\oiint_{\Sigma}[e_{31}S_1(x,y;t) + e_{32}S_2(x,y;t)]dxdy \times \frac{Z_C Z_L}{Z_C + Z_L}\,, \qquad (2\text{-}23)$$

Equivalent circuit – voltage source model

The equivalent circuit of the drive unit shown in Figure 2-3 can also be represented by voltage source. Consider the sensor equation in Eqn.(2-18) and rearranging it by the capacitance of the piezoelectric lamina C ($C = \varepsilon_{33}^{S}A/h$), the sensor equation then becomes

$$\frac{1}{C}\oiint_{\Sigma}[e_{31}S_1(x,y;t) + e_{32}S_2(x,y;t)]dxy = V + \frac{q}{C}\,, \qquad (2\text{-}24)$$

where Σ is the surface area of the electrodes. Eqn.(2-24) sows that

$v_s(t) = \frac{1}{C}\iint_{\Sigma}[e_{31}S_1(x,y;t) + e_{32}S_2(x,y;t)]dxdy$ is the voltage source induced by the strain on the piezoelectric material, $V_C(t) = q(t)/C$ is the voltage drop across the internal capacitor of the piezoelectric ceramic C, and $V(t)$ is the open-circuit output voltage of the piezoelectric ceramic. Therefore, Eqn.(2-24) can be graphically expressed to an equivalent circuit with a voltage source and an output impedance Z_L as shown in Figure 2-5.

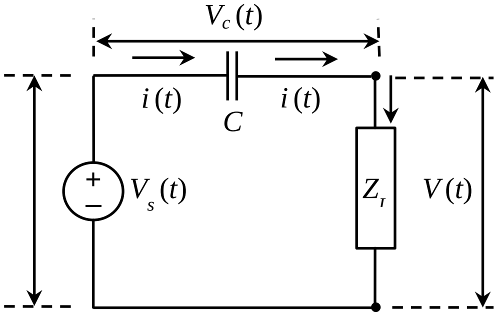

Figure 2-5 Equivalent circuit of the sensor unit

Taking time derivative to Eqn.(2-24), we have the governing equation as follows

$$\frac{1}{C}\frac{d}{dt}\oiint_{\Sigma}[e_{31}S_1(x,y;t)+e_{32}S_2(x,y;t)]dA=\frac{dV}{dt}+\frac{1}{C}\frac{d}{dt}q\,, \tag{2-25}$$

where $i(t) = dq/dt$ is the electric current flowing in the circuit as well as the electrical loading Z_L; therefore, $i(t)$ can be written in terms of voltage drop $V(t)$ across electrical loading Z_L as $i(t) = V(t)/Z_L$. Eqn.(2-25) can be written as

$$\frac{1}{C}\frac{d}{dt}\oiint_{\Sigma}[e_{31}S_1(x,y;t)+e_{32}S_2(x,y;t)]dA=\frac{dV}{dt}+\frac{1}{C}\frac{V(t)}{Z_L}\,, \tag{2-26}$$

Rearrange Eqn.(2-26) and consider $S_1(x, y; t)$ and $S_2(x, y; t)$, we have

$$\frac{d}{dt}V(t)+\frac{1}{Z_LC}V(t)=\frac{1}{C}\frac{d}{dt}\oiint_{\Sigma}[e_{31}S_1(x,y;t)+e_{32}S_2(x,y;t)]dxdy\,, \tag{2-27}$$

which ends up with an identical solution to the differential equation derived from the current source model in Eqn.

To generalize the equivalent circuit model shown in Figure 2-5, the capacitance *C* and load resistance R_L are replaced to capacitance impedance $Z_C(\omega)$ and load impedance $Z_L(\omega)$ if they are both frequency-dependent. The generalized equivalent circuit of the drive unit is shown in Figure 2-6.

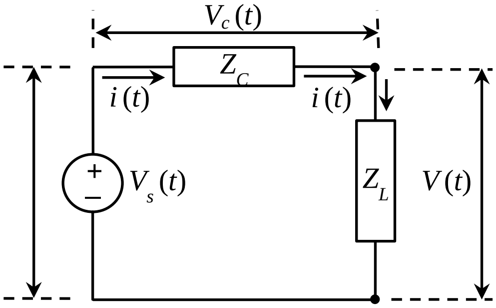

Figure 2-6 Generalized equivalent circuit of the drive unit (voltage source model)

From Kirchoff’s current law, Eqn.(2-22) can be rewritten as

$$\frac{1}{C}\oiint_{\Sigma}[e_{31}S_1(x,y;t)+e_{32}S_2(x,y;t)]dA=V_C+V_L\,, \tag{2-28}$$

where $V_C(t) = i(t)\,Z_L$ and $V_L\,(t) = i(t)\,Z_C$ are voltage drop across load Z_L and capacitance Z_C.

The output current of the drive unit results to

$$i(t)=\frac{1}{C}\oiint_{\Sigma}[e_{31}S_1(x,y;t)+e_{32}S_2(x,y;t)]dxdy\times\frac{1}{(Z_C+Z_L)}\,, \tag{2-29}$$

From Figure 2-6, the output voltage across the load Z_L is determined by

$$V(t)=\frac{1}{C}\oiint_{\Sigma}[e_{31}S_1(x,y;t)+e_{32}S_2(x,y;t)]dxdy\times\frac{Z_L}{(Z_C+Z_L)}\,. \tag{2-30}$$

Considering the imperfection of the piezoelectric ceramic due to fabrication, the piezoelectric ceramic is modeled by a capacitor connected to an internal resistor *R*, meaning that the ceramic is not only a perfect capacitor, but allows a small amount of current going through. The out voltage can then be modified as

$$V(t)=\frac{1}{C}\oiint_{\Sigma}[e_{31}S_1(x,y;t)+e_{32}S_2(x,y;t)]dxdy\times\frac{Z_L}{(Z_C+R_{in}+Z_L)}, \qquad (2\text{-}31)$$

which replace Z_C to Z_C+R_{in}, meaning the internal resistance increases in voltage-source equivalent circuit to divide more voltage from the load. The voltage-source equivalent circuit with loss resistor is shown in Figure 2-7.

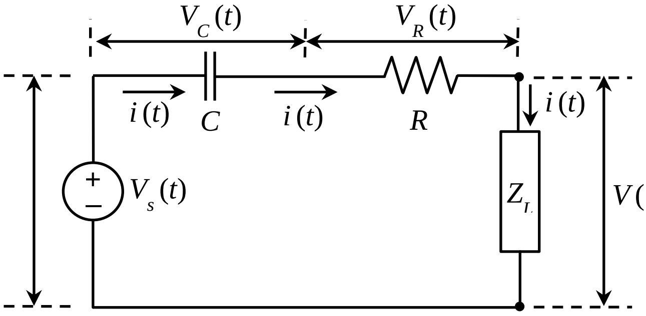

Figure 2-7 Equivalent circuit of the sensor unit with loss resistor

2.3.1 The Sensor Equation of Drive Unit on a Fourth Order Structural System

The flexural vibration of a thin plate can be described by the following governing equation [63]

$$D\nabla^4 w(x,y;t)+\rho h\frac{\partial^2}{\partial t^2}w(x,y;t)=f(x,y;t), \qquad (2\text{-}32)$$

where *D* is the flexural rigidity, *ρ* is the density of the plate, *h* is the thickness of the thin plate, *w* is the displacement in 3-direction, and *f*(*x*, *y*; *t*) is the body force, shows a typical forth order structural system.

To connect the relationships between governing equation shown in (2-32) and sensor equation shown in (2-20), consider a flexural vibration shown in Figure 2-8, let the displacement at the mid-plane equals to the u_0 and v_0 along x and y directions.

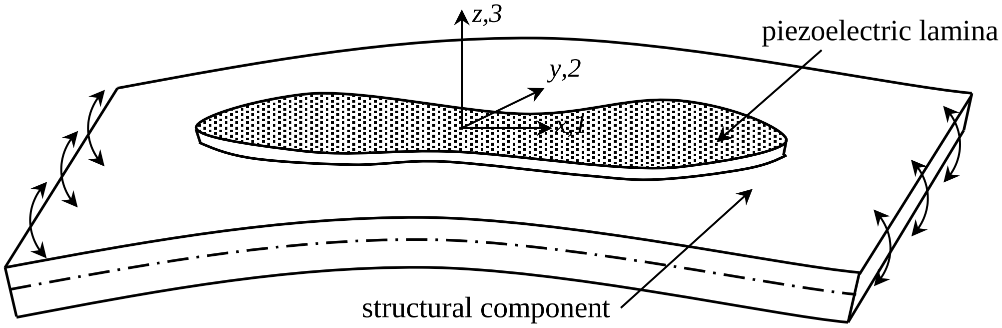

Figure 2-8 Schematic of a piezoelectric pate placed on a flexural structural component

The displacement along the line that perpendicular to the mid-plane equals to

$$u = u_0 - z\frac{\partial w}{\partial x} \text{ and } v = v_0 - z\frac{\partial w}{\partial y}, \qquad (2\text{-}33)$$

where u, v, w are the displacements in 1, 2, and 3-directions, respectively, $\partial w/\partial x$ and $\partial w/\partial y$ are the slope of the thin plate; u_0 and v_0 are displacements on the mid-plane in 1 and 2-directions; z is the distance from the mid-plane to a specific location.

From theory of linear elasticity, the strain distributions are expressed as

$$\begin{Bmatrix} S_1 \\ S_2 \\ S_6 \end{Bmatrix} = \begin{Bmatrix} \partial u / \partial x \\ \partial v / \partial y \\ \partial u / \partial y + \partial v / \partial x \end{Bmatrix}. \qquad (2\text{-}34)$$

Substituting Eqn.(2-33) into Eqn.(2-34) , the strain field within the thin plate can be represented by displacement field as

$$\begin{Bmatrix} S_1 \\ S_2 \\ S_6 \end{Bmatrix} = \begin{Bmatrix} \partial u_0 / \partial x \\ \partial v_0 / \partial y \\ \partial u_0 / \partial y + \partial u_0 / \partial x \end{Bmatrix} - z \begin{Bmatrix} \partial^2 w / \partial x^2 \\ \partial^2 w / \partial y^2 \\ 2\partial^2 w / \partial x \partial y \end{Bmatrix} . \qquad (\text{ 2-35 })$$

The strain field of a thin plate can also be expressed in a general form shown below

$$\begin{Bmatrix} S_1 \\ S_2 \\ S_6 \end{Bmatrix} = \begin{Bmatrix} S_1^0 \\ S_2^0 \\ S_6^0 \end{Bmatrix} - z \begin{Bmatrix} \kappa_1 \\ \kappa_2 \\ \kappa_6 \end{Bmatrix} , \qquad (\text{ 2-36 })$$

where S_1^0 , S_2^0 , and S_6^0 are strain in *x, y* direction and *x-y* plane at mid-plane, respectively; κ_1, κ_2, and κ_6 denote curvature in *x, y* direction and *x-y* plane, respectively; z is the distance from mid-plane to a specific location.

Substituting Eqn.(2-35) to Eqn.(2-8), the sensor equation *q*(*t*) in terms of displacement field of the structure *w*(*x*, *y*, *z*; *t*) can be written as

$$q = \iint_{\Sigma} [e_{31} \frac{\partial u_0}{\partial x} + e_{32} \frac{\partial v_0}{\partial y}] dxdy - z \iint_{\Sigma} [e_{31} \frac{\partial^2 w}{\partial x^2} + e_{32} \frac{\partial^2 w}{\partial y^2}] dxdy - CV(t) . \qquad (\text{ 2-37 })$$

Eqn.(2-37) is based on piezoelectric plate theory, which consider the deformation in both axial (1-) and lateral (2-) directions under the assumption of plane stress to ignore the stress in 3-direction. To simplify the analysis but still practically to the drive unit of proposed SHM system, we apply the simplification from piezoelectric plate theory to Euler-Bernoulli beam model, Eqn. (2-37) can be further expressed as

$$q = -ze_{31} \iint_{\Sigma} \frac{\partial^2 w}{\partial x^2} dxdy - CV(t) . \qquad (\text{ 2-38 })$$

The output electric current then yields to

$$i(t) = -ze_{31}\frac{d}{dt}\iint_{\Sigma}\frac{\partial^2 w}{\partial x^2}dxdy - C\frac{d}{dt}V(t)\,. \tag{2-39}$$

Simplifying the piezoelectric plate to piezoelectric beam, the electric current of the drive unit is

$$i(t) = -ze_{31}b\frac{d}{dt}\int_{x_1}^{x_2}\frac{\partial^2 w}{\partial x^2}dx - C\frac{d}{dt}V(t)\,, \tag{2-40}$$

where *b* is the width of the rectangular piezoelectric patch, x_1 and x_2 are the locations of the starting and ending positions of the piezoelectric ceramic, and $i(t)= V(t)/Z_L$ (Z_L: load impedance),

Applying the modal expansion to the current response of the drive unit, we represent $w(x, t)$ as a convergent series of the eigenfunctions as

$$w = \sum_{n=1}^{\infty}\varphi_n(x)\eta_n(t)\,, \tag{2-41}$$

Applying Eqn.(2-41) to Eqn.(2-40), we have the governing equation of the output voltage as follows

$$\frac{dV(t)}{dt} + \frac{1}{Z_L C}V(t) = \sum_{n=1}^{\infty}\kappa_n\frac{d\eta_n(t)}{dt}\,, \tag{2-42}$$

where κ_n is the modal coupling term in the electric circuit equation:

$$\kappa_n = -e_{31}h_P b\int_{x_1}^{x_2}\frac{d^2\varphi}{dx^2}dx = -e_{31}h_P b\left.\frac{d\varphi}{dx}\right|_{x_1}^{x_2}\,. \tag{2-43}$$

2.3.2 The Sensor Equation of Drive Unit on a Second Order Structural System

The governing equation of a one-dimensional bar in longitudinal vibration is [63]

$$EA\frac{\partial^2 u(x,t)}{\partial x^2} + m\frac{\partial^2 u(x,t)}{\partial t^2} = 0\,, \qquad (2\text{-}44)$$

where u is the displacement in 1-direction, EA is the axial stiffness, m is the mass per unit length, E is the elastic constant, and A is the cross section area.

To connect the relationships between governing equation shown in Eqn.(2-32) and sensor equation shown in Eqn.(2-20), we consider vibration of an one-dimensional bar shown in Figure 2-9. A piezoelectric lamina with top and bottom electrodes is attached on the top surface of a thin plate as the structural component, undergone displacement in 1-direction only. Assume that the thickness and rigidity of piezoelectric lamina are much smaller than those of structural component so that the piezoelectric lamina provides no constraint to the host structural component.

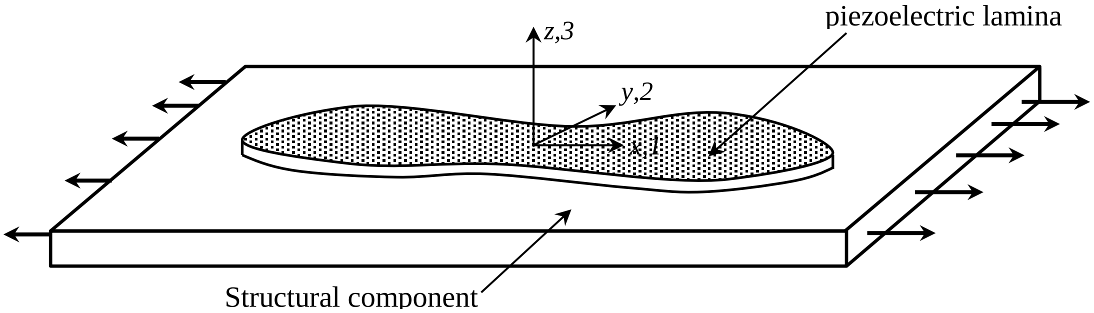

Figure 2-9 Schematic of a piezoelectric pate placed on an one-dimensional bar

From theory of linear elasticity, the strain distributions of one-dimensional in-plane deformation are expressed as

$$S_1 = \frac{\partial u}{\partial x}\,. \qquad (2\text{-}45)$$

Substituting Eqn.(2-34) to Eqn.(2-18), the sensor equation $q(t)$ in terms of displacement field of the structure $u(x, y, z; t)$ can be written as

$$q(t) = e_{31}\iint_{\Sigma} \frac{\partial u}{\partial x} dxdy - CV(t) . \qquad (2\text{-}46)$$

The output electric current then yields to

$$i(t) = e_{31}\frac{d}{dt}\iint_{\Sigma} \frac{\partial u}{\partial x} dxdy - C\frac{d}{dt}V(t) . \qquad (2\text{-}47)$$

Applying the modal expansion to the current response of the drive unit, we represent *w*(*x, t*) as a convergent series of the eigenfunctions as

$$w = \sum_{n=1}^{\infty} \varphi_n(x)\eta_n(t) , \qquad (2\text{-}48)$$

Applying Eqn.(2-48) to Eqn.(2-68), we obtain the governing equation of the output voltage as follows

$$\frac{dV(t)}{dt} + \frac{1}{Z_L C}V(t) = \sum_{n=1}^{\infty} \kappa_n \frac{d\eta_n(t)}{dt} , \qquad (2\text{-}49)$$

where κ_n is the modal coupling term, that we couple the mechanical response to the electric circuit equation

$$\kappa_n = -e_{31}h_P b\int_{x_1}^{x_2} \frac{d\varphi(x)}{dx} dx = -e_{31}h_P b\varphi(x)\Big|_{x_1}^{x_2} . \qquad (2\text{-}50)$$

2.4 Coupled Mechanical Equation of Drive Unit

The partial differential equation that governs the forces vibrations of a beam is

$$m\frac{\partial^2 w}{\partial t^2} + \frac{\partial^2}{\partial x^2}\big(M(x,t)\big) = f(x,t) , \qquad (2\text{-}51)$$

where *m* is the mass per unit length, *M*(*x*, *t*), and *f*(*x*, *t*) are the internal bending moment and external force at position *x* and time *t*, respectively.

For the case of dynamic four-point bending case, the forcing term in Eqn.(2-51) can be expressed as

$$f(x,t) = F(t)\left(\delta(x+\frac{L_2}{2}) + \frac{d}{x}\delta(x-\frac{L_2}{2})\right), \qquad (\text{ 2-52 })$$

where δ(*x*) is the Dirac delta function and *F*(*t*) is the force that applied at the internal legs of the four-point-bending fixture positioned at $x = -L_2/2$ and $x = L_2/2$.

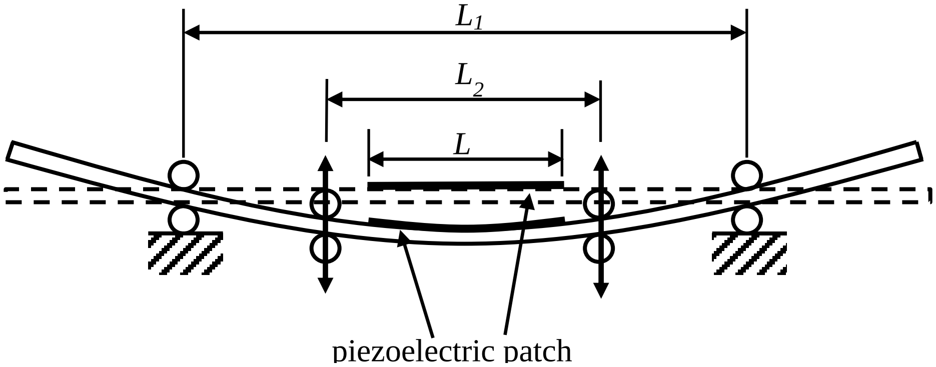

Figure 2-10 Beam in four-point-bending fixture

The internal bending moment in Eqn.(2-51) is the first moment of axial stress over the cross-section:

$$M(x,t) = -b\left(\int_0^{h_S} zT_1^S dz + \int_{h_S}^{h_S+h_P} zT_1^P \left(H(x+\frac{L}{2} - H(x-\frac{L}{2})\right)dz\right), \qquad (\text{ 2-53 })$$

where *H*(*x*) is the unit step function that specifies the size and location of the piezoelectric ceramic (length *L*, placed starting from $x = -L_2/2$ and ending at $x = L_2/2$).

The axial stress components in the piezoelectric ceramic and substrate layers, respectively, are given by the following constitutive relations:

$$T_1^S = Y^S S_1^S \text{ , } T_1^P = c_{11}^E S_1^P - e_{31} E_3 \text{ ,.} \qquad (\text{ 2-54 })$$

In Euler-Bernoulli beam theory, the axial strain at a certain level z from the neutral axis of the component beam is proportional to the curvature of the beam $\kappa = -\partial^2 w/\partial x^2$ at a specific position x and time t:

$$S_1(x,z,t) = -z \frac{\partial^2 w(x,t)}{\partial x^2} \text{ .} \qquad (\text{ 2-55 })$$

Substituting Eqn.(2-52) ~ Eqn.(2-55) to Eqn.(2-51) and applying the relation between electric field $E(t)$ and electric field $V(t)$, $E = -V(t)/h_p$, the coupled beam equation can be obtained as follows

$$m \frac{\partial^2 w}{\partial t^2} + \frac{\partial^2}{\partial x^2}\left(YI \frac{\partial^2 w}{\partial x^2} \right) + \vartheta V(t) \left(\frac{d}{x} \delta(x + \frac{L}{2}) - \frac{d}{x} \delta(x - \frac{L}{2}) \right) = f(x,t) \text{ .} \qquad (\text{ 2-56 })$$

where ϑ couples the electric characteristics of piezoelectric materials to mechanical vibration by piezoelectric constant e_{31} is

$$\vartheta = -\frac{1}{2} e_{31} b (2h_S - 2h_0 + h_P) \text{ .} \qquad (\text{ 2-57 })$$

The equivalent bending stiffness of the beam YI and mass per unit m in Eqn.(2-56) are

$$YI = \frac{1}{3} \left\{ c_{11} \left[(h_0 - h_S)^3 + (h_S + h_P - h_0)^3 \right] + Y_{11} \left[h_0^{\,3} + (h_0 - h_S)^3 \right] \right\} \qquad (\text{ 2-58 })$$

$$m = b\rho_S h_S + b\rho_P h_P \,, \tag{2-59}$$

where c_{11} and Y_{11} are the stiffness of the piezoelectric ceramic and substrate in 11-direction (x-direction), respectively; ρ_p and ρ_s are the density of the piezoelectric ceramic and, respectively.

Mode shapes

The vibration response of the drive unit can be represented as a convergent series of the eigenfunctions as

$$w = \sum_{n=1}^{\infty} \varphi_n(x)\eta_n(t) \,, \tag{2-60}$$

where $\varphi_n(x)$ is the mode shapes of the beam and $\eta_n(x)$ is the modal coordinates of the beam structure.

Applying Eqn.(2-60) to Eqn.(2-56), the modal expansion of the beam is

$$m\varphi_n \frac{\partial^2 \eta_n}{\partial t^2} + \eta_n \frac{\partial^2}{\partial x^2}\left(YI \frac{\partial^2 \varphi_n}{\partial x^2} \right) + \vartheta V(t) \left(\frac{d}{x}\delta(x+\frac{L}{2}) - \frac{d}{x}\delta(x-\frac{L}{2}) \right) = F(t)P(x) \,. \tag{2-61}$$

To obtain the mode shapes, we ground the electrical output ($V(t)$=0) and consider the no forcing terms ($f(x, t)$=0), the partial differential equation is reduced to

$$m\varphi_n \frac{\partial^2 \eta_n}{\partial t^2} + \eta_n \frac{\partial^2}{\partial x^2}\left(YI \frac{\partial^2 \varphi_n}{\partial x^2} \right) = 0 \,. \tag{2-62}$$

For the beam structure we use for experiments, the length outside the external legs (2.5 cm) is relative smaller than the beam length (10.0 cm) in low frequency (<< 212 Hz, the first resonant freqency) in particular, we ignore the bending moment induced by the part of the beam that outside the external legs. Applying boundary conditions: zero displacements and zero bending moments at the locations external legs of the four-point-bending fixture, we obtain

$$w(x,t)\Big|_{x=\pm\frac{L_1}{2}}=0 \text{ and } \frac{d^2w(x,t)}{dx^2}\Bigg|_{x=\pm\frac{L_1}{2}}=0. \qquad (2\text{-}63)$$

The mode shapes of the beam can be expressed as the eigenfunctions of the partial differential equations as [63]

$$\varphi_n(x)=\sqrt{\frac{2}{mL_1}}\sin\left(\frac{n\pi}{L_1}x+\frac{n\pi}{2}\right),\ n = 1, 2, 3, \ldots \qquad (2\text{-}64)$$

The eigenvalues are the natural frequencies of the beam structure

$$\omega_n(x)=(n\pi)^2\sqrt{\frac{YI}{mL_1^{\,4}}},\ n = 1, 2, 3, \ldots \qquad (2\text{-}65)$$

The orthogonality relations of the beam are follows

$$\int_{-\frac{L_1}{2}}^{\frac{L_1}{2}}\varphi_m(x)m\varphi_n(x)dx=\delta_{mn},\ m, n = 1, 2, 3, \ldots \qquad (2\text{-}66)$$

$$\int_{-\frac{L_1}{2}}^{\frac{L_1}{2}}\varphi_m(x)YI\,\frac{\partial^4\varphi_n(x)}{\partial x^4}dx=\omega_n^{\ 2}\delta_{mn},\ m, n = 1, 2, 3, \ldots \qquad (2\text{-}67)$$

Modal coordinates

Considering a four-bending case, the external force is applied at the internal legs of the fixture at position $x = \pm L_2/2$, the modal expansions of Eqn.(2-56) is

$$m\frac{\partial^2 w}{\partial t^2}+\frac{\partial^2}{\partial x^2}\left(YI\,\frac{\partial^2 w}{\partial x^2}\right)+\vartheta V(t)\left(\frac{d}{x}\delta(x+\frac{L}{2})-\frac{d}{x}\delta(x-\frac{L}{2})\right)=f(t)\left(\delta(x+\frac{L_2}{2})+\frac{d}{x}\delta(x-\frac{L_2}{2})\right). \qquad (\text{ 2-68 })$$

Applying the orthonormality relations to Eqn.(2-68), we have

$$\begin{aligned}\frac{\partial^2\eta_n}{\partial t^2}\int_{-\frac{L_1}{2}}^{\frac{L_1}{2}}\varphi_m m\varphi_n dx+\eta_n\int_{-\frac{L_1}{2}}^{\frac{L_1}{2}}\varphi_m YI\,\frac{\partial^4\varphi_n}{\partial x^4}dx+\vartheta V(t)\int_{-\frac{L_1}{2}}^{\frac{L_1}{2}}\varphi_m(x)\left(\frac{d}{x}\delta(x+\frac{L}{2})-\frac{d}{x}\delta(x-\frac{L}{2})\right)dx\\=f(t)\int_{-\frac{L_1}{2}}^{\frac{L_1}{2}}\varphi_m(x)\left(\delta(x+\frac{L_2}{2})+\frac{d}{x}\delta(x-\frac{L_2}{2})\right)dx\end{aligned} \qquad (\text{ 2-69 })$$

From Eqn.(2-69), the coupled beam equation in modal coordinates is

$$\frac{\partial^2\eta_n}{\partial t^2}+\omega_n{}^2\eta_n+\chi_n V(t)=f_n(t)\,, \qquad (\text{ 2-70 })$$

where the modal electromechanical coupling term χ_n is

$$\chi_n=\vartheta\left(\left.\frac{d\varphi_n(x)}{x}\right|_{-\frac{L}{2}}-\left.\frac{d\varphi_n(x)}{x}\right|_{\frac{L}{2}}\right), \qquad (\text{ 2-71 })$$

and the modal mechanical forcing term is the modal mechanical forcing function can be expresses as

$$f_n(t)=\frac{f(t)}{m}\left(\varphi_n(-\frac{L_2}{2})+\varphi_n(\frac{L_2}{2})\right). \qquad (\text{ 2-72 })$$

Applying the mode shapes of the beam in Eqn.(2-64) to Eqn.(2-71), we have the modal electromechanical coupling term as

$$\chi_n=\frac{n\pi}{L_1}\sqrt{\frac{2}{mL_1}}\vartheta\left(\cos(\frac{n\pi}{2}\frac{L}{L_1}-\frac{n\pi}{2})-\cos(\frac{n\pi}{2}\frac{L}{L_1}+\frac{n\pi}{2})\right). \qquad (\text{ 2-73 })$$

and the modal mechanical forcing term as

$$f_n(t) = \frac{f(t)}{m}\left(\sin(-\frac{n\pi}{2}\frac{L_2}{L_1} + \frac{n\pi}{2}) + \sin(\frac{n\pi}{2}\frac{L_2}{L_1} + \frac{n\pi}{2}) \right). \qquad (2\text{-}74)$$

2.5 Voltage Output of the Drive Unit for Four-point-bending Structure

Considering a fourth order structural system (beam structure), the coupled electric circuit equation (Eqn.(2-42)) and coupled mechanical equation (Eqn.(2-70)) are list below

$$\frac{dV(t)}{dt} - \frac{1}{Z_L C}V(t) = \sum_{n=1}^{\infty} \kappa_n \frac{d\eta_n(t)}{dt}.$$

$$\frac{\partial^2 \eta_n}{\partial t^2} + \omega_n{}^2 \eta_n + \chi_n V(t) = f_n(t) \qquad (2\text{-}75\text{ a, b})$$

Assuming the external force *f* (*t*) applied by four-point-bending fixture is harmonic in time, the induced output voltage *V*(*t*) and modal coordinates *η*(*t*) are induced harmonic in time as well (i.e. $f_n(t) = F_0 e^{j\omega t}$, $\eta_n(t) = H_n e^{j\omega t}$, $V(t) = V_o e^{j\omega t}$, where *ω* is the driving angular frequency, *j* is the unit imaginary number).

The harmonic the coupled electric circuit equation and coupled mechanical equation can be obtained

$$(1 + j\omega Z_L C)V_o - j\omega \sum_{n=1}^{\infty} \kappa_n H_n = 0$$

$$(\omega_n{}^2 - \omega^2)H_n + \chi_n V_n = F_n. \qquad (2\text{-}76\text{ a, b})$$

where modal mechanical forcing term F_n is,

$$F_n = \frac{F_0}{m}\left(\varphi_n(-\frac{L_2}{2}) + \varphi_n(\frac{L_2}{2}) \right) \qquad (2\text{-}77)$$

and electromechanical coupling terms χ_n and κ_n are

$$\chi_n = -\frac{2n\pi}{L_1}\sqrt{\frac{2}{mL_1}}\vartheta\cos\left(\frac{n\pi}{2}\frac{L}{L_1}+\frac{n\pi}{2}\right) \tag{2-78}$$

$$\kappa_n = -e_{31}h_P b\int_{x_1}^{x_2}\frac{d^2\varphi}{dx^2}dx = -e_{31}h_P b\left.\frac{d\varphi}{dx}\right|_{x_1}^{x_2}. \tag{2-79}$$

The modal coordinates $\eta_i(\omega)$ can be obtained

$$H_n(\omega) = \left(F_n - \chi_n \frac{\sum_{n=1}^{\infty}\frac{j\omega\kappa_n F_n}{\omega_n^{\ 2}-\omega^2}}{1+j\omega Z_L C+\sum_{n=1}^{\infty}\frac{j\omega Z_L\kappa_n\chi_n}{\omega_n^{\ 2}-\omega^2}} \right)\left(\frac{1}{\omega_n^{\ 2}-\omega^2}\right). \tag{2-80}$$

The frequency response of the displacement is

$$w(x,\omega) = \sum_{n=1}^{\infty}\left(\left(F_n - \chi_n \frac{\sum_{n=1}^{\infty}\frac{j\omega\kappa_n F_n}{\omega_n^{\ 2}-\omega^2}}{1+j\omega Z_L C+\sum_{n=1}^{\infty}\frac{j\omega Z_L\kappa_n\chi_n}{\omega_n^{\ 2}-\omega^2}} \right)\left(\frac{1}{\omega_n^{\ 2}-\omega^2}\right)\varphi_n(x)\right). \tag{2-81}$$

The frequency response function of the output voltage is

$$V_o(\omega) = \frac{\sum_{n=1}^{\infty}\frac{j\omega\kappa_n F_n Z_L}{\omega_n^{\ 2}-\omega^2}}{1+j\omega Z_L C+\sum_{n=1}^{\infty}\frac{j\omega Z_L\kappa_n\chi_n}{\omega_n^{\ 2}-\omega^2}}. \tag{2-82}$$

Applying the mode shapes $\varphi_n(x)$ in Eqn.(2-64) to electromechanical coupling terms χ_n and κ_n in Eqn.(2-71) and Eqn.(2-79) as well as the modal mechanical forcing term F_n Eqn.(2-77), we obtain the frequency response function of the beam under the harmonic excitations of four-point-bending fixture.

The steady state response of the mid-span displacement *w*(*t*) and output voltage *V*(*t*) at angular frequency can then be determined as

$$w(x=0,\omega)=\sum_{n=1}^{\infty}\left(\left(F_n-\chi_n\frac{\displaystyle\sum_{n=1}^{\infty}\frac{j\omega\kappa_n F_n}{{\omega_n}^2-\omega^2}}{1+j\omega Z_L C+\displaystyle\sum_{n=1}^{\infty}\frac{j\omega Z_L\kappa_n\chi_n}{{\omega_n}^2-\omega^2}}\right)\left(\frac{1}{{\omega_n}^2-\omega^2}\right)\varphi_n(x=0,t)\right)e^{j\omega t} \qquad (\text{2-83})$$

$$V_o(t)=\frac{\displaystyle\sum_{n=1}^{\infty}\frac{j\omega\kappa_n F_n Z_L}{{\omega_n}^2-\omega^2}}{1+j\omega Z_L C+\displaystyle\sum_{n=1}^{\infty}\frac{j\omega Z_L\kappa_n\chi_n}{{\omega_n}^2-\omega^2}}e^{j\omega t}\,. \qquad (\text{2-84})$$

Output voltage at low frequency

Consider a practical case, the piezoelectric sensors are usually in rectangular shape with length *l*, width *b* (area *A*=*bl*), mounted on a structural component, which is very large in size compared to the piezoelectric sensors. The spatial distribution of stress and strain do not vary a lot locally on the piezoelectric lamina, so that the in-plane stress and strain distribution on the piezoelectric lamina can be approximated as uniformly distributed, where $S_1(x, y; t) = S_1(t)$ remains constant in spatial domain. Therefore Eqn.(2-19) can be simplified with constant stress distribution in spatial domain as follows

$$\frac{V(t)}{Z_L}=e_{31}A\frac{dS_1(t)}{dt}-C\frac{dV(t)}{dt}\,. \qquad (\text{2-85})$$

Consider a harmonic output voltage $V(t)=V_0e^{j\omega t}$ and harmonic strain $S_1(t)=S_{1,0}e^{j\omega t}$ induced by a harmonic excitation, where V_0 and $S_{1,0}$ are the complex number, ω is the angular frequency of the excitation. Eqn.(2-85) can be written as

$$\frac{1}{Z_L}V_0e^{j\omega t}=e_{31}A\frac{d}{dt}S_{1,0}e^{j\omega t}-C\frac{d}{dt}V_0e^{j\omega t}\,. \tag{2-86}$$

Take time derivative of the complex form of the governing equation, we obtain

$$\frac{1}{Z_L}V_0e^{j\omega t}=e_{31}Aj\omega S_{1,0}e^{j\omega t}-j\omega CV_0e^{j\omega t}\,. \tag{2-87}$$

Further simplified Eqn.(2-87) we have

$$(j\omega+\frac{1}{Z_LC})V_0e^{j\omega t}=j\omega\frac{e_{31}}{C}e^{j\omega t}AS_{1,0}\,. \tag{2-88}$$

The output voltage amplitude then yields to

$$V_0=\frac{j\omega Z_Le_{31}A}{1+j\omega Z_LC}S_{1,0}\,. \tag{2-89}$$

The voltage response results to

$$V(t)=e^{j(\omega t+\varphi)}\frac{\omega Z_Le_{31}A}{\sqrt{1+\omega^2{Z_L}^2C^2}}S_{1,0}\,, \tag{2-90}$$

where phase angle φ is

$$\varphi=\tan^{-1}\frac{1}{\omega Z_LC}\,, \tag{2-91}$$

In experiment, the output from piezoelectric layers on an aluminum beam in a four-point-bending fixture was conducted by a fixture shown in Figure 2-11 to evaluate the performance of the proposed SHM system. The induced bending moment and the spatial distributions between the inner span are constant, which fits the case of most applications. To conduct four-point-bending experiment, the material properties and dimensions of piezoelectric ceramic and aluminum beam are shown in Table 2-2.

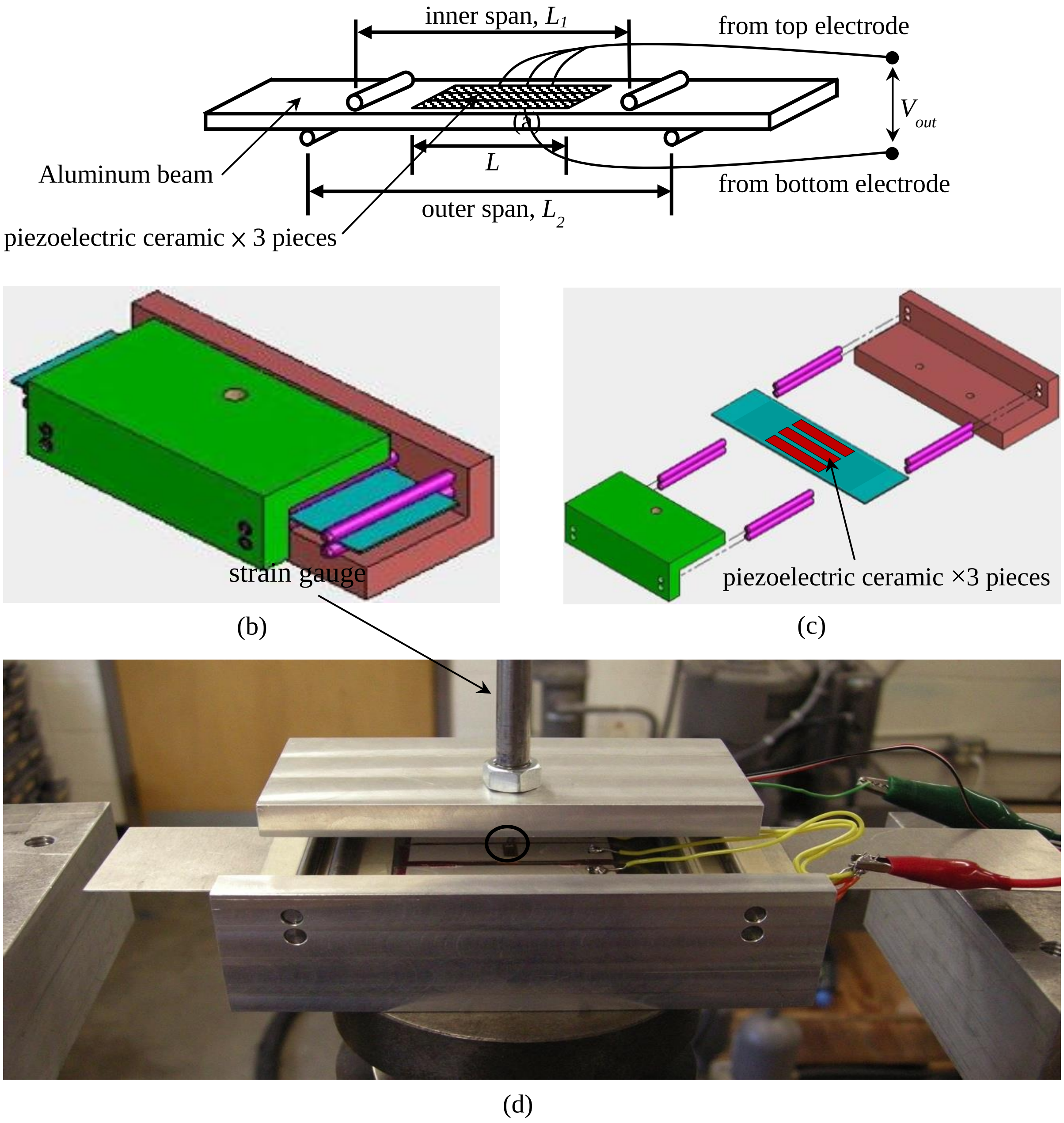

Figure 2-11 Four-point-bending fixture (a) schematic of four-point-bending beam structure and piezoelectric lamina, (b) four-point-bending fixture, (c) exploded view of a four-point-bending fixture, and (d) photo of four-point-bending setup.

Table 2-2 Materials properties and dimensions of piezoelectric patches, aluminum beam and four-point-bending fixture

Piezoelectric ceramic (PZT C-6 from Fuji ceramics, 3 pieces)	
L = 5.0cm (length)	C = 20.4 nF (internal capacitance)
b = 1.0cm (width)	R_0 = 18.5 MPa (internal resistance)
t = 0.5mm (thickness)	ρ = 7650 kg/m^3 (density)
Aluminum beam	
L = 15.0cm (length)	E_{11} = 69 GPa (Young's modulus)
b = 4.0cm (width)	ν = 0.3 (Poisson ratio)
t = 0.5mm (thickness)	ρ = 2700 kg/m^3 (density)
Four-point-bending fixture	
L_1 = 7.5 cm (inner span)	L_2 = 10 cm (outer span)

Table 2-3 stiffness [***c***] and compliance [***s***] matrix of PZT C-6

$$[c]=\begin{bmatrix} c_{11} & c_{21} & c_{31} & c_{41} & c_{51} & c_{61} \\ c_{12} & c_{22} & c_{32} & c_{42} & c_{52} & c_{62} \\ c_{13} & c_{32} & c_{33} & c_{43} & c_{53} & c_{63} \\ c_{14} & c_{42} & c_{34} & c_{44} & c_{54} & c_{64} \\ c_{15} & c_{52} & c_{35} & c_{45} & c_{55} & c_{65} \\ c_{16} & c_{62} & c_{36} & c_{46} & c_{56} & c_{66} \end{bmatrix}=\begin{bmatrix} 62 & -17.4 & -13.9 & 0 & 0 & 0 \\ -17.4 & 62 & -13.9 & 0 & 0 & 0 \\ -13.9 & -13.9 & 49 & 0 & 0 & 0 \\ 0 & 0 & 0 & 19 & 0 & 0 \\ 0 & 0 & 0 & 0 & 19 & 0 \\ 0 & 0 & 0 & 0 & 0 & 22.5 \end{bmatrix}\times 10^{9}\ \text{Pa}$$

$$[s]=\begin{bmatrix} s_{11} & s_{21} & s_{31} & s_{41} & s_{51} & s_{61} \\ s_{12} & s_{22} & s_{32} & s_{42} & s_{52} & s_{62} \\ s_{13} & s_{32} & s_{33} & s_{43} & s_{53} & s_{63} \\ s_{14} & s_{42} & s_{34} & s_{44} & s_{54} & s_{64} \\ s_{15} & s_{52} & s_{35} & s_{45} & s_{55} & s_{65} \\ s_{16} & s_{62} & s_{36} & s_{46} & s_{56} & s_{66} \end{bmatrix}=\begin{bmatrix} 16.1 & -5.74 & -7.22 & 0 & 0 & 0 \\ -5.74 & 16.1 & -7.22 & 0 & 0 & 0 \\ -7.22 & -7.22 & 20.4 & 0 & 0 & 0 \\ 0 & 0 & 0 & 52.6 & 0 & 0 \\ 0 & 0 & 0 & 0 & 52.6 & 0 \\ 0 & 0 & 0 & 0 & 0 & 44.3 \end{bmatrix}\times 10^{-12}\ \text{Pa}^{-1}$$

Table 2-4 Piezoelectric strain/charge [***d***], stress/charge [***e***] and permittivity [*ε*] matrix of PZT C-6

$$[d]=\begin{bmatrix} d_{11} & d_{12} & d_{13} & d_{14} & d_{15} & d_{16} \\ d_{21} & d_{22} & d_{23} & d_{24} & d_{25} & d_{26} \\ d_{31} & d_{32} & d_{33} & d_{34} & d_{35} & d_{36} \end{bmatrix}=\begin{bmatrix} 0 & 0 & 0 & 758 & 758 & 0 \\ 0 & 0 & 0 & 758 & -758 & 0 \\ -210 & -210 & 472 & 0 & 0 & 0 \end{bmatrix}\times 10^{-12} \text{ C/m}$$

$$[e]=\begin{bmatrix} e_{11} & e_{12} & e_{13} & e_{14} & e_{15} & e_{16} \\ e_{21} & e_{22} & e_{23} & e_{24} & e_{25} & e_{26} \\ e_{31} & e_{32} & e_{33} & e_{34} & e_{35} & e_{36} \end{bmatrix}=\begin{bmatrix} 0 & 0 & 0 & 14.4 & 14.4 & 0 \\ 0 & 0 & 0 & 14.4 & -14.4 & 14.4 \\ -13.02 & -13.02 & 10.02 & 0 & 0 & 0 \end{bmatrix} \text{C-N/m}^3$$

$$[\varepsilon]=\begin{bmatrix} \varepsilon_{11} & \varepsilon_{12} & \varepsilon_{13} \\ \varepsilon_{21} & \varepsilon_{22} & \varepsilon_{23} \\ \varepsilon_{31} & \varepsilon_{32} & \varepsilon_{33} \end{bmatrix}=\begin{bmatrix} 2270 & 0 & 0 \\ 0 & 2270 & 0 \\ 0 & 0 & 2130 \end{bmatrix}\times 8.854\times 10^{-12} \text{ Farad/m}$$

Three pieces of 10 mm×50 mm×0.5 mm PZT C-6 ceramic from Fuji Ceramics (Japan) are utilized to our drive unit. The critical material properties for evaluating its electric output are dielectric constant $\varepsilon_{33}=1170\times 8.854\times 10^{-12}$ F/m and piezoelectric charge constant $d_{31}= -141\times 10^{-12}$ C/N; therefore, the internal resistance *R* of once piece of PZT C-6 ceramic can be measured as 3.21MΩ and internal capacitance *C* can be calculated as 10.4nF. The output voltage reached to 8.47 V if a 1.0 Hz cyclic loading, which induces a 12.5 MPa cyclic stress on the topmost layer of drive unit, is applied on the structural component. Figure 2-12 shows that the theoretical predictions agree well to the experimental result while a 1.0 Hz cyclic loading, which induces a 12.5 MPa on the topmost surface of the drive, generates 8.0 V from the drive unit. By the linear relationship of the output voltage from drive unit, a stress of 1.8 MPa amplitude induced by cyclic loading excites the drive unit generating 5 V to sensor unit. The experiment results are 5% smaller than theoretical predictions, which could be that the piezoelectric provides a certain of constraint to the host structure since the rigidity and thickness of the aluminum beam is not much larger than the piezoelectric ceramic, which does not perfectly follow the assumption we set in the theoretical model.

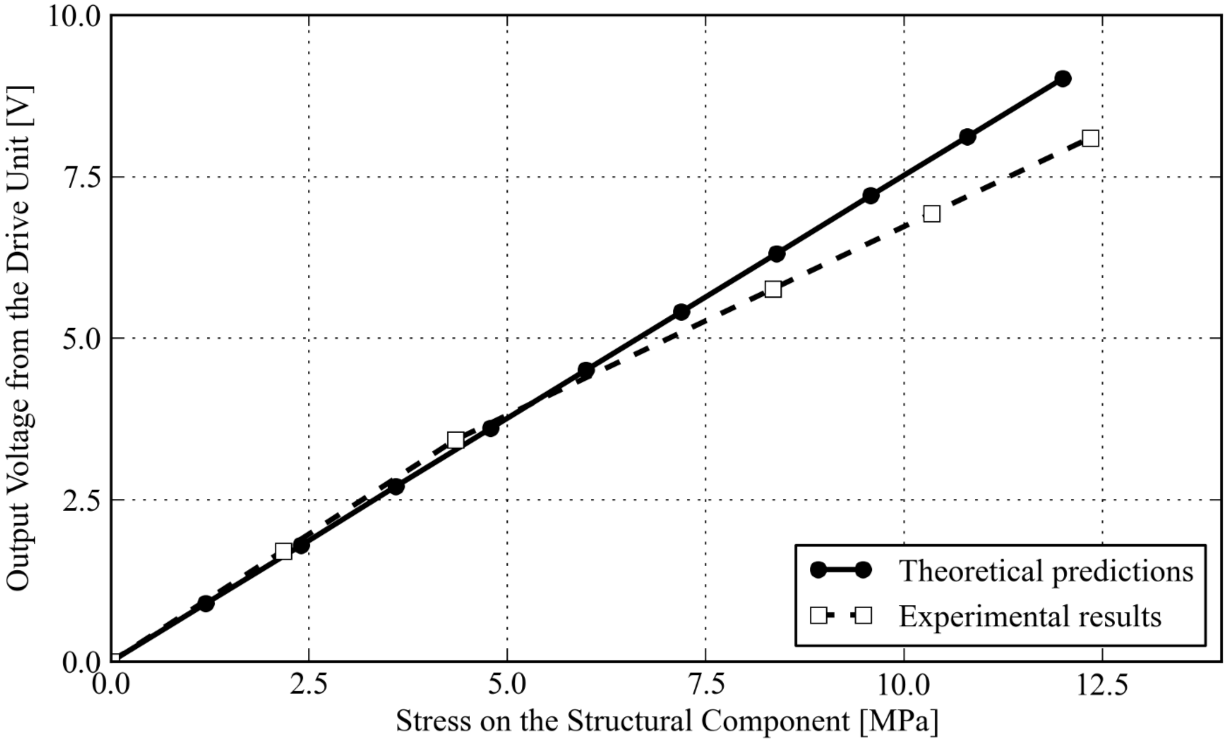

Figure 2-12 Theoretical predictions and experimental results of stress on the structural component vs output voltage from drive (mother) piezoelectric unit

2.6 Finite Element Analysis of the Mechanical and Electric Response of Drive Unit

To verify the expressions of the voltage response in Eqn.(2-90) and Eqn.(2-91), ANSYS finite element simulations are used to analyze the voltage of harmonic and transient response of the drive unit.

We model the drive unit, which has been conducted in the experiment shown in Figure 2-11: three pieces of piezoelectric patch attached on an aluminum beam with dimensions and material properties of them shown in Table 2-2.

To perform finite element simulation by ANSYS, the beam structure is modeled using element type `SOLID186`, a higher order 3-D 20-node structural solid element that exhibits quadratic displacement behavior. The displacement of the nodes is considered for the settings of the `SOLID186` element properties. The degrees of freedom are translations in *x*, *y* and *z*-directions at each node, denoted by `UX`, `UY`, and `UZ`. Materials properties required for this element on the structural component of the model is Young's modulus, Poisson's ratio, and density, which are `69E9`, `0.3`, and `2700`, respectively. All the units used were SI system in default.

The piezoelectric material was modeled using a 3D coupled field solid element `SOLID226` to simulate the interaction between mechanical and electrical behaviors of the drive unit. With appropriate element settings, the `SOLID226` is defined by 20 nodes having four degrees of freedom per node: translations in the nodal *x*, *y*, *z* directions, and voltage, denoted as `UX`, `UY`, `UZ` and `VOLT`, respectively. Required material properties to sufficiently describe the behaviors of piezoelectric ceramics are: Young's modulus, Poisson ratio, permittivity, density, permittivity, elastic compliance and piezoelectric charge constants with the number of `62E9`, `0.3`, `2130*8.854E-12`, respectively. In addition, the three pieces of piezoelectric ceramics bonded on the top of the aluminum are assigned to tables of the required material constants for PZT. Since piezoelectric ceramics are anisotropic materials, meaning that stress, strain, electric field, etc. behave differently in *x*, *y* and *z* directions. The matrices of required material properties must be transformed properly to make sure that the polarization direction of PZTs is oriented along +*z* direction of global coordinate. The element coordinate must be aligned to the *z* coordinate for the polarization direction as well.

The only electrical DOF for `SOLID226` is voltage, which implies that the `SOLID226` in ANSYS consider piezoelectric output is a voltage source. The electric potential generated on the top electrode of the piezoelectric drive unit while the structural component deformed is an open-looped output voltage, the output with infinite impedance of electrical loadings. However, while the piezoelectric drive unit is in used, connected to the next electric stage, for example, a measuring devices, the internal resistance and capacitor shows up and affects the output of the drive unit. To simulate the output voltage with electrical loadings, considering the voltage-source nature of the ANSYS element type `SOLID226`, the voltage source model in Figure 2-5 is adopted to modify the output voltage of the drive unit. The nodal solution of electric potential on the top electrode is considered to be the voltage source in Figure 2-5, additional circuit elements internal capacitance, internal resistance, and external electrical loading connected from the top electrode of the drive unit in series, to the electrical ground, in voltage source model, are modeled by ANSYS electric component element `CIRCU94`.

Figure 2-13 (a) and (b) show the FEM and physical models of the drive unit, respectively. The side view of the FEM model shown in Figure 2-13 (a) indicates that the mesh pattern has 32337 nodes, 16704 20-noded elements and another three circuit elements: one capacitor and two resistor elements to model internal capacitance, internal resistance and electrical loading. Figure 2-13 (b) shows that three pieces of piezoelectric ceramics are bonded on the top of the aluminum beam. The poling direction is set to point downward in $-y$ direction to the Cartesian coordinate. To specify the top and bottom electrodes of the piezoelectric ceramics, the voltage degree of freedom for every node on the same piece of electrode is coupled to a specific node on that electrode so that every node on the conductor is equipotential. This 3D finite model is parameterized and programmed by APDL (ANSYS Parametric Design Language), a FORTRAN-like programming language. Detailed script is list in Appendix I**.**

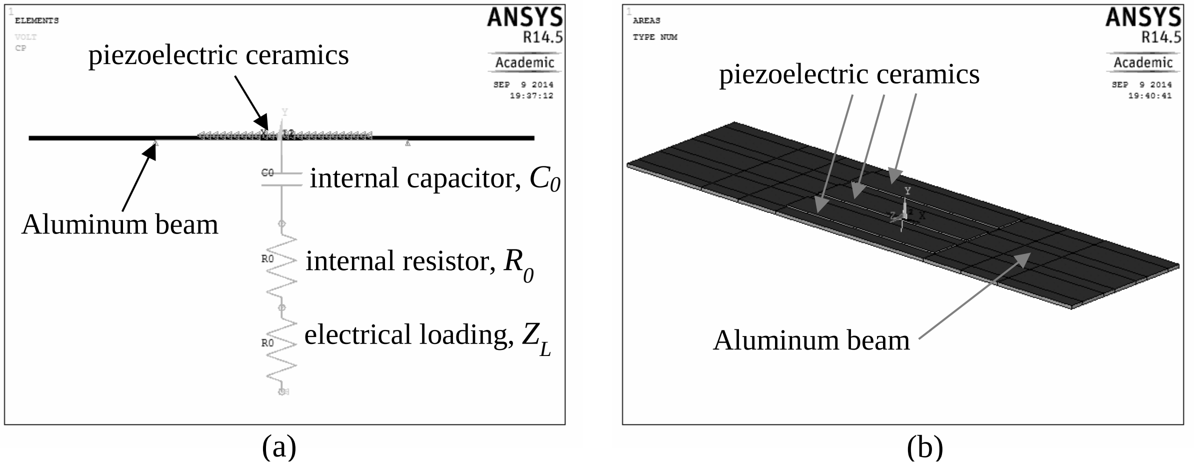

Figure 2-13 FEM model and physical model of drive unit

To verify the performance of proposed SHM, the drive unit is designed to bind three pieces of piezoelectric ceramics on an aluminum beam on a four-point-bending fixture, which confines the y-direction displacement on the external fixture and applies loadings on the internal fixture. To study the dynamic behavior of the beam, modal, harmonic and transient analyses are carried out.

Modal analysis

Modal analysis is carried to determine the natural mode shapes and natural frequencies of the four-point-bending structure during free vibration. Based on the Euler-Bernoulli beam theory, the theoretical solutions of natural frequencies were given in Eqn.(2-65) and mode shapes were given in Eqn.(2-64). The results of the first six modes derived from the Euler-Bernoulli beam model are generalized in Table 2-5.

Table 2-5 Natural frequencies and mode shapes of a four-point-bending structure by theoretical model

Mode No.	Natural frequency	Mode shape
1	212 Hz	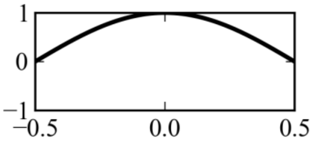
2	850 Hz	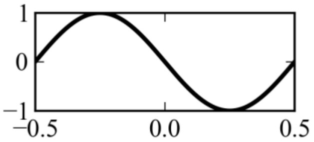
3	1911 Hz	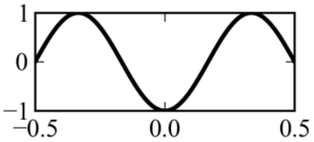
4	3400 Hz	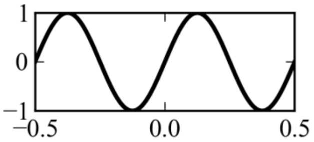
5	5309 Hz	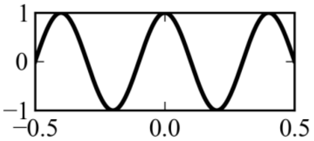
6	6370 Hz	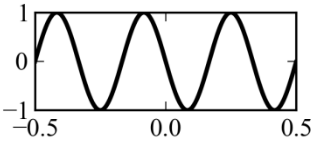

To verify the theoretical model shown in Table 2-5, a 3D FEM model shown in Figure 2-13 is used to carry out modal analysis. The natural frequencies and mode shapes of the first six modes are generalized in

Table 2-6. The mode shapes from FEM appear that the structure behave like a plate in higher frequency modes. This 3D modal analysis is parameterized and programmed by APDL. Detailed APDL scripts are list in Appendix I and Appendix II. Since the modal analysis consider mechanical behaviors only, the electric potential on upper and lower electrodes Appendix I have to be set to zero.

Since the Euler-Bernoulli beam model does not consider the variation of displacement u_z along y-direction (beam-width direction), the natural frequencies and mode shapes obtained from beam model miss the third, fifth and sixth modes obtained from FEM model. Considering the mode shapes along x-axis only, the natural frequencies and mode shapes obtained from Euler-Bernoulli model and FEM roughly agree to each other around 212 Hz, 1911 Hz, and 3439 Hz, which the mode shapes in y-axis do not involved.

Table 2-6 Natural frequencies and mode shapes of a four-point-bending structure by FEM

First mode: 245 Hz	Second mode: 1406 Hz
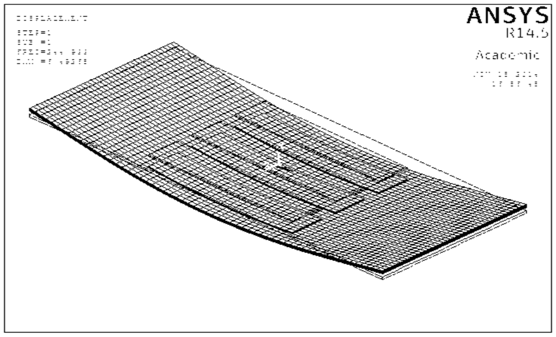	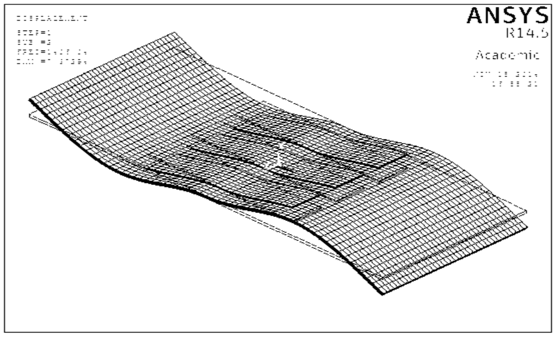
Third mode: 1597 Hz	Fourth mode: 1903 Hz
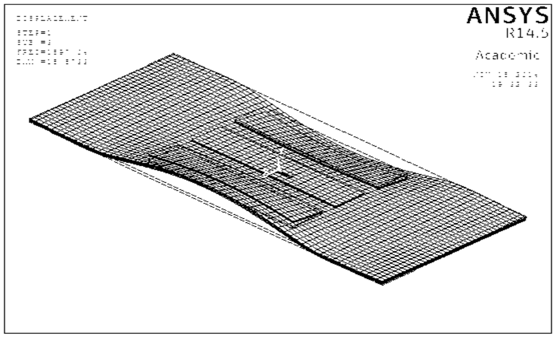	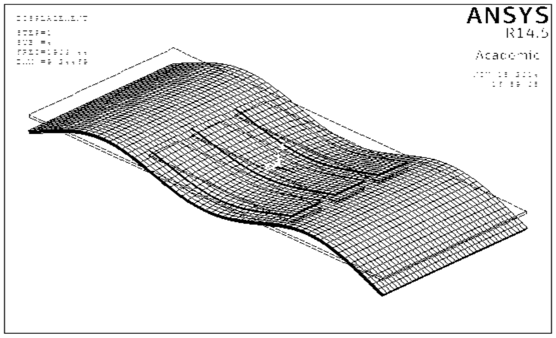
Fifth mode: 2381 Hz	Sixth mode: 3439 Hz
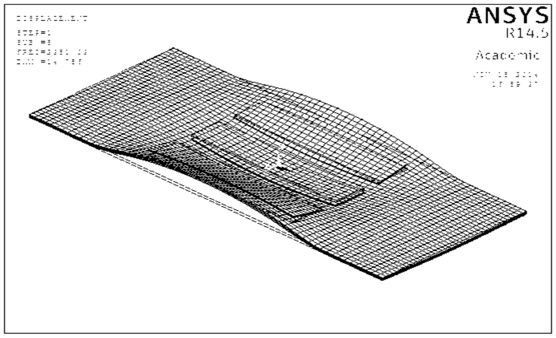	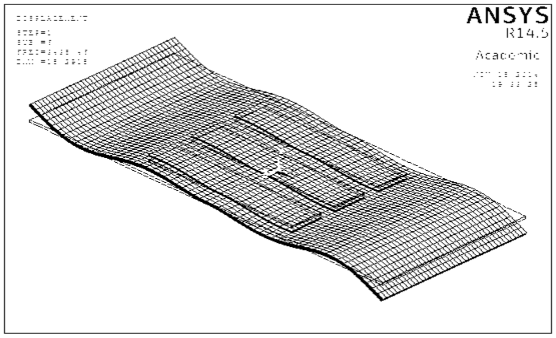

Harmonic analysis

Harmonic analysis was carried out to test the frequency response of displacement at mid-span of four-point-bending beam and output voltage across electrical loadings, while we apply harmonic loading at the internal fixture from 1 Hz to 3000 Hz.

Figure 2-14 shows the frequency response of the displacement at mid-span obtained from theoretical model (Eqn.(2-80)) and FEM results. This 3D harmonic analysis is parameterized and programmed by APDL. Detailed APDL scripts are list in Appendix I and Appendix III.

Both approaches result to the first resonant frequency at around 200 Hz, which is the first natural frequency we obtained by theoretical model in Table 2-5 and FEM in Table 2-6. The external force applied to the beam by four-point-bending fixture does not drive the mode shapes that are asymmetric to the mid-plane of the beam; therefore, the beam is not resonant from 200 Hz to 1900 Hz. The beam reaches another resonant state at around 1900 Hz, which is the third natural frequency from Euler-Bernoulli beam model, or the fourth natural frequency from FEM. Since we use 3D element to build up the finite element model for beam structure, the anti-resonant frequency at around 2300 Hz and resonant frequency at around 2400 Hz is the natural frequencies specific for a plate structure, which consider mode shapes along y-axis (beam-width direction). The Euler beam model consider the mode shape in *x*-direction (length direction) only, the resonant frequencies at 2400 Hz does not appear by Euler-Bernoulli model.

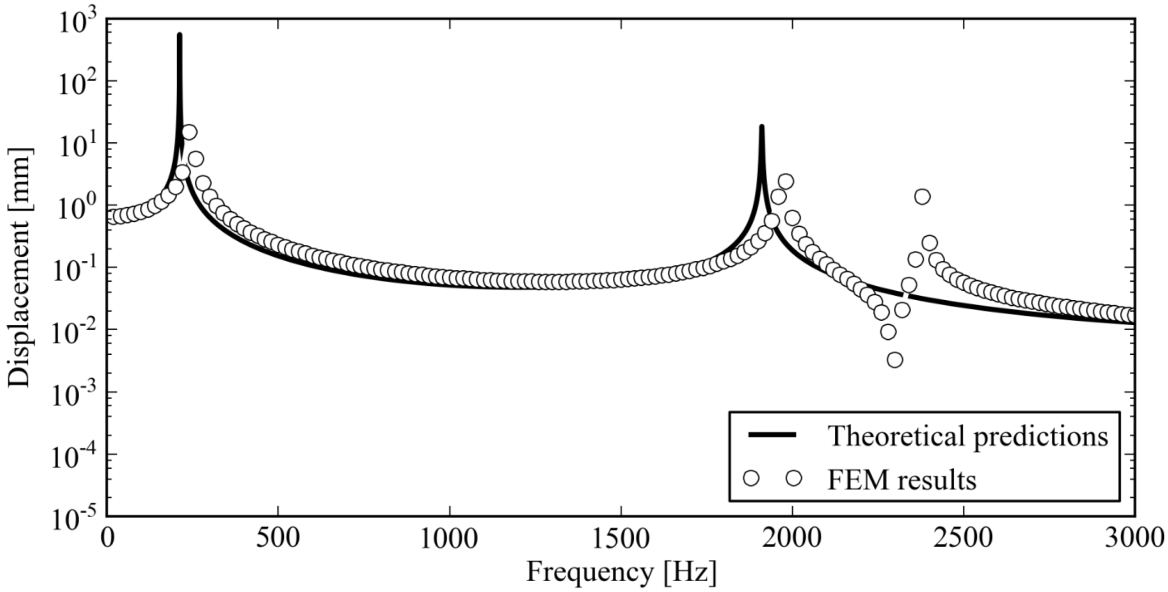

Figure 2-14 Frequency response of the displacement at mid-span of the beam

Figure 2-15 shows the frequency response of the output voltage obtained from theoretical model (Eqn.(2-81) and (2-80)) and FEM results. Both approaches result to the first resonant frequency of output voltage at around 200 Hz, which is the first natural frequency we obtained by theoretical model in Table 2-5 and FEM in Table 2-6. The external force applied to the beam by four-point-bending fixture.

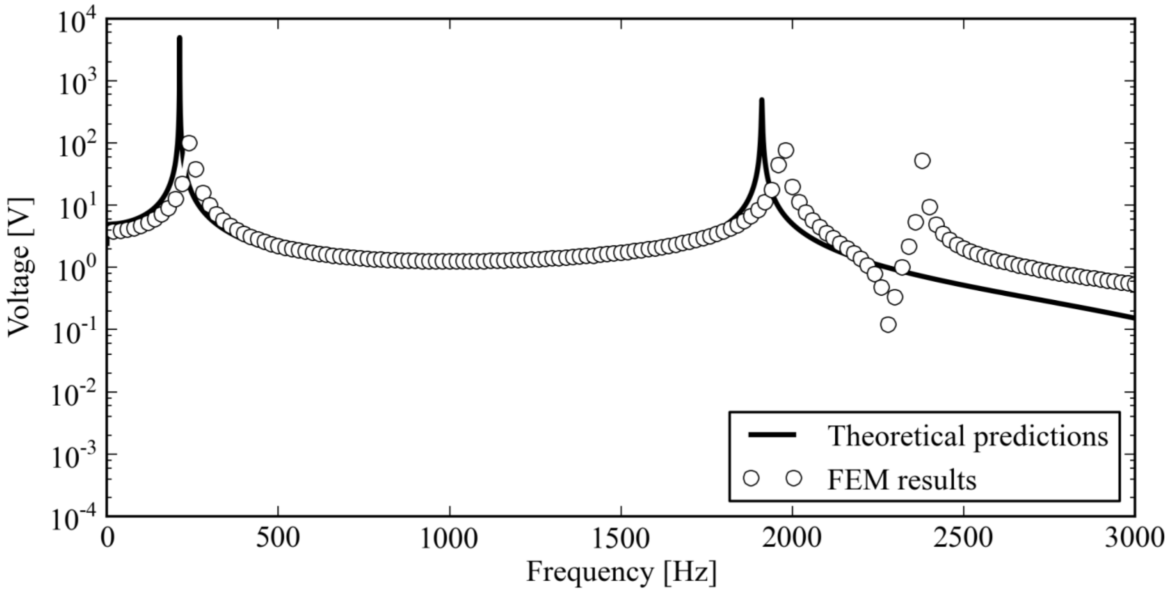

Figure 2-15 Frequency response of the output voltage

Transient response

A transient response was conducted by APDL to set a sinusoidal displacement on the inner span of the four-point-bending fixture and induced -27.5 MPa ~ +27.5 MPa stress in *x*-direction on the top-most surface of piezoelectric ceramics. This 3D transient responses are parameterized and programmed by APDL. The transient response was conducted by implicit dynamics. The sinusoidal input excitations were discretized into six hundred timesteps in each periods and stored these data in an array by an APDL `*DO-*ENDO` loop. The sinusoidal excitations are applied to the structure by another APPDL `*DO-*ENDO` loop. Detailed APDL scripts are list in Appendix I and Error! Reference source not found.

The open-circuit output voltage response induced by the sinusoidal bending stress on the piezoelectric ceramics is shown in Figure 2-16, which illustrates that -27.5 MPa ~ +27.5 MPa stress in *x*-direction on the top-most surface of piezoelectric ceramics induces an amplitude of ±75 V output voltage from the piezoelectric drive unit without electric loading. The mechanical loading and electrical output is in-phase.

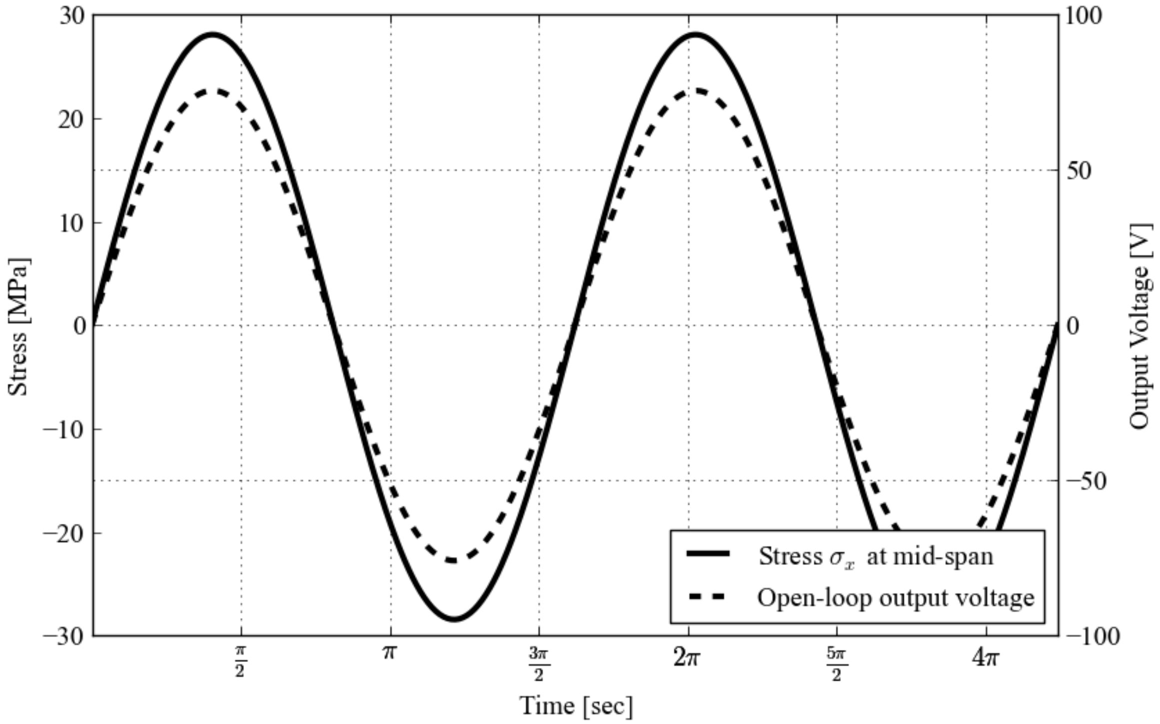

Figure 2-16 Transient open-loop output voltage response of drive unit induced by bending stress

Figure 2-17 shows the transient response of voltage drop on load induced by the sinusoidal bending stress on the piezoelectric ceramics. The phase angle of voltage drop on loads presents π/3 radian phase lead to the corresponding stress, which matches 69º, the results from Eqn.(2-

91), where ω = 2π×1 Hz, C=10.4×3^{pieces} nF, Z_L=1 MΩ. Noted that the simulations set poling in –z direction, which is opposite to the theoretical model derived in Eqn.(2-90) and Eqn.(2-91) .

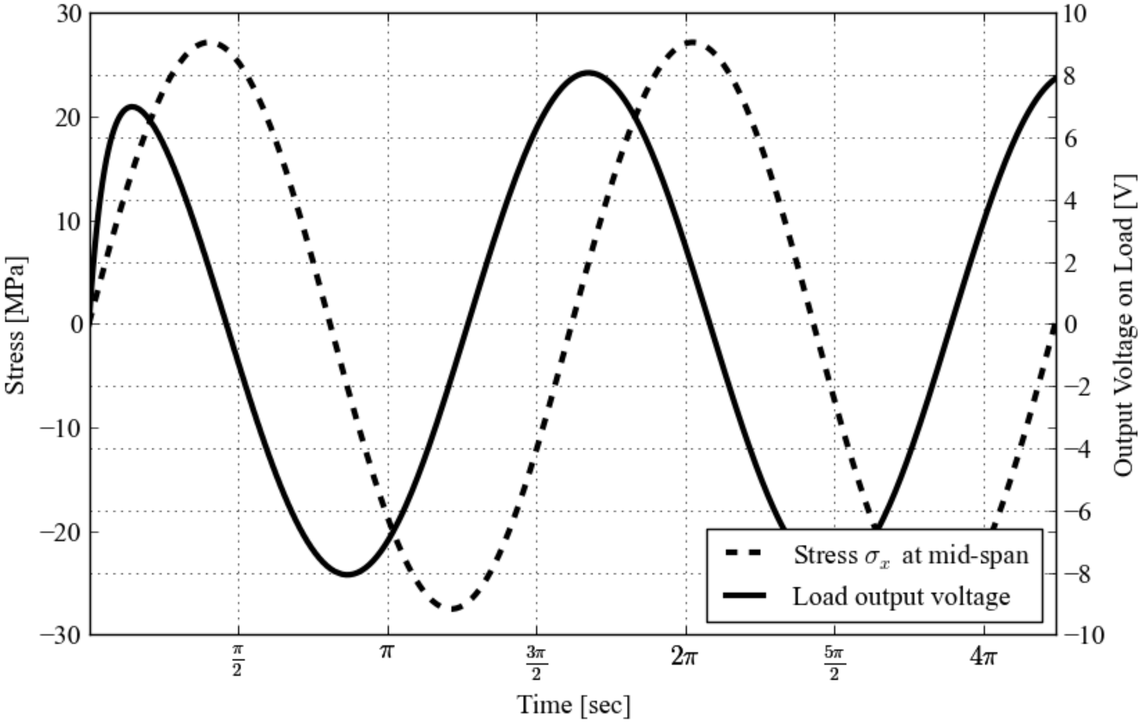

Figure 2-17 Transient close-loop output voltage response of drive unit

2.7 Conclusion

In this chapter, we introduce the piezoelectric effects and the constitutive equations to describe the electromechanical coupling effect of piezoelectric materials. We also review the literature that develop models of piezoelectric material to devices for energy harvesters. Then, we developed coupled electric circuit equations and coupled mechanical equations to model the electro-mechanical coupling effects that mechanical and electrical behaviors interact to each other. Based on these theoretical models, we derive the natural frequencies, mode shapes, and frequency response functions of output voltage and mid-point displacement of the piezoelectric patch mounting on the beam in the four-point-bending fixture. A 3D FEM model was also built up to perform the modal analysis and harmonic analysis as well as transient response under sinusoidal excitations at low mechanical frequency. The results of the theoretical model and FEM show agreement. We also drove the beam by four-point-bending fixture at a specific frequency experimentally to verify the output voltage from the piezoelectric based drive unit and the theoretical predictions and FEM results agree to the experimental results.

Chapter 3 Characteristics of Ferroelectric Materials

Ferroelectric materials, by definition, possess reversible spontaneous polarization by the application of an external electric field below the Curie temperature. Once the external electric field is removed, the polarization is not withdrawn but a certain amount of polarization still remained named as remnant polarization. While a repeatable cyclic external electric field is applied, the loss of remnant polarization follows with the number of cycles of the external electric field. The polarization fatigue is the fundamental concept that the ferroelectric based sensor unit of the proposed SHM system. This counts the number of cycles of the mechanical excitation on the structural component. The mechanical excitation drives the drive unit of the proposed SHM system and sending out electrical excitation to the sensor unit, which gives polarization fatigue to the ferroelectric based sensor unit in every repetition of cyclic electric field.

In this chapter, we will review the polarization fatigue phenomenon of ferroelectric thin film. Then, we will introduce the polarization vs. electric field (*P-E*) loop, which has been a useful diagnostic tool to study the polarization behavior of the ferroelectric material ever since ferroelectricity was discovered. Next, we will introduce the polarization fatigue phenomenon, the experimental setup to record P-E loop, the fabrication process of the proposed sensor unit, as well as the measurement system to conduct polarization fatigue. The experimental result will then be provided.

3.1. Literature Review

The phenomenon of ferroelectricity was first discovered in 1921 by Valasek [64] who was investigating the dielectric properties of Rochelle salt ($NaKC_4H_4O_6 \cdot 4H_2O$) and published the first hysteresis curve of Rochelle salt. The discovery of ferroelectric fatigue was reported by

Merz and Anderson in 1955 [65] who investigated the electrical properties of single-crystal $BaTiO_3$ influenced by an AC electric field. The factors that influence the polarization fatigue experimentally have been studied by a large body of experiments. These experimental characteristics are generalized as the amplitude of the driving electric field (or voltage), frequency of the driving electric field (or voltage), and the material of electrodes, etc.

The effects of the driving electric field amplitude on polarization fatigue of PZT films have been widely studied. The majority of experiments showed that the higher electric field induced stronger polarization fatigue [66][67][68][69][70][71][72]. However, the minority of research found that the polarization fatigue is relatively independent to the driving electric field amplitude [73][74].

The effects of driving frequency on polarization fatigue of thin film also showed a certain inconsistency in experiments. Some researchers observed that there is no evident frequency dependence of the polarization fatigue behavior [67][68][74]. While experiments from others showed that the lower the frequency of driving field, the higher the polarization fatigue is induced [73][75][76][77][78].

The effect of electrodes material was also found to be a critical factor to the polarization fatigue of ferroelectric films for PZT thin films in particular. Al-Shareef *et al*. [79] conducted experiments to investigate the polarization fatigue characteristics of Pt/PZT/Pt and RuO_2/PZT/RuO_2 capacitors and found that RuO_2/PZT/RuO_2 capacitors resist more polarization fatigue than Pt/PZT/Pt do. The results appear that the conductive oxide electrodes enhance the resistance of the polarization fatigue of PZT films more than conductive electrodes.

One of the major failure mechanisms of ferroelectric thin film is polarization fatigue, which indicates that the reduction of the remnant polarization of ferroelectric thin films is induced by the number of polarization reversals resulting from the reversed external electric field applied on the ferroelectric thin film.

Researches have generalized that the mechanisms of the polarization fatigue are induced by the domain-wall spinning, microcracks, etc.

Warren *et al*. [80] presented that the electronics charges are trapped and stabilized at domain boundaries, and the domains are pinned by the presence of these trapped electronics. These trapping electronic charges do not contribute to the polarization of the thin film. Increasing numbers of domains are pinned induced by the accumulation of the trapped electronic charges, the polarization of the PZT film is suppressed [81][82][83].

Microscopic cracks that induce polarization fatigue have long been observed as well, especially in bulk ferroelectric materials [84][85]. The reversal of the external electric field induces the internal stress with the sample resulting to microcracks. Microcracks, void within the samples, also mean the discontinuity of the materials. Increasing number of microcracks, which do not contribute to polarization switched, causes the polarization loss with increasing number of cycles of driving electric field.

3.2. Ferroelectricity

The most prominent behaviors of ferroelectric materials are the nonlinearity among the polarization P and the applied electric field E, which form a hysteresis loop. A typical hysteresis loop for ferroelectric material is shown in Figure 3-1. While the increasing applied electric field E is small, the polarization P increases linearly followed by portion 0A because the applied electric field E is not large enough yet to orient the domains. Once a larger electric field E is applied, polarization P induced by electric field E increases nonlinearly because polarization in all domains within the ferroelectric materials start to orient toward the direction of the applied electric field E. While the polarization P in almost every domain is already aligned toward the direction of the applied electric field E, it reaches the saturation state, where the saturated polarization increases slowly and linearly while applied electric field E increases. The linearity at high-range shows that the materials possess somewhat dielectric behaviors while the polarization of every domain is already aligned toward the applied electric field E. The spontaneous polarization P_s is defined by 0E, where E is the extrapolated point from the extension of the linear portion. If the applied electric field E is gradually withdrawn, the polarization P decreases followed by the path BCDE and intersects the y-axis at remnant polarization P_r, which means the polarization does not vanish under the absence of the applied electric field E. The remnant polarization P_r can only be removed by inverting the electric field until the field reaches a coercive field E_c (portion 0R on electric field axis). By further increasing the reverse electric field, realignment of the orientation of the dipoles in the opposite direction is achieved. Finally, when inverting the applied electric field once more, a complete hysteresis loop is obtained.

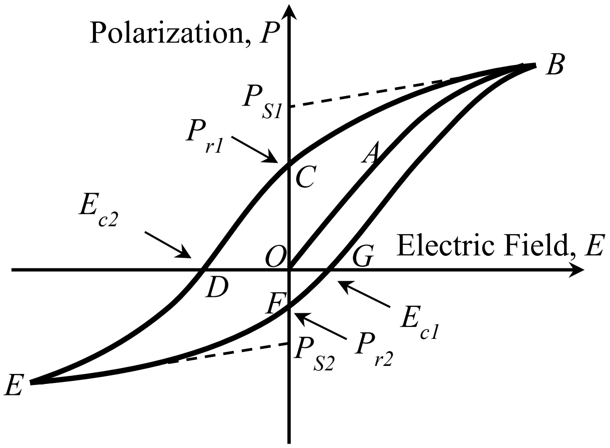

Figure 3-1 Hysteresis loop of ferroelectric materials

3.3. Ferroelectric thin film based sensor unit

To make the sensor unit of the proposed SHM system with high piezoelectric constants, a sol-gel process route shown in Figure 3-2 is used to fabricated PZT thin films with high piezoelectric performance by AIST (The National Institute of Advanced Industrial Science and Technology, Japan). The fabrication process is shown as follows:

Step A: A silicon wafer of oriental <100> with 500 μm in thickness was prepared for the substrate for the PZT thin films.

Step B: The Silicon wafer was first annealed at 1000°C with an oxidation environment furnace. A 200 nm-thick silicon dioxide was then grown on a silicon wafer.

Step C: An E-beam sputtering system was then employed to grow the bottom electrode. A 100 nm-thick layer of platinum was coated after a 50 nm-thick layer of titanium was coated on the surface of an oxide film. This was needed for the enhancement of a strong interface bonding between silicon and platinum.

Step D: A PZT sol-gel was spun and deposited repeatedly on the surface of this Pt/Ti/SiO_2/Si substrate and patterned by conventional photolithography.

Step E: Annealing the as-deposited films at 300°C makes the PZT films highly dense. The precursor solution was coated by spin coating on the surface of PZT/ Pt/Ti/SiO_2/Si substrate.

Step E to Step D repetitions: A PZT thin film in form of sol-gel was deposited on the surface of this substrate by spin-coating repeatedly, followed by annealing to make the as-deposited film highly dense. The precursor solution is coated by spin coating on the Si-wafer surface. Each spin coating is followed by an annealing process. Coating/annealing to form the PZT thin film of 0.1μm in thickness each time was repeated around twenty times.

Step F: The PZT films on the substrate were then treated by sintering at 700°C. As-processed PZT film has uniform thickness of around 2.0 μm.

Step G: Reactive Ion Etching (RIE) method was applied to make PZT film ranging from 0.3 to 2.0 μm in thickness. Then, on the top surfaces of the sensors platinum electrodes were deposited 100 nm in thickness. The schematic and photo of ferroelectric-based sensor unit is shown then shown in Figure 3-3 and Figure 3-4.

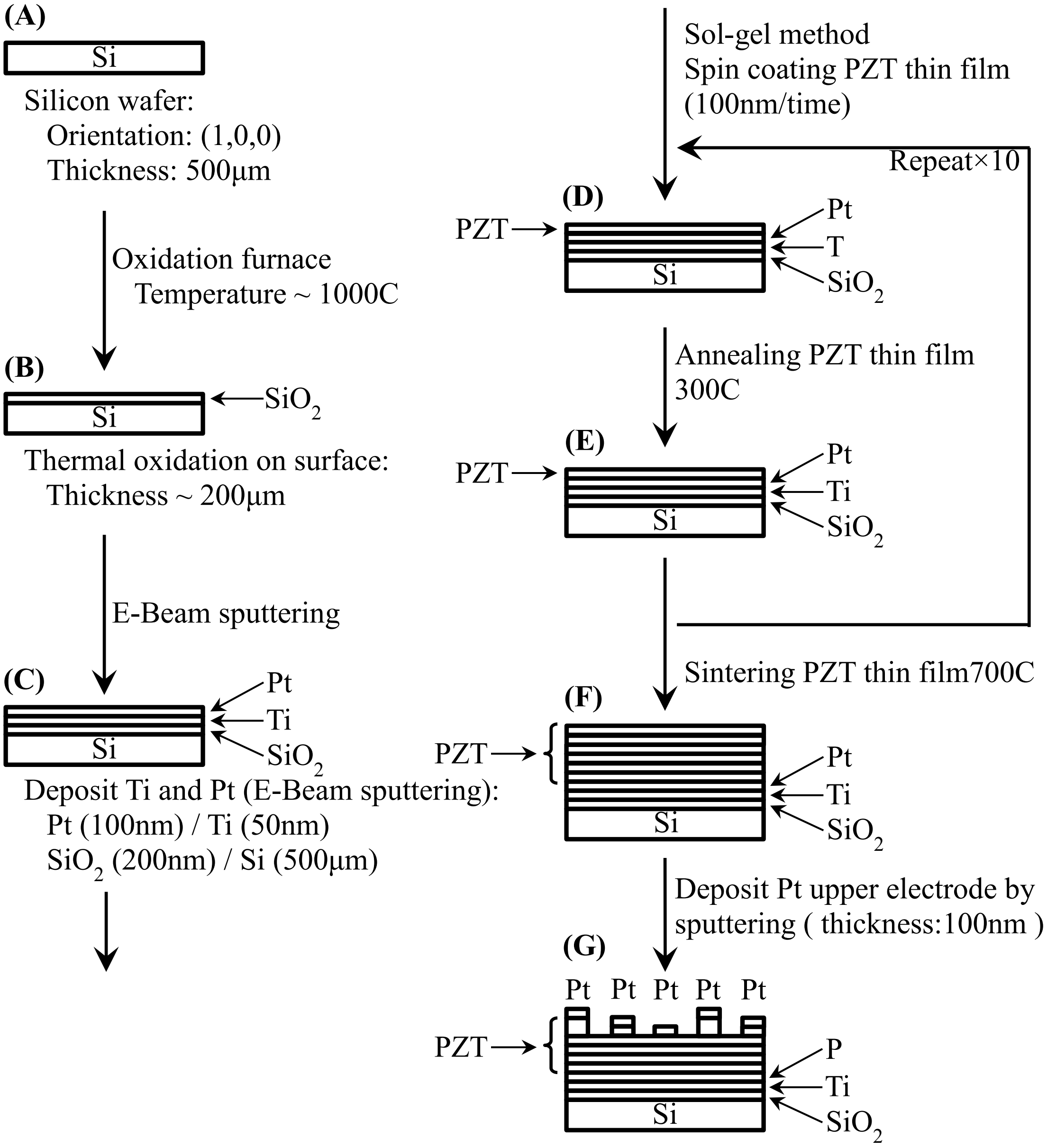

Figure 3-2 Process route for arrayed sensor system for the uniform thickness type PZT film (by AIST).

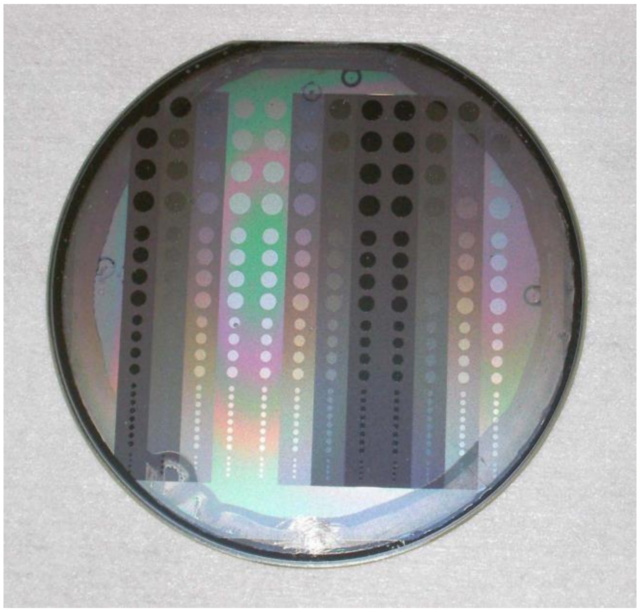

Figure 3-3 Sensor PZT units manufactured by AIST

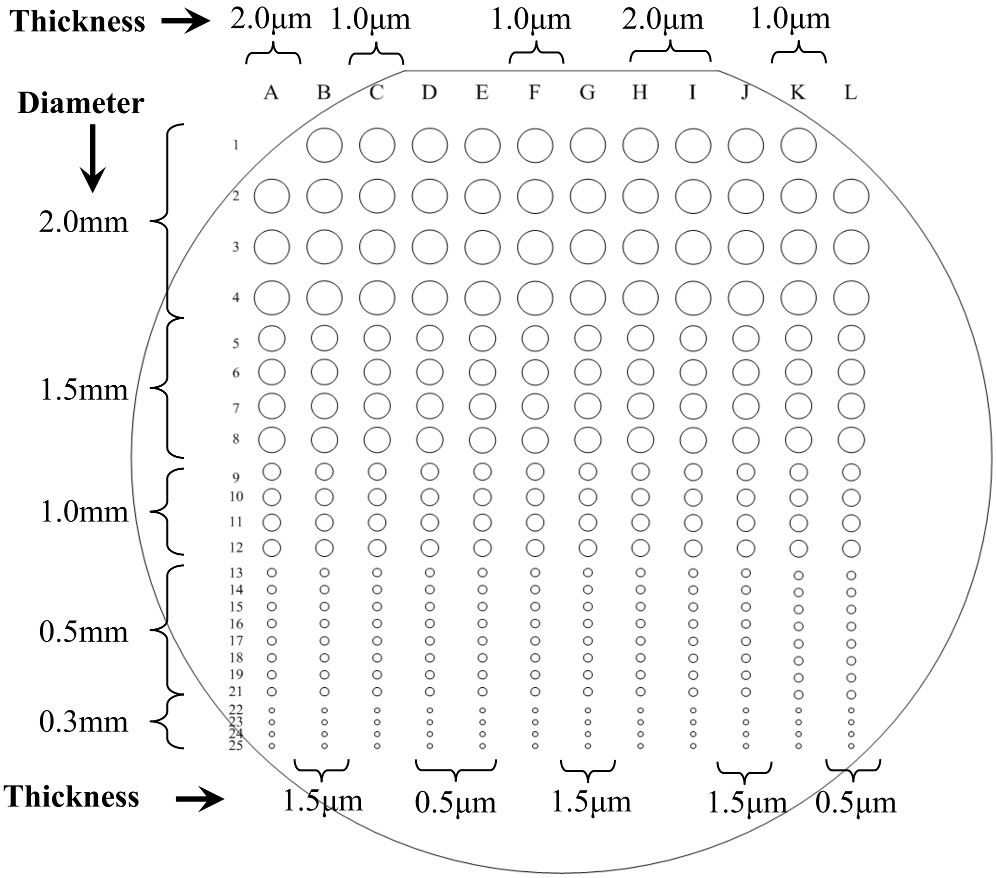

Figure 3-4 Dimensions of daughter sensor PZT units

3.4. Polarization Fatigue

The main application of hysteretic behavior of the ferroelectric thin film, relating polarization P and applied electric field E are nonvolatile memories. There is a nominal threshold, coercive electric field E_c specifically, above which makes polarization of the ferroelectric materials change of sign. The two zero-electric-electric-field values $\pm P_r$ are equally stable, and either of the two states of polarization could be read as a “1” or a “0”, a good candidate for memory devices. Since the hysteresis loop of ferroelectric materials shown in Figure 3-1 indicates that no external electric field is required to maintain these two states, the memory is nonvolatile.

The polarization fatigue is the microscopic mechanism of ferroelectric thin films and it limits the applications of ferroelectric memory. However, the polarization fatigue phenomenon provides another application of a sensor for a cycle counter device, since it means that the remnant polarization (average polarization while no external electric field) is a function of the number of the reversals of the applied electric field.

Polarization fatigue of ferroelectric materials is defined as the loss of the remnant polarization P_r while the material is undergoing a cyclic external electric field E. Figure 3-5 illustrates that the area of the hysteresis loops evolves to get smaller while we apply more number of cycles N of the external electric field. The corresponding remnant polarization P_r of each hysteresis loop decays as a function of the number of cycles N of the applied electric field, where subscripts k, m, and n denote the specific numbers of cycles that the corresponding hysteresis loops are retrieved. This phenomenon of polarization fatigue has been investigated over the past decades to aid the development of ferroelectric thin film based random access memories, which has been reviewed in Sec. 3.1.

As we reviewed in Sec.3.1, even though several models have been presented for decades to modify the mechanism of polarization fatigue, the mechanisms of polarization fatigue are presently not well understood. Moreover, researchers conducted numerous experiments to clarify the parameters that affect the severity of polarization fatigue, but most of the experimental results showed inconsistency. To develop a reliable ferroelectric-based SHM system for cycle counter devices, an interface circuit electrically connected between drive and sensor units is required to condition the voltage signal induced by the stressed structural component. The measurement system for polarization fatigue will be introduced later this chapter and the interface circuit will be presented in the next chapter.

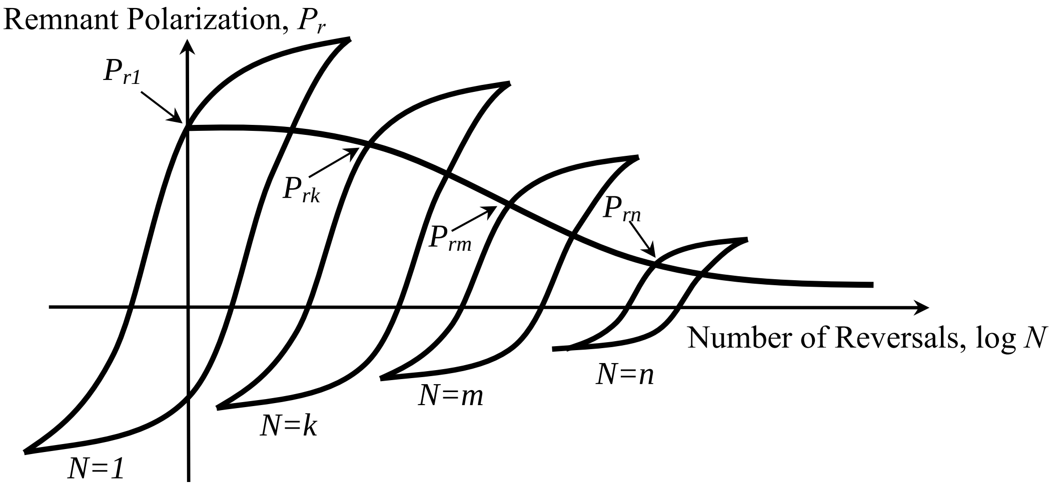

Figure 3-5 Polarization fatigue of ferroelectric materials

3.5. Experimental Setup

To develop a reliable ferroelectric-based SHM system, we built up an automatic measurement system polarization fatigue test to retrieve the polarization fatigue curves.

The presented measurement system is able to not only conduct millions of cycle polarization fatigue tests and retrieve those polarization curves for the SHM system, but also perform the proof-of-concept experiments, driving the structural component in random amplitudes and verify the accuracy of a ferroelectric-based cycle counter. The measurement system is built up based on Sawyer Tower circuit, a typical and fundamental approach to measure *P-E* loop of ferroelectric materials; several relay drivers to control the measurement procedures; MOSFET as a power amplifier for the relay drivers; a LabVIEW program to execute the measurement procedure; and a data acquisition device to send out or read the signals. They will be introduced in the following sections in chapter three.

3.5.1. Sawyer Tower circuit

The electric displacement for dielectric materials can be expressed as follows

$$\vec{D} = \varepsilon_0 \vec{E} + \vec{P} \text{ and } \vec{D} = \varepsilon_0 \chi_e \vec{E} \, , \qquad (3\text{-}1)$$

where ***D*** is the electric displacement , ***E*** is the electric field, ***P*** is the polarization, and ε_0 is the electric permittivity (dielectric constant) of free space, and χ_e is electric susceptibility of dielectric materials.

$$\vec{D} = \varepsilon_0 (1 + \chi_e) \vec{E} \, . \qquad (3\text{-}2)$$

For a dielectric material $\chi_e >> 1$ (for PZT-5, $\chi_e \approx 1750$), $\varepsilon_0 (1+\chi_e) \approx \varepsilon_0 \chi_e$, electric displacement ***D*** for dielectric materials can be simplified as follows

$$\vec{D} \cong \varepsilon_0 \chi_e \vec{E} \, , \qquad (3\text{-}3)$$

which leads to

$$\vec{D} \cong \vec{P} \qquad (3\text{-}4)$$

Coulomb's law for dielectric materials describes that the free charges ρ_f at position vector ***r*** induced by electric displacement ***D*** shows

$$\nabla \cdot \vec{D} = \rho_f (\vec{r}) \qquad (3\text{-}5)$$

Applying Gauss's law the divergence of electric displacement field is equal to its flux through a surface S which encloses a volume V as follows

$$\oiint_{s} \vec{D} \cdot d\vec{A} = Q \,. \tag{3-6}$$

The surface integration leas to

$$D \cdot A = Q \,, \tag{3-7}$$

where D is the electric displacement, A the area of surface electrode on the ferroelectric film, and Q is the amount of electric charges on the surface electrode.

Substituting Eqn. (3-4) into Eqn. (3-7), polarization P of the ferroelectric material then results to the follows

$$P = \frac{Q}{A} \,, \tag{3-8}$$

which is the surface charge density on the electrodes.

Sawyer Tower circuit

The Sawyer-Tower circuit [86] shown in Figure 3-6 for measurement of hysteresis loops of ferroelectric crystals is a practical circuit for studying the characterization of ferroelectrics and fundamental phenomena such as spontaneous polarization P_s, remnant polarization P_r, coercive electric field E_C (Figure 3-1) and polarization reversal mechanisms (Figure 3-5).

The original Sawyer-Tower circuit shown in Figure 3-6, applicable only for low loss and high polarization materials, consists of a standard linear-known-value capacitor C and an unknown sample capacitor C_P.

The x-channel of oscilloscope gets the voltage drop $V(t)$ applied to both C and C_P. In the case of $C >> C_P$ the voltage drop at C can be ignored and therefore the voltage V_P at C_P is nearly equal to the supply voltage $V(t)$. The proportionality between voltage V and electrical field strength E shows

$$E = \frac{V}{h}, \tag{3-9}$$

where h is thickness of the capacitor, which means that the voltage at the x-channel of oscilloscope can be taken as a measure for the electric field inside of the sample C_P with appropriate modifications by Eqn.(3-9).

The y-channel of oscilloscope reads a voltage drop that is proportional to the polarization of the sample C_P. The two capacitors C_P and C are connected in series and identical electric current flows through both elements, which means that both C_P and C carry the same amount of electric charge Q at any arbitrary time t. Because of the proportionality between voltage V_P and charge Q in the relation of $V_P=C_PQ$, by applying Eqn.(3-8), the voltage drop at C_P can be used as a measure for the charge of the capacity C_P as follows

$$P = \frac{V_P}{C_P A}, \tag{3-10}$$

where A is the surface electrode area of the capacitor.

The capacitance of standard linear-known capacitor C is independent of the applied voltage V.

A sinusoidal voltage $V(t)$ is applied to the Sawyer-Tower circuit. To display the P (polarization) – E (electric field) loop, y channel from the oscilloscope is plotted as a y-coordinate of the hysteresis loop, while the x channel from the oscilloscope is referred to as a x-coordinate of the hysteresis loop. With appropriate modification given in Eqn.(3-9) and Eqn.(3-10), The P-E hysteresis loop is then displayed.

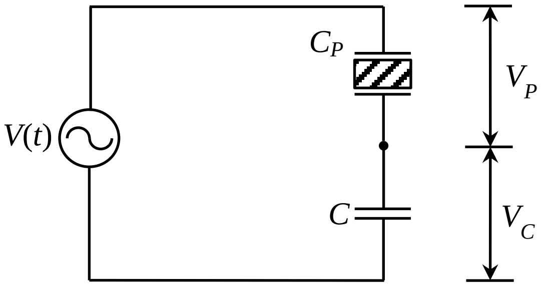

Figure 3-6 Sawyer Tower circuit to measure hysteresis loop for ferroelectric materials

The Sawyer-Tower circuit we use for the measurement is based on LabVIEW-NI DAQ system. A LabVIEW program is developed to send a cycle of sinusoidal signal with frequency of 10Hz to the Sawyer-Tower circuit as $V(t)$ in the previous discussion. Two input channels in the NI-DAQ reads the time-dependent V_P and $V(t)$ from the Sawyer-Tower circuit, which represent to polarization P and electric field E respectively.

3.5.2. Relay driver

To conduct the experiment, relays are used to switch between fatigue and measurement modes in the measurement system. A NI-DAQ system controlled by a LabVIEW program sends 5 V or 0 V to switch the relays ON/OFF. The rating voltage of the relays (OMRON G5V-1 3VDC) is 3 V, which is within the range that NI-DAQ can provide; however, the rating current of the relays (OMRON G5V-1 3VDC) is 50 mA, which is much larger than the 10 nA, that the NI-DAQ output channel can provide. To amplify the power of the signal from NI-DAQ output channel, a power MOSFET (IRF510, an n-channel enhancement-type of MOSFET) configured in Figure 3-7 is used to drive a relay to switch ON or OFF, and the diode in reverse bias across the relay's coil is used to eliminate voltage spikes created by the relay's coil and protect the relay circuit.

While the transistor's gate G receives a control voltage of 5 V from DAQ digital output channel, the transistor works in the active region. It allows drain-source current I_D to pass through the relay coil, causing the relay to switch states and through the MOSFET's drain-source region (D gate to S gate). The drain-source current I_D is formulated as

$$I_D = k(V_{GS} - V_t)^2, \tag{3-11}$$

where V_{GS} is the gate-source voltage, V_t (3.5 V for IRF510) is the threshold voltage (particular gate source voltage where MOSFET begins to conduct), and the construction parameter k is proportional to the width/length ratio of the transistor's channel and is dependent on temperature as well. The manufacturer of IRF510 gives k = 450 mA/V^2 at 25ºC in the datasheet.

Eq.(3-11) implied that the drain-source current I_D is independent of gate-source voltage V_{DS} , on the same loop of the circuit, but functions of gate-source V_{GS} voltage only, which acts as a voltage (V_{GS}) control valve. With no voltage V_{GS} applied to the MOSFET gate (G), the drain (D)-to-source (S) channel is closed, hence blocking current flow through the relay's coil. However, if a sufficiently large voltage V_{GS} is applied to the transistor's gate (G), the transistor's drain (D)-to-source (S) channel opens, allowing current I_D to flow through the relay's coil.

To drive the relay, the output channel of NI-DAQ should send at least 4.0 V to power MOSFET IRF510, which provides V_{GS} (4.0 V) larger than threshold voltage V_t (3.5 V) and makes the power MOSFET function in the active region. The drain-source current I_D is 100 mA determined by Eq.(3-11) and voltage drop V_{Relay} across the coil of relay is 6 V ($V_{Relay} = I_D \times r_{DS}$ = 1 mA×60 Ω = 6.0 V, r_{DS} = 60 Ω from OMRON G5V-1 3VDC datasheet), which are larger than the rating current and voltage of the relay (3 V, 50 mA) and capable of driving the relays.

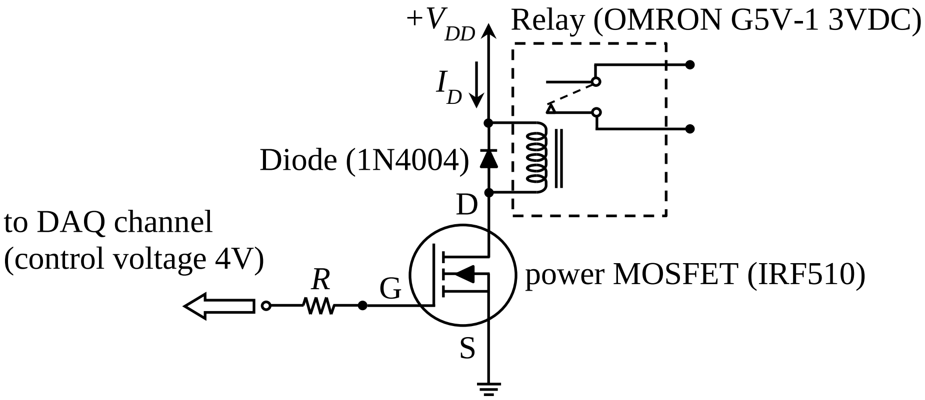

Figure 3-7 Common-source amplifier (an n-channel enhancement-type of power MOSFET) to drive a relay

3.5.3. Measurement system

The measurement system (shown in Figure 3-8 and Figure 3-9) is composed of the following elements:

1) Drive PZT unit on a four-point-bending beam excited by a universal testing machine (INSTRON 8521S),
2) A Sensor PZT unit: ferroelectric thin films on a silicon wafer,
3) A Sawyer Tower circuit,
4) Four relays driven by power MOSFETs for each,
5) Data acquisition system (NI-6221 BNC controller) ,
6) A NI-LabVIEW program.

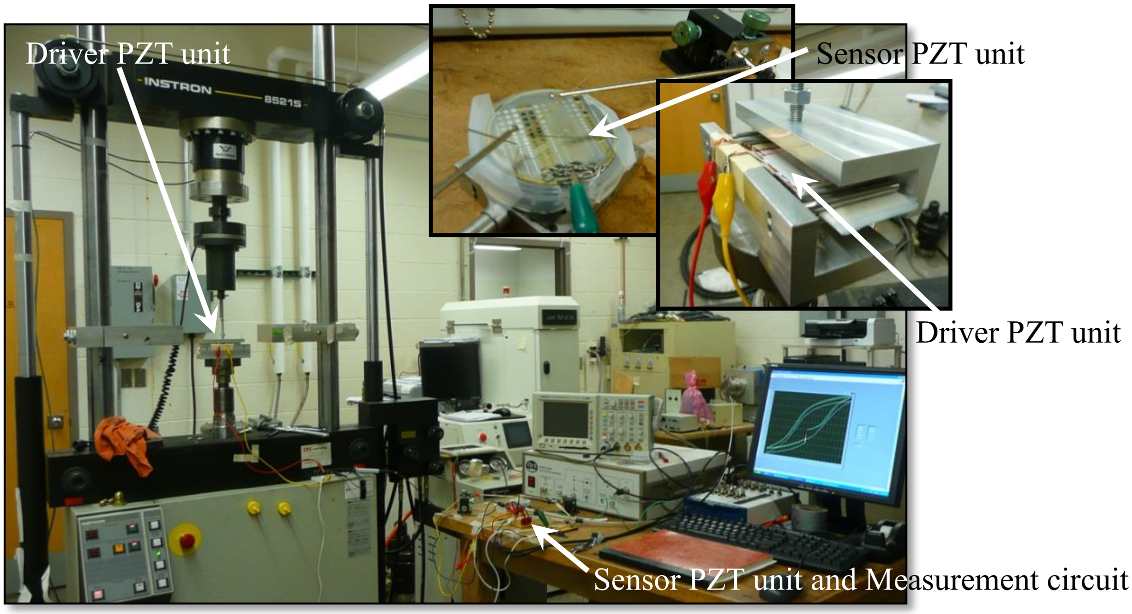

Figure 3-8 Photography of the measurement system

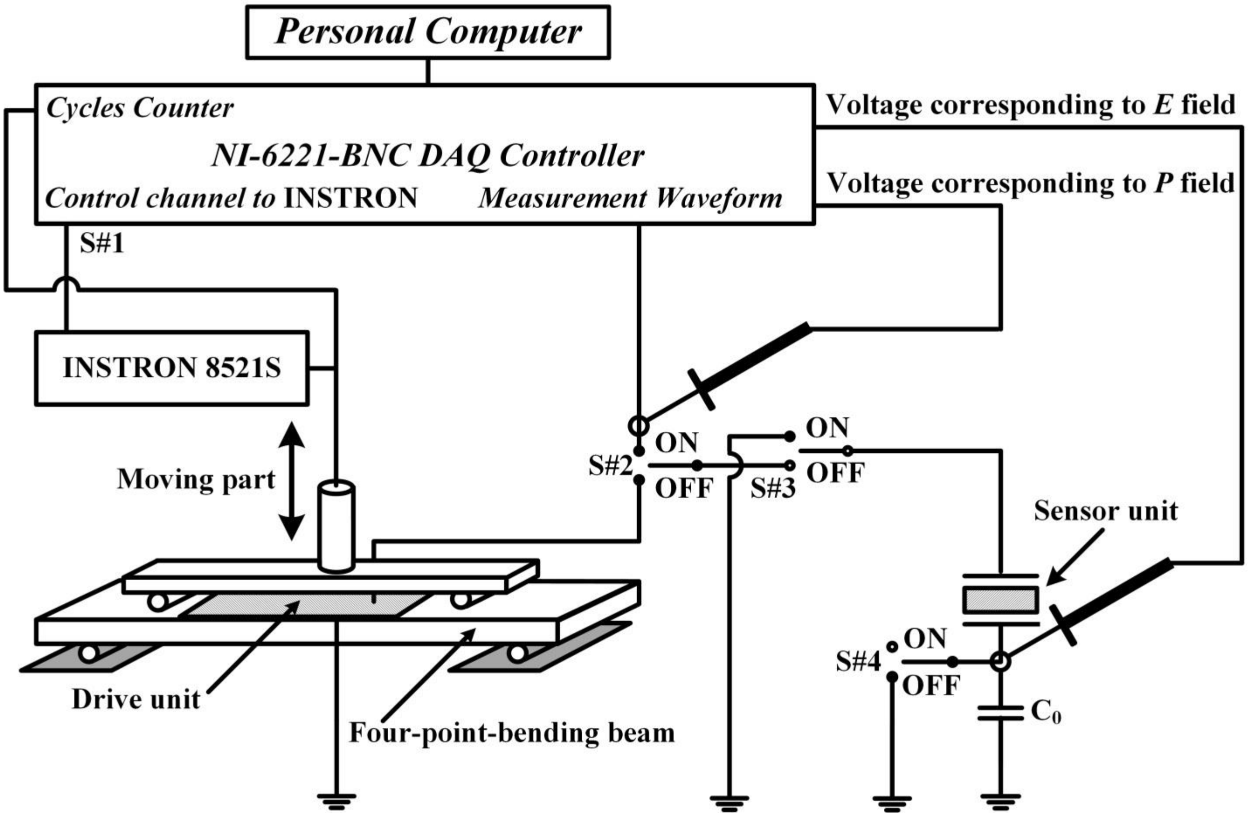

Figure 3-9 Measurement system for structural health monitor

The whole measurement system is controlled by a NI-LabVIEW program composed of four modes: fatigue mode, preset mode, pre-ground mode and measurement mode. The switch between each mode is controlled by a NI-LabVIEW program switching the relays in ON/OFF state following the truth table shown in Table 3-1. The measurement process is conducted following the flow chart shown in Figure 3-10. The system is in fatigue mode most of the time, keeps on poling and converse poling the sensor unit, except for some specific number of cycles when the program switches to the preset, pre-ground and measurement modes to collect the hysteresis loop. Then, the measurement system goes back to function in fatigue mode until the next specific number of cycles to collect hysteresis loop. The waveforms that applied to the sensor unit, including fatigue, preset, pre-ground, and measurement modes, are illustrated in Figure 3-11. Details of each mode are described one by one next.

Table 3-1 Truth table of relays control signal

	Switch #1	Switch #2	Switch #3	Switch #4
Fatigue Mode	OFF	OFF	OFF	OFF
Preset Mode	ON	ON	OFF	OFF
Pre-ground Mode	ON	OFF	ON	OFF
Measurement Mode	ON	ON	OFF	ON

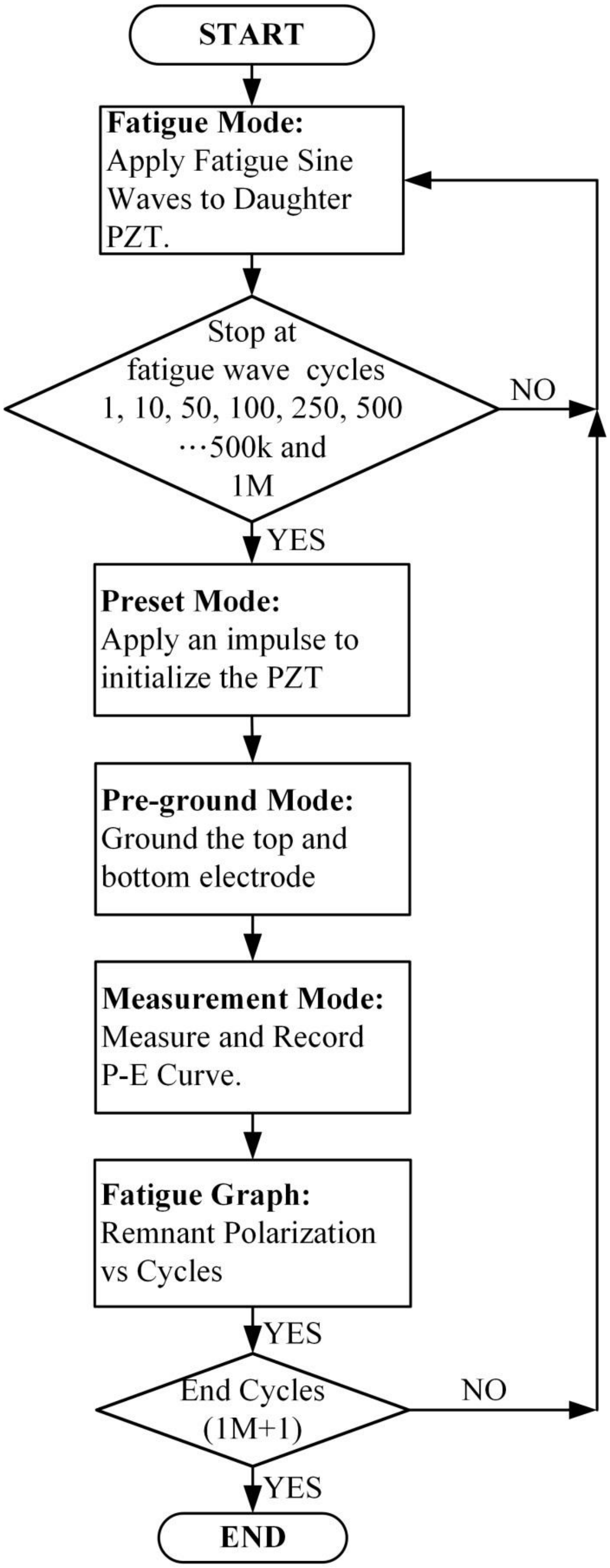

Figure 3-10 Flow chart of the measurement system

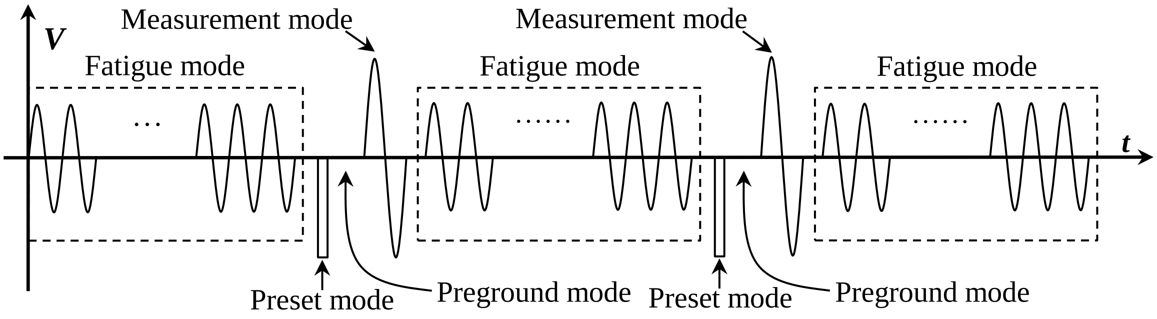

Figure 3-11 Sequence of polarization fatigue curve measurement

Fatigue mode

The experimental setup for the fatigue testing and its electric circuit is given in Figure 3-12, where a beam in a four-point-bending fixture is driven by a universal testing machine (INSTRON 8521S) to give a known frequency and a constant strain amplitude to the drive unit. During the vibration, the piezoelectric patches of drive unit generate electric charges sending to the sensor unit and repeat poling and converse poling the sensor daughter PZT.

The poling and converse poling cycles are counted by measuring the alternating time-dependent displacement excited by INSTRON 8521S. At a specific stop cycle *N*, the measurement system is set to measure the remnant polarization of the sensor daughter unit. Before the remnant polarization is measured in the measurement mode, preset mode is set by the application of a negative impulse.

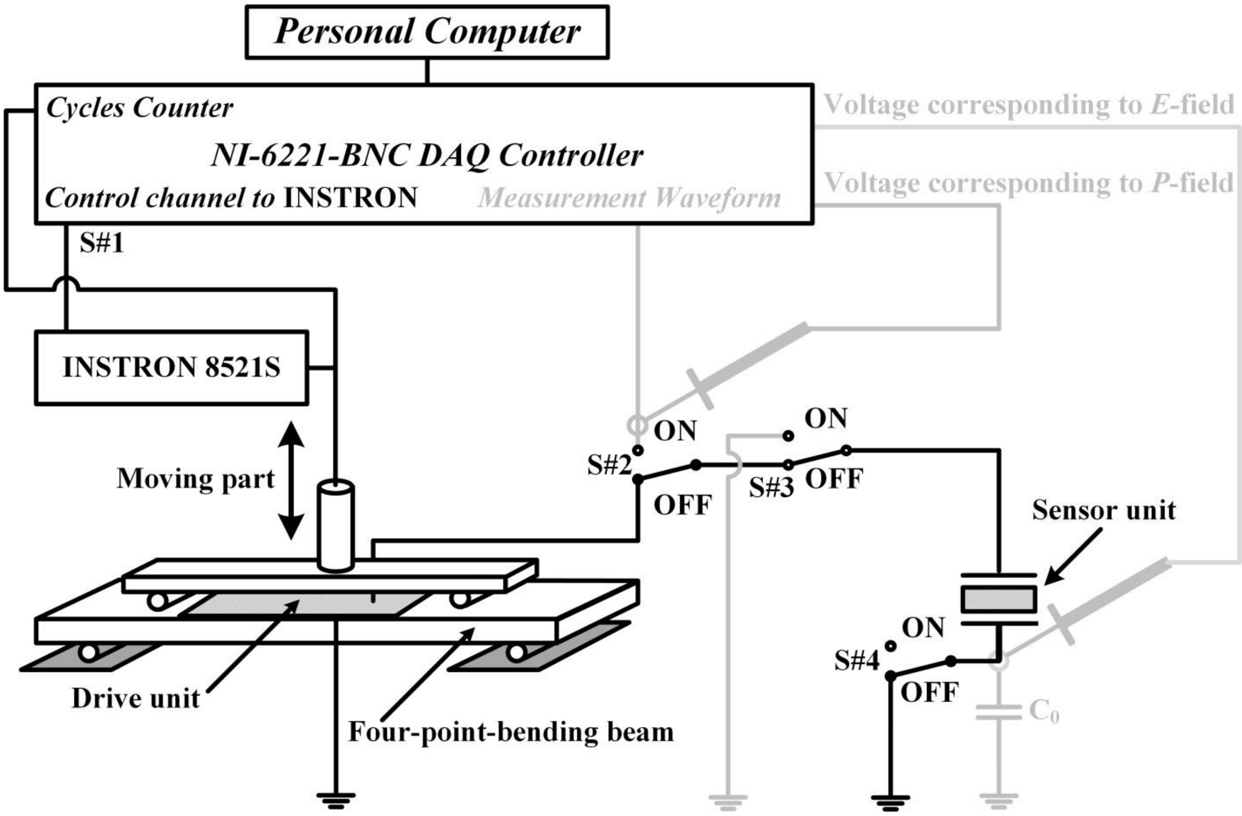

Figure 3-12 Fatigue mode of the measurement system

Preset mode

As the last cycle of the "Fatigue Mode" is finished, the applied electric field goes back to zero and the sensor unit performs negative remnant polarization. If the sensor unit is measured right after the fatigue mode, the hysteresis loop starts from a non-zero polarization. Also, the hysteresis loop starts from different non-zero polarization for each measurement, because the remnant polarization decreases in magnitude by the fatigue phenomenon. The different reference values for each measurement would complicate the data acquisition and data analyses. To solve issue, in preset mode shown in Figure 3-13, a negative impulse is applied to negatively polarize the sensor unit so that the polarization vector of each domain points downward. By applying the negative impulse, the "Preset Mode" initializes the sensor unit before the measurement mode starts so that the initial condition of each hysteresis loop is set to the same value.

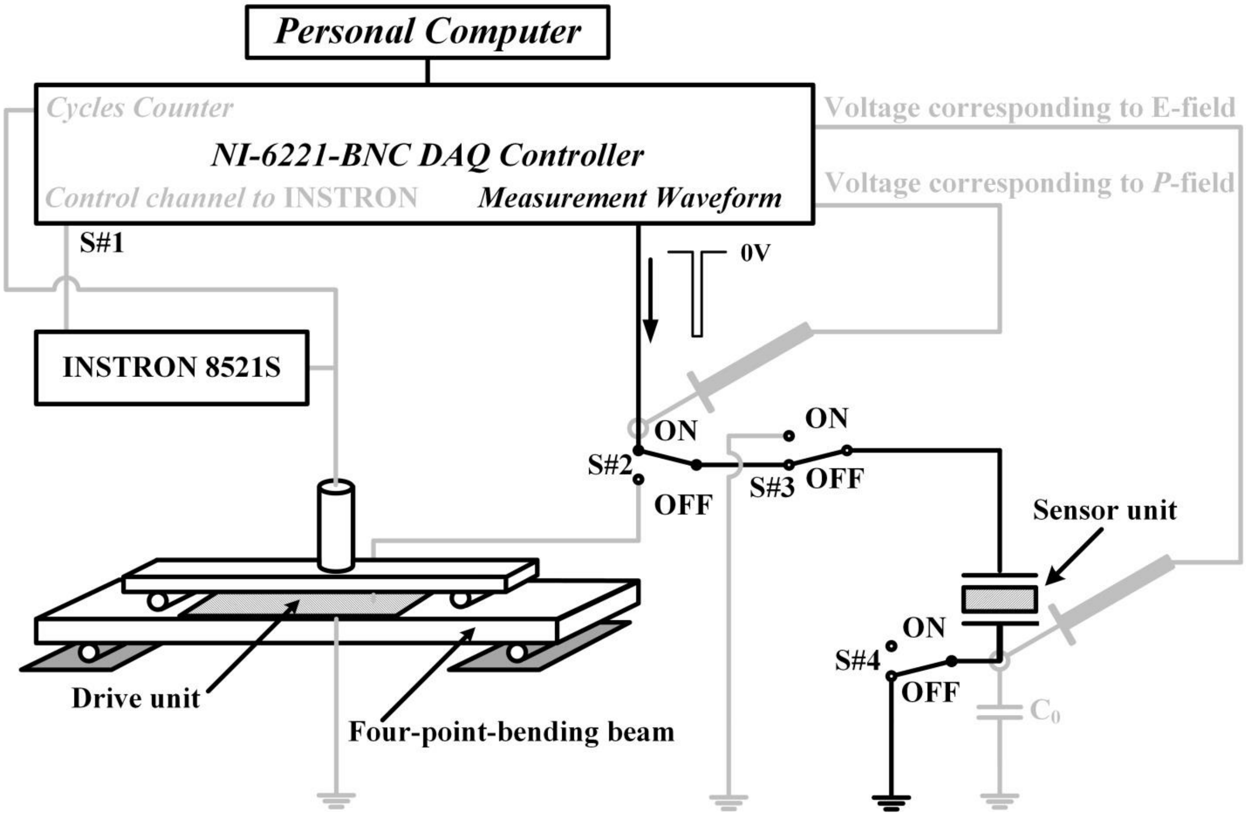

Figure 3-13 Preset mode of the measurement system

Pre-ground mode

After the preset mode, some charges, which may induce measurement errors, remain on the electrode of the sensor daughter unit. In the pre-ground mode shown in Figure 3-14, the top and bottom electrodes are connected to the ground and release the remaining charges.

Pre-ground mode

After the preset mode, some charges, which may induce measurement errors, remain on the electrode of the sensor daughter unit. In the pre-ground mode shown in Figure 3-14, the top and bottom electrodes are connected to the ground and release the remaining charges.

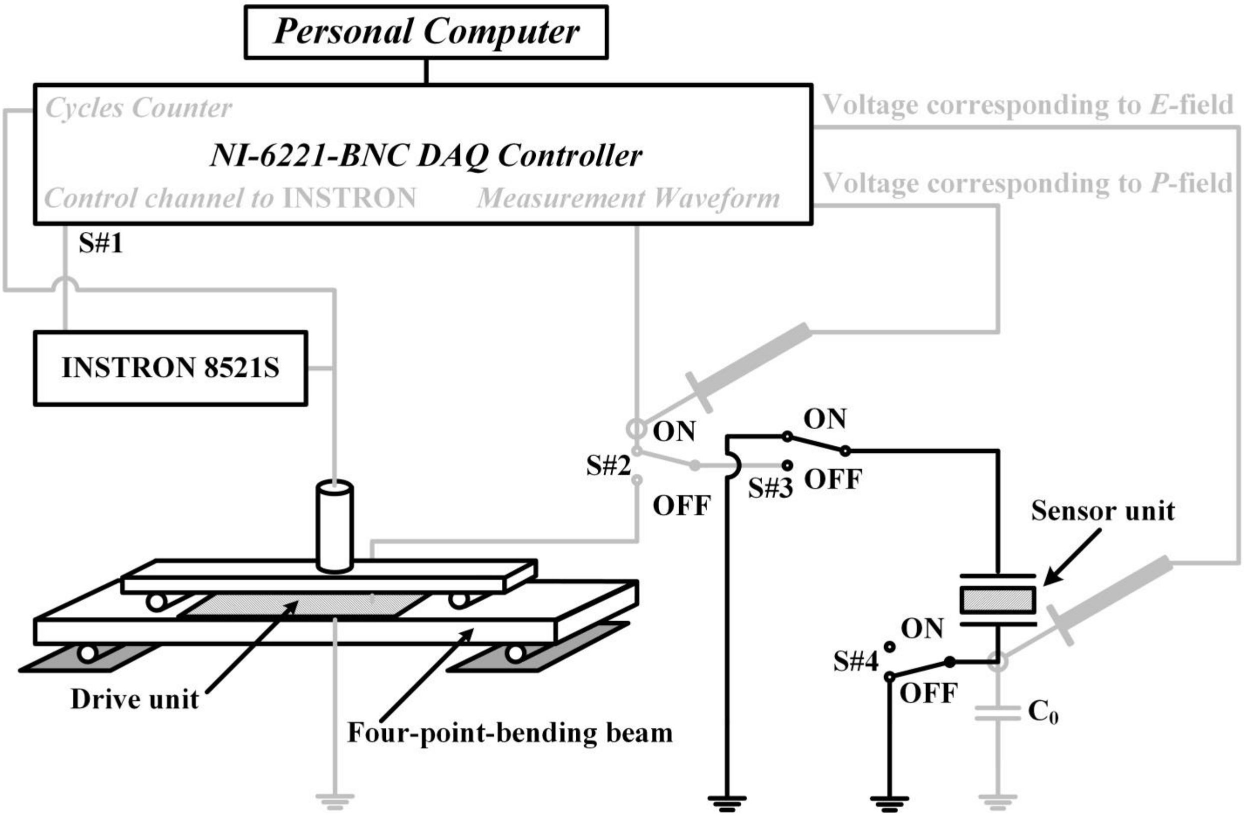

Figure 3-14 Pre-ground mode of the measurement system

Measurement mode

After the preset and pre-ground mode, the relays are switched to the measurement mode shown in Figure 3-15. The measurement waveform is sent by a data acquisition (DAQ) device to the Sawyer Tower circuit and the voltage corresponding to electric field E and polarization P are collected by DAQ device. This data can be sketched as a hysteresis loop. The number of cycles N and remnant polarization P_r are recorded to draw a fatigue graph when the measurement is done. Note that the voltage follower in the circuit is used to match the electrical impedance and provide large current to drive the relay circuits, while the non-converting amplifier amplifies the measurement waveform two times to the Sawyer Tower circuit.

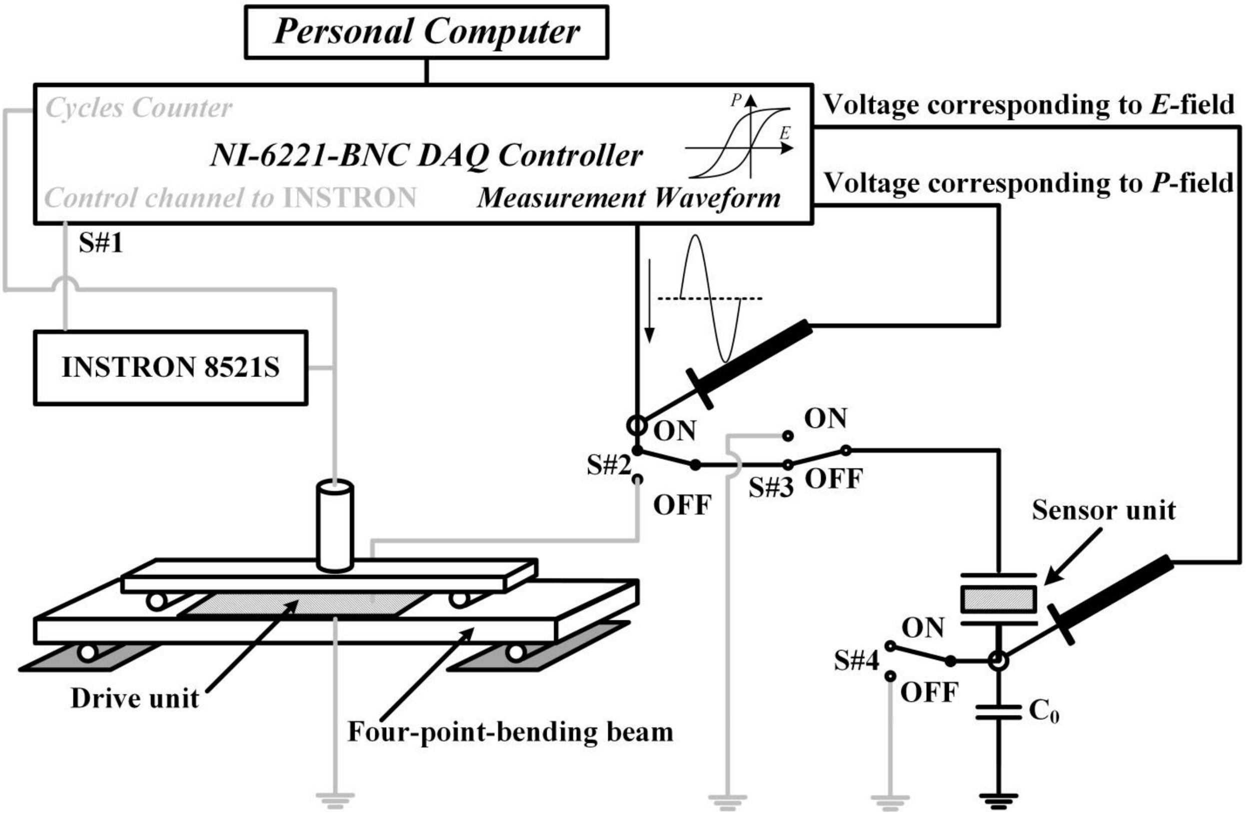

Figure 3-15 Measurement mode of the measurement system

3.6. Experimental Results

3.6.1. Polarization fatigue curve measurement

Figure 3-16 shows the hysteresis loops of PZT thin film with 2.0 μm in thickness and 0.5 mm in diameter under sinusoidally cyclic (1.0 Hz, 1~10000 cycles) electric field with 6.0 V in amplitude. The relation between corresponding remnant polarization P_r against number of cycles N taken from Figure 3-16 is shown in Figure 3-17. The polarization fatigue curve of Figure 3-17 shows three stages: (1) initial in plateau while low-cycle electric field is applied, (2) while the electric field is applied in middle number of cycles range, the remnant polarization drops rapidly, and (3) the remnant polarization remains nearly flat for the large number of cycles.

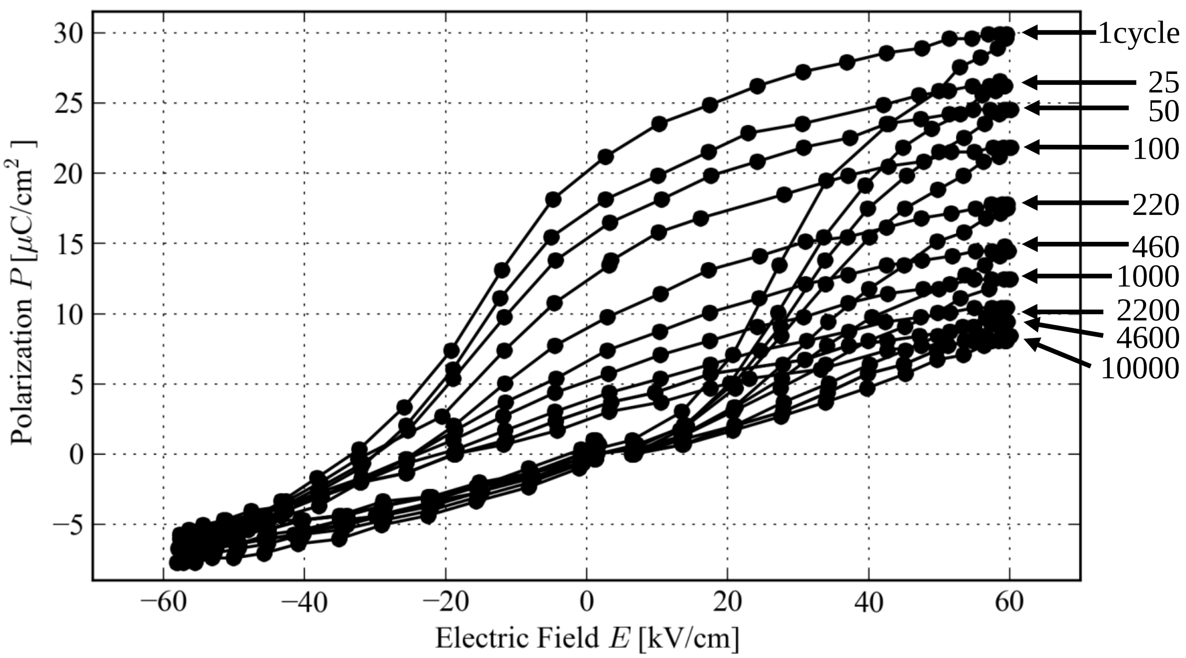

Figure 3-16 Hysteresis loops for a ferroelectric thin film (2.0 μm in thickness and 0.5 mm in diameter) from 1 to 10000 cycles

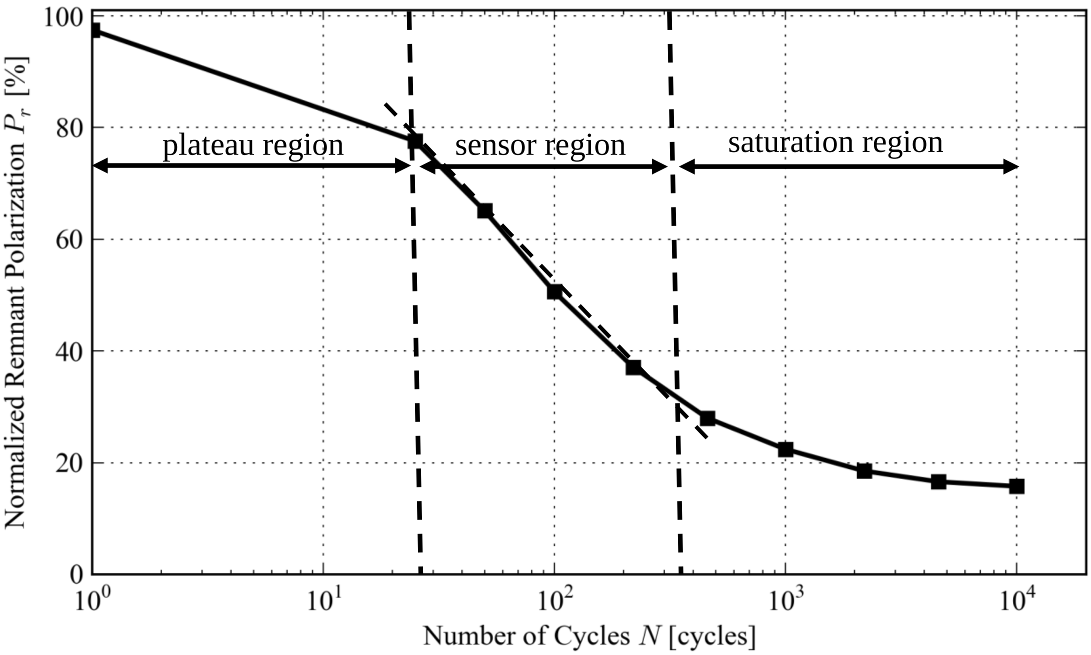

Figure 3-17 Normalized polarization fatigue curves of ferroelectric thin film (normalized by P_r = 20 μC/m^2 at N=1)

3.6.2. The effect of driving electric field

The effects of the driving electric field amplitude on polarization fatigue of PZT films are shown in Figure 3-18 and Figure 3-19. We applied cyclic displacement up to 10^6 to 10^7 cycles on the four-point-bending fixture and dynamically stressed the drive unit (piezoelectric patches). In order to simulate the voltage sending from drive unit excited by mechanical vibration, we applied a low frequency of 1.0 Hz on the four-point-bending fixture. Each test took at least 10 days to cause polarization fatigue on the PZT thin film. The piezoelectric patches on the structural component (drive unit) sending out $0.8V_{th}$ to $1.7V_{th}$ (Figure 3-18) and $0.6V_{th}$ to $4.5V_{th}$ (Figure 3-19) to PZT thin films (sensor unit) with the dimensions of 1.5 mm in diameter and 1.5 μm in thickness (the threshold electric field for this dimension is $E_{th} = 3.0$ V/ μm, i.e. $V_{th} = 3.0$ V/μm (E_{th}) ×1.5 μm (thickness of the PZT thin film) for the PZT films we tested). The experimental results shown in Figure 3-18 and Figure 3-19 illustrate that the applied electric field accelerates the polarization fatigue. In the sensor region, the slope of fatigue curves of different driving voltage is close in logarithmic scale. If the stress levels are lower than the threshold stress, which send out voltage lower than threshold voltage, the plateau remains much longer in number of cycles; however, if the stress levels are higher than the threshold stress, the fatigue curves step into sensor region much sooner. The polarization drops exponentially in the sensor region adopting linear scale for *x*-axis, the number of cycles. However, if logarithmic scale is used for the number of cycles, the sensitivity is close even if we apply different stress levels.

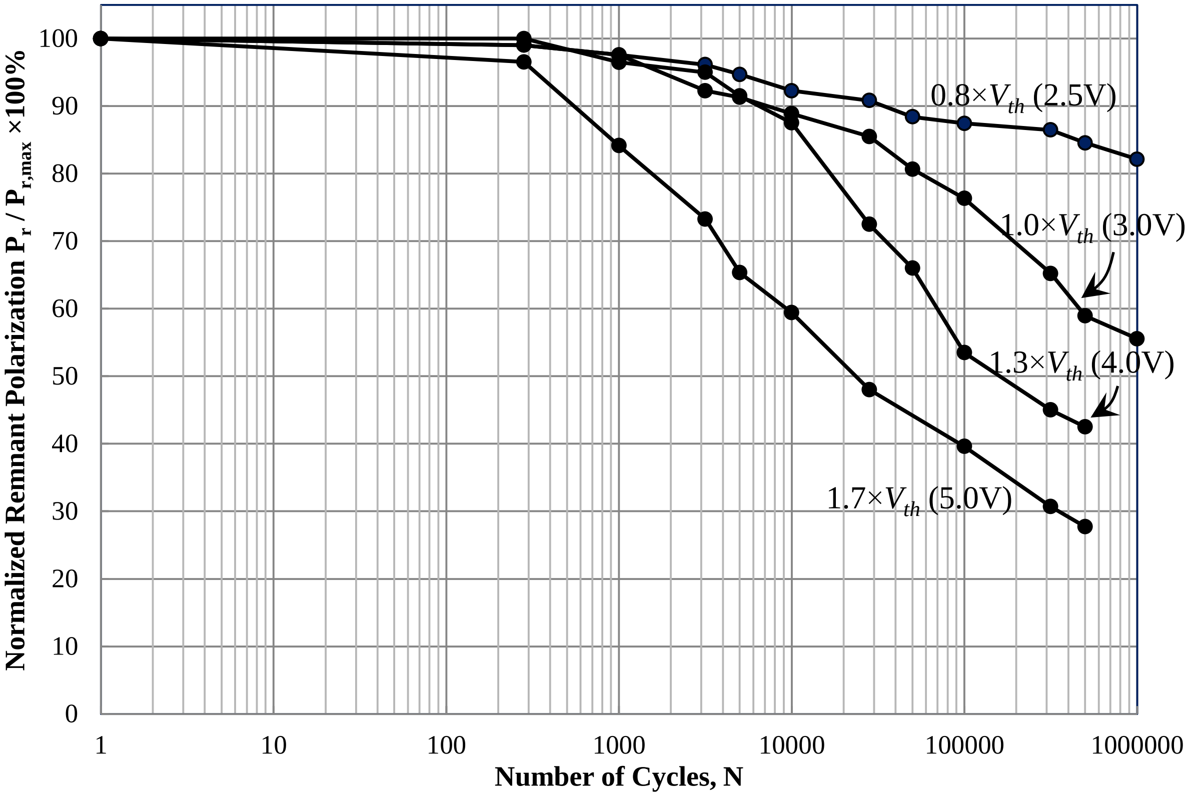

Figure 3-18 Fatigue behavior of various output voltage from drive unit (lower than domain-switched voltage)

Table 3-2 Sensitivity for a single daughter sensor PZT unit applied different voltage

	0.8V_{th}	1.0V_{th}	1.3V_{th}	1.7V_{th}
Plateau region (number of cycles)	1~	1~1000	1~400	1~200
Sensor region (number of cycles)	~	2000 ~	1000 ~	200 ~
Plateau sensitivity (linear scale in cycles)	-6.36×10^{-6}	-2.44×10^{-3}	-1.58×10^{-3}	-0.0085
Sensor sensitivity (linear scale in cycles)	×	-3.08×10^{-5}	-1.10×10^{-4}	-1.1×10^{-4}
Plateau sensitivity (log scale in cycles)	-8.70	-2.21	-1.43	-7.64
Sensor sensitivity (log scale in cycles)	×	-19.3	-23.86	-20.90

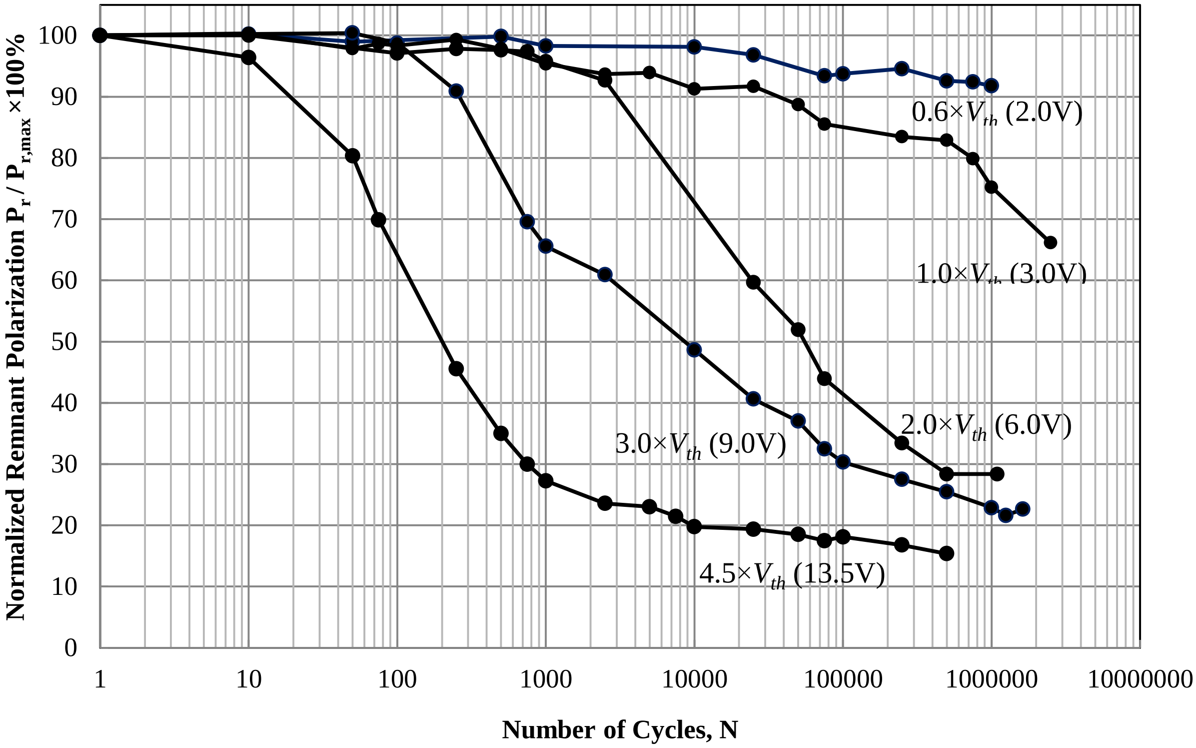

Figure 3-19 Fatigue behavior of various output voltage from drive mother PZT unit (high than domain-switched voltage). Apply on 1.5mm in diameter and 1.5μm in thickness sensor PZT unit.

The plateau and sensor region for each curve and its sensitivity is summarized in Table 3-3. The sensitivity of the sensor region represents exponential decrease when we use linear scale for the number of cycles. However, if we take the logarithmic scale for the number of cycles, the sensitivity is close even if we apply different stress levels.

Table 3-3 Sensitivity for a single daughter sensor PZT unit applied different voltage

	0.5V_{th}	**1.0V_{th}**	**1.5V_{th}**	**2.0V_{th}**	**3.0V_{th}**
Plateau region (number of cycles)	1~×	$1\sim5\times10^5$	$1\sim1\times10^3$	1~100	1~10
Sensor region (number of cycles)	×	500000 ~25000000	2500 ~500000	250 ~500000	50 ~1000
Plateau sensitivity (linear scale in cycles)	-1.48×10^5	-3.42×10^5	-0.0042	-0.017	-0.4
Sensor sensitivity (linear scale in cycles)	×	-8.11×10^{-6}	-1.2910^{-4}	-6.07×10^{-4}	-0.0698
Plateau sensitivity (log scale in cycles)	-1.30	-3.01	-1.41	-0.83	-3.60
Sensor sensitivity (log scale in cycles)	×	-23.21	-27.94	-23.27	-34.57

The polarization fatigue curves show that the driving voltage affects the speed of fatigue. To apply this material nature of polarization fatigue to the proposed SHM system, some designs are required to make a reliable and accurate SHM system.

In the practical applications, the vibration is random in its amplitude and induces random amplitudes of stress on the structural component and the drive unit of SHM system. The random amplitudes of stress on the drive unit sends out random amplitudes of voltage to the sensor unit. Different amplitudes of voltage fatigue the sensor unit to varying degrees, it would be impossible to trace back the number of cycles for a specific stress level on the structural component and the corresponding voltage from the drive unit of SHM system. To solve this issue, we propose an interface circuit that when a random amplitude signal is sent into the circuit, the circuit recognizes the absolute value of the amplitude only. Once the absolute value of the amplitude is larger than a certain threshold, it sends out the voltage to the sensor unit; otherwise, the output voltage is set to zero and sent to the sensor unit. Therefore, the sensor unit is only fatigued by a certain level of voltage induced by the corresponding stress level on the structural component.

The fatigue signal to the sensor unit is a voltage pulse train with an amplitude corresponding to a specific stress level on the structural component. Details will be explained in the next chapter.

3.7. Conclusion

In this chapter, we reviewed the literature about the polarization fatigue of ferroelectric thin film, and PZT thin film in particular. To the proposed SHM system, the amplitude, waveform, and frequency of driving electric field are critical issues. The reviewed literature shows that among all the parameters that researchers have studied, the effect of amplitude of the driving electric field shows inconsistency. Next, the mechanisms of the polarization fatigue were summarized and introduced next.

To clarify the effect of the driving electric field, we build up an automatic measurement system that are capable of conducting millions of cycles of applied electric fields and periodically measured the hysteresis loop and the corresponding remnant polarization at a specific number of cycle. The experimental results showed that the electric field accelerates the polarization fatigue. In the practical application of random amplitude of excitations, an interface circuit will be designed in the next chapter to develop a reliable SHM system.

Chapter 4 Proposed SHM System and its Performance

The behaviors of the drive and sensor units have been studied in Chapter 2 and 0, respectively. The idea of the proposed SHM system can be generalized in Figure 4-1 that the drive unit sends out dynamic voltage signal, which is a liner function of stress on the structural component. The voltage signals carrying the information of stress levels on the structural component is sent to the sensor unit, and voltage signal generated from the drive unit induces polarization fatigue to the ferroelectric material based sensor unit. The loss of the polarization determines the number of cycles of the electric field with a specific amplitude that carries the information (number of cycles and amplitude) of dynamic stress. The number of cycles of a specific stress level of dynamic loading on the structural component can be back calculated by the measurement of remnant polarization P_r.

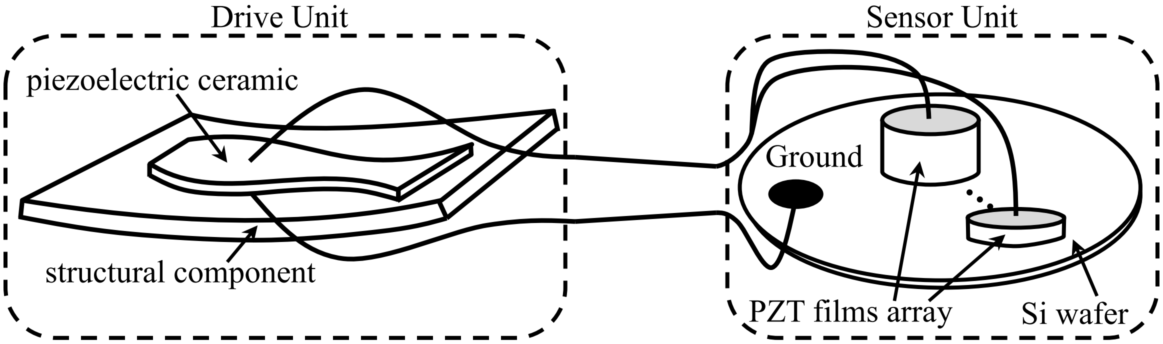

Figure 4-1 Proposed Structural Health Monitoring

However, some of the research [66][67][68][69][70][71][72] introduced in Sec.3.1 as well as the experimental results of polarization fatigue shown in Figure 3-18 and Figure 3-19 illustrate that the driving voltage (or electric field) accelerates the polarization fatigue of the PZT thin films. High voltage (or electric field) induces intensive polarization fatigue. Once we measure the loss of remnant polarization under multiple amplitudes of the dynamic loadings, both intense and mild polarization fatigue are involved to the loss of remnant polarization and makes it impossible to calculate the fatigue comes from one or several specific amplitudes of stress. To resolve this issue, a window comparator circuit is designed to eliminate the irrelevant amplitudes of voltage, only a specific level of voltage remains and sends to the sensor unit, which makes it possible to determine the polarization fatigue is induced by a specific level of stress on a structural component by how many number of cycles of that stress level.

In this chapter, we will introduce how the drive and sensor units, and in particular the interface circuit in between function in the proposed SHM system. To verify that the concept of the proposed SHM system works, we conducted several sets of experiments that the number of cycles of two specific stress amplitudes was counted by both a DAQ system with a LabVIEW program (exact number of cycles) as well as by the fatigue curve (measured number of cycles). We also show the errors between the exact and measured number of cycles.

4.1. Window Comparator

Since the polarization fatigue curves of piezoelectric thin film highly depend on the applied voltage induced by the amplitude of dynamic stress loading, we need a signal conditioner which functions as a comparator. If the amplitude of stress is larger than a certain value, named as threshold stress, the threshold voltage generated from the drive unit is sent out to the sensor unit, causing electrical domain switch; otherwise, the smaller amplitude of voltage from the drive unit that is sent to the sensor unit would not induce polarization fatigue to the sensor unit. An operational amplifier with proper connection was chosen to achieve this function.

The operational amplifier shown in Figure 4-2 is a typical differential amplifier: the output V_o linearly depends on the difference of the inverting and non-inverting input ($V_+ - V_-$) with voltage gain G as $V_{out} = G\,(V_+ - V_-)$.

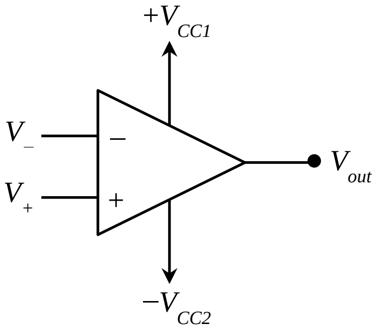

Figure 4-2 Voltage comparator (Operational amplifier)

The output voltage becomes positive when the non-inverting input becomes more positive than the inverting input, and vice versa. Since the voltage gain G is typically around $10^5 \sim 10^6$, a small voltage difference leads to a very high output. However, no matter how high the output voltage we have from the drive unit shown in Figure 2-11(a), the output voltage of operational amplifier never goes higher than the voltage $+V_{CC1}$ or lower than $-V_{CC2}$ provided by the power source. In other words, once a very small voltage difference is applied on the non-inverting and inverting nodes, the output voltage soon reaches the saturated voltage provided by external power source, a perfect comparator to judge if the signal is positive or negative. The behavior of the operational amplifier can be represented as follows

$$V_{out} = \begin{cases} +V_{CC1}, V_+ > V_- \\ -V_{CC2}, V_+ < V_- \end{cases} . \qquad (4\text{-}1)$$

Several window comparators modified by two diodes for each shown in Figure 4-3 is used for the interface circuit for SHM system.

If V_{in} is higher than V_{D1}, the diodes D_1 allow current to pass to the negative terminal, while the diodes D_2 block current to pass to the positive terminal, which makes $V_+ = V_{in}$ and $V_- = 0$ V. Eqn. (4-1) shows output voltage becomes $V_{out} = +V_{CC}$. Similarly, If V_{in} is lower than V_{D2}, the diodes D_2 allow current to pass to the negative terminal, while the diodes D_1 block current to pass to positive terminal, which makes $V_+ = 0$V and $V_- = V_{in}$. Eqn. (4-2) show that output voltage becomes $V_{out} = -V_{DD}$.

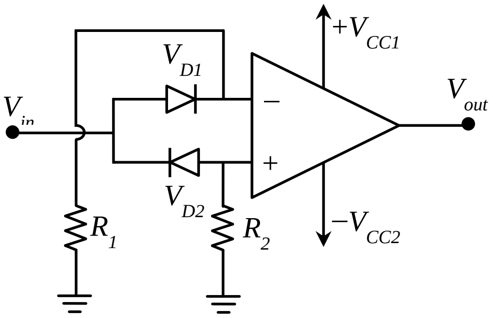

Figure 4-3 Window comparator (WC) for the interface circuit of SHM system

$$V_{out} = \begin{cases} +V_{CC}, V_{in} > V_{D1} \\ -V_{DD}, V_{in} < V_{D2} \end{cases}. \qquad (4\text{-}2)$$

Figure 4-4 shows the characteristic relationship (V_{in} vs V_{out}) of a window comparator. If the amplitude of the input voltage to the window comparator is larger than the threshold voltages of the diodes, the output voltage are set to V_{cc} or $-V_{DD}$; otherwise, the output voltage is zero. Apply this electric characteristic to the output of the drive unit, the window comparator is able to activate the polarization fatigue while the stress on the structural component reaches to a certain value (threshold stress). If the stress on the structural component is mild, below to the threshold stress, the polarization fatigue is deactivated by the window comparator.

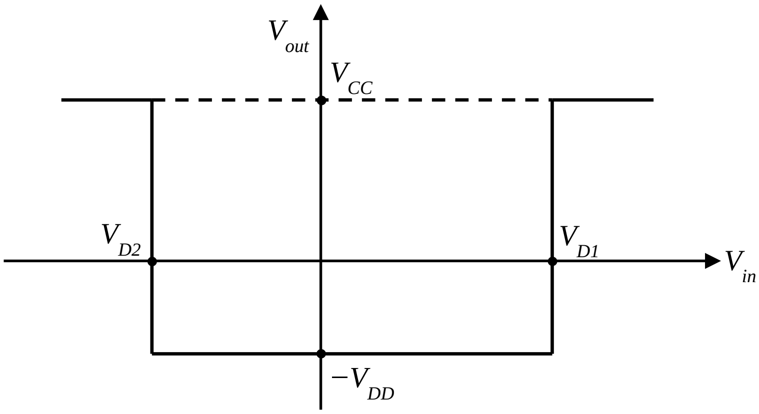

Figure 4-4 Characteristic curves for a window comparator

Table 4-1 generalized two window comparators that we will use in the following experiments. The window comparators have two different supplied voltages (V_{CC1} and V_{CC2}) and two different pairs of diodes for different threshold voltages (V_{D1} and V_{D2}), which is able to activate two levels of polarization fatigue (by V_{CC1} and V_{CC2}) if the voltage sent into the window comparators reaches two levels of threshold voltage (V_{D1} and V_{D2}). The characteristic curves for the pair of the window comparator are illustrated in Figure 4-5.

In the time period of a loading history from 0 second to 10 second, for the example, WC1 senses five peaks shown in the above figure of Figure 4-6, which means the SHM system counts the structural component undergone five times of stress, which amplitude over 12.6 MPa in this time block, and WC2 senses eleven peaks in the signals from drive unit, shown in the below figure of Figure 4-6, which corresponds to the stress on the structural component reaches eleven times over 7.88 MPa in the time block.

Table 4-1 Specifications of a pair of window comparators

	WC1	WC2
$+V_{CC}$	8V	5V
$-V_{DD}$	0V	0V
V_{D1}	8V	-8V
V_{D2}	5V	-5V

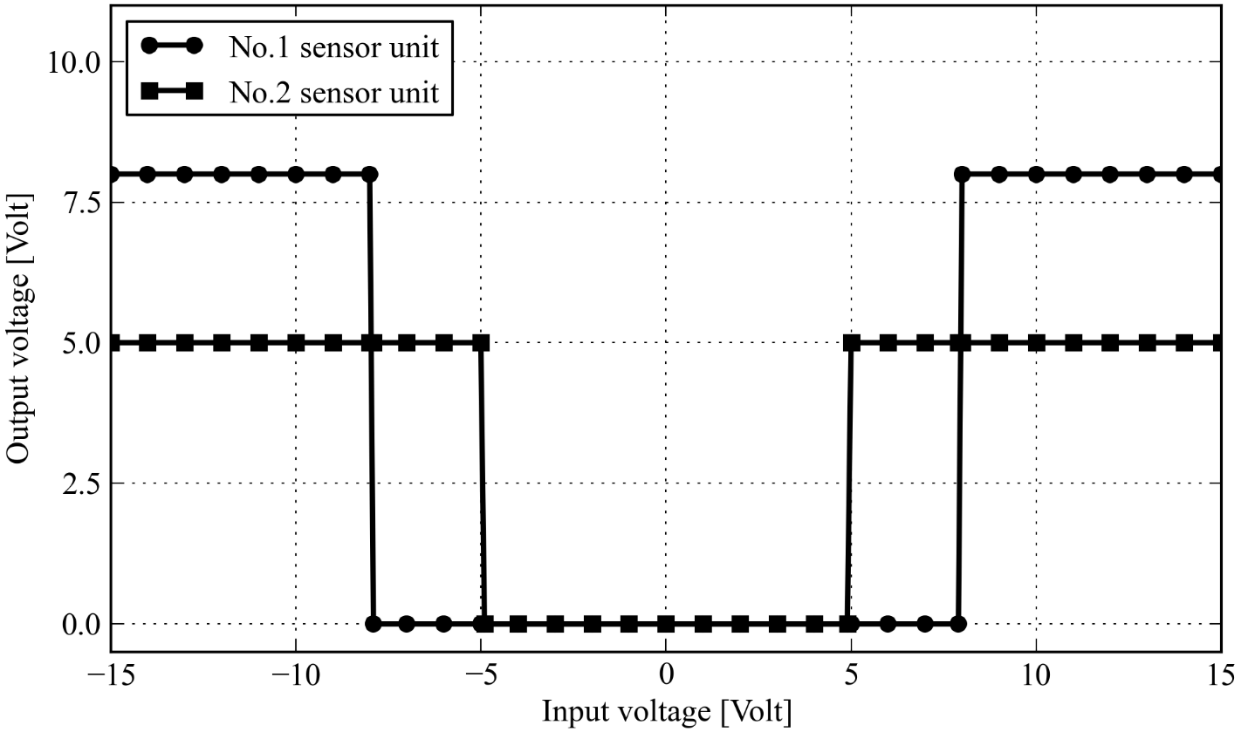

Figure 4-5 Output and Input voltage curves for window comparator

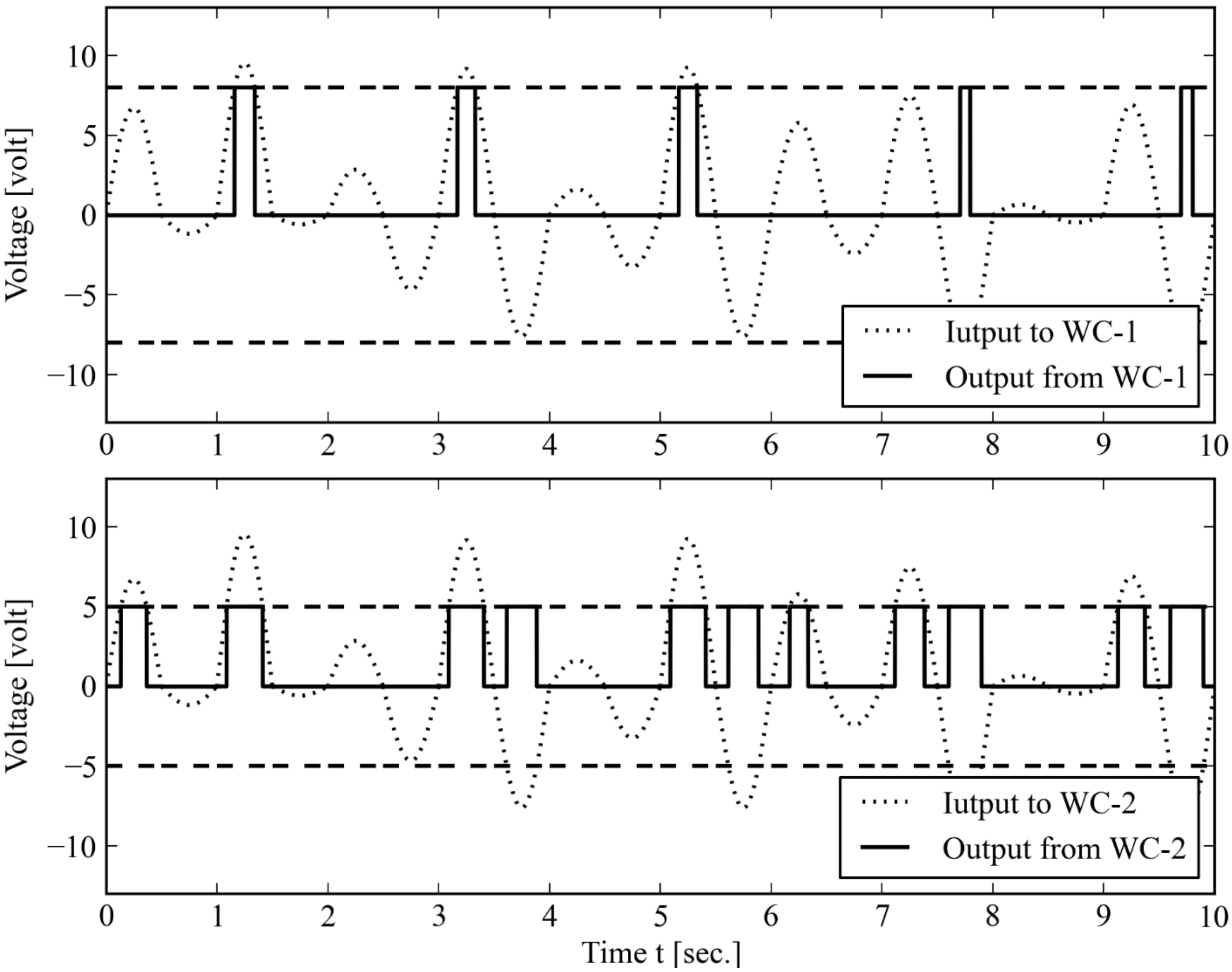

Figure 4-6 Time-domain performance of window comparators;
above figure: input and output voltage of window comparator 1 (WC-1),
and below figure: input and output voltage of wind comparator 2 (WC-2).

4.2. Verifications of the Proposed SHM System

To verify the performance of the proposed SHM system, a SHM system with one drive unit (three pieces of 1.0 cm×5.0 cm PZT C-6 piezoelectric ceramic from Fuji Ceramic), two sensor units (PZT thin films – No.1: 5.0 μm in thickness, 1.5 mm in diameter, No.2: 2.7 μm in thickness, 1.5 mm in diameter) and interface circuit is designed to evaluate the performance to estimate the number of cycles of two specific stress levels on a structural component. To this end, a dynamic four-point-bending test is used to drive the beam and the mounted piezoelectric patches sinusoidally in 1.0 Hz frequency, where the stress levels ranges from -20 to +20 MPa dynamically, uniformally distributed on the top-most surface of the beam in spatial domain. The signal from the drive unit is conditioned by the interface circuits and sent out pulse trains with corresponding threshold amplitude to the corresponding sensor unit. The interface circuits send out 5 V and 8 V to electrically fatigue No.1 and No.2 sensor unit, respectively.

The proof-of concept experiment is conducted in the following two steps: 1. retrieve the polarization fatigue curve of each PZT thin film (sensor unit), and 2.employ random amplitude excitations to the drive unit. Details and results are discussed in the following sections.

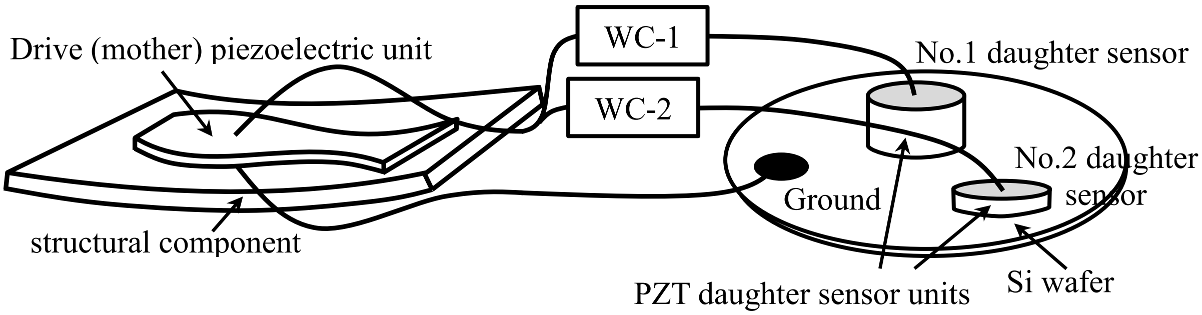

Figure 4-7 Modified SHM system with two window comparators

Step1: Unipolar polarization fatigue test to each PZT thin film of sensor unit

As discussed previously, considering the effect of driving electric field to the polarization fatigue of PZT thin film, we applied the signal with information of stress on the structural component to a window comparator. The signal going out from the window comparator becomes a specific amplitude of pulse train, representing a specific stress level, and electrically fatigue each PZT thin film. Therefore, for the modified design of the SHM system, applying unipolar fatigue waves would be more suitable than the typical approach, which is applying bipolar fatigue waves. To retrieve the polarization fatigue information for the modified SHM system with window comparators, we apply a pulse train to polarization fatigue the PZT thin film. The experiment setup is shown in Figure 3-8 and Figure 3-9, controlled by NI-LabVIEW and DAQ system following Figure 3-10 and Table 3-1. The waveforms that we apply to the PZT thin film in each mode are modified from Figure 3-11 to Figure 4-8. Note that the fatigue waveforms in Figure 3-11 have been modified from bipolar sinusoidal waves to unipolar pulse trains in Figure 4-8.

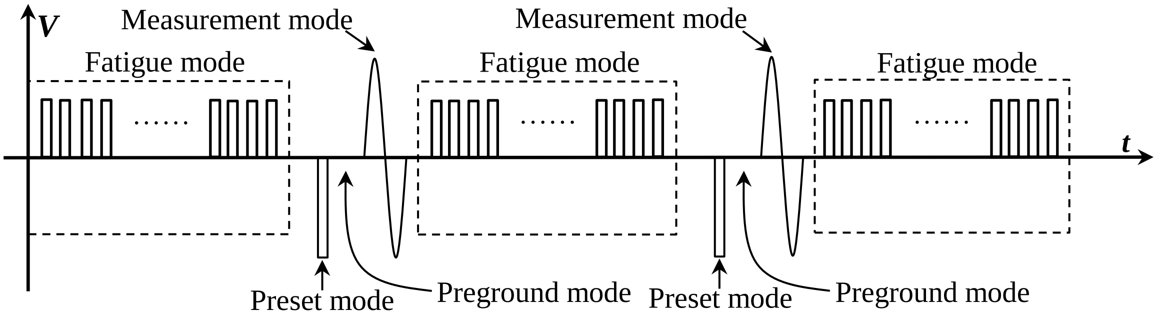

Figure 4-8 Sequence of polarization fatigue curve measurement

Figure 4-9 shows the result of polarization fatigue tests for No.1 and No.2 sensor units under unipolar cyclic voltage of 0 ~ 8.0 V and 0 ~ 5.0 V to match the input voltage from window comparators WC1 and WC2, respectively, to sensor units. A 15-number-of-cycles voltage 8 V and 5 V have been pre-trained for No.1 and No.2 sensor units, respectively, to make sure the as-pretrained sensor system passes through the first region of P_r - N curve of Figure 4-9 and functions linearly in a wide range of sensing area in logarithmic scale. The P_r – N relation of these two sensor units that are obtained experimentally (see Figure 4-9) can be expressed linearly as follows

$$\begin{Bmatrix} P_{r1}(\%) \\ P_{r2}(\%) \end{Bmatrix} = \begin{bmatrix} -12.2\,(\%/\text{cycle}) & 0 \\ 0 & -29.5\,(\%/\text{cycle}) \end{bmatrix} \begin{Bmatrix} \log N_1\,(\text{cycle}) \\ \log N_2\,(\text{cycle}) \end{Bmatrix} + \begin{Bmatrix} 98.4\% \\ 90.4\% \end{Bmatrix}. \qquad (4\text{-}3)$$

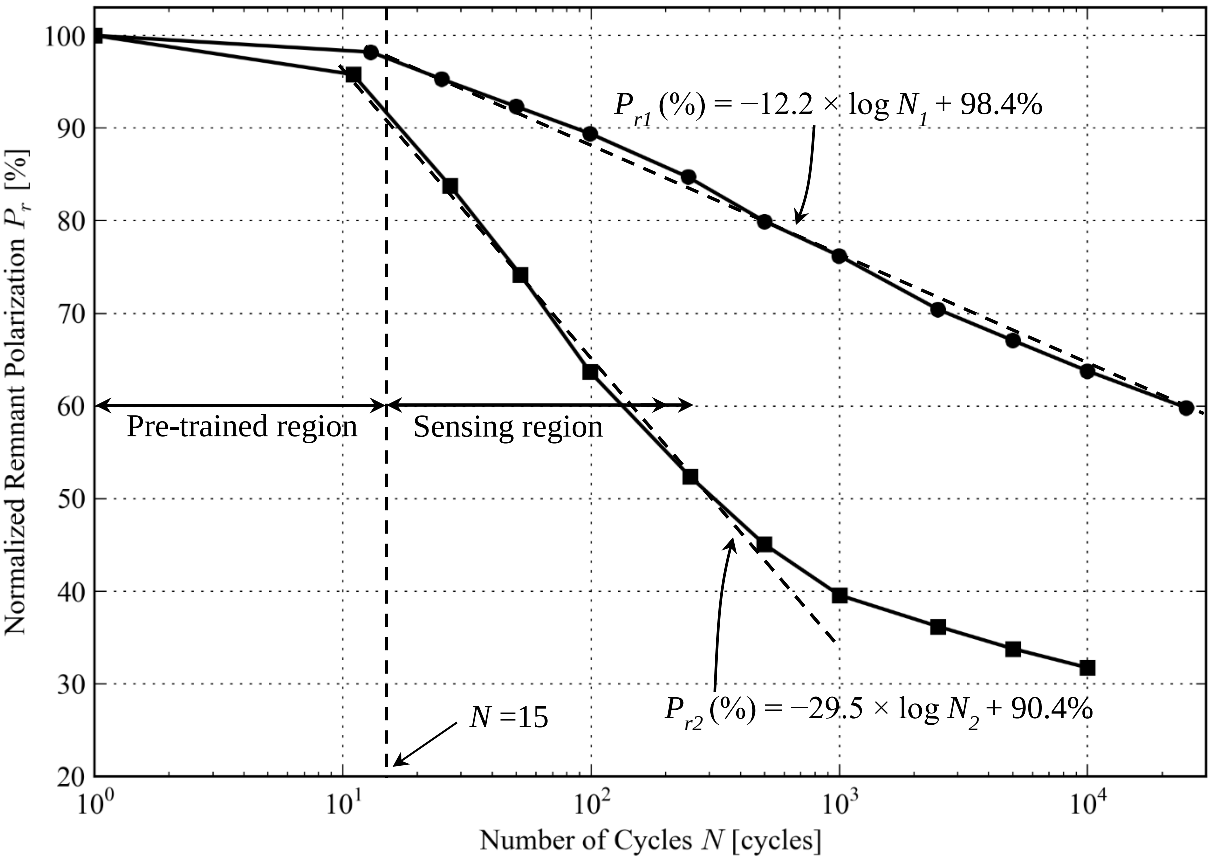

Figure 4-9 Polarization fatigue curve of piezoelectric thin film for No.1 (5.0 µm in thickness and 1.5 mm in diameter under cyclic voltage 8 V) and No.2 (2.7µm in thickness and 1.5 mm in diameter under cyclic voltage 5 V) sensor units

Step2: Verification of proposed SHM system with excitation of random amplitudes

To verify the performance of the proposed SHM system, we applied random amplitudes of sinusoidal displacement with 1.0 Hz in frequency to the four-point-bending fixture by a universal testing machine INSTRON 8521S shown in Figure 3-8 and Figure 3-9. The excitations applied to the four-point-bending fixture induced a random amplitudes of sinusoidal stress, ranging from -20 MPa to 20 MPa, in time domain. The random amplitudes of voltage from the drive unit is sent to window comparator and signals that the PZT thin films receiving from the window comparator are pulse trains with amplitude of 8.0 V for No.1 sensor unit and 5.0 V for No.2

sensor unit. Figure 4-6 is an example of how window comparators receive random amplitude voltage from drive unit and send out pulse trains to sensor units. The tests were randomly stopped and measured the remnant polarization by the measurement system shown in Figure 3-8 and Figure 3-9. The number of cycles of the stress on the structural component whose amplitude of stress reaches a certain value can be back calculated by the measured remnant polarization following Eqn.(4-3). By comparing this calculated number of cycles to that directly counting the excitations that INSTRON 8521S made, we could verify the accuracy of the proposed SHM system.

The Case 1 in Table 4-2 shows the counted number of cycles of the load history above 12.60MPa and 7.88MPa on the topmost surface of the four-point-bending beam by sensors No.1 and No.2, which are considered to be exact results. The Case 2 in Table 4-2 shows by using curve fitting (dash lines in Figure 4-9) for the standard polarization fatigue test for both No.1 and No.2 sensor units, we estimate number of cycles for both stress levels by measuring the remnant polarization under a specific number of cycles, which are considered to be predictive results. The Third group in Table 4-2 shows the error between exact results and predictive results of the SHM system. In general, the performance of the SHM system shows acceptable estimation of number of cycles counting. The error is ranging from 1.0 to 19.7%, and the average error is less than 10% in general.

Table 4-2 Experimental results for exact number of cycles counted from the load history and estimated number of cycles from proposed SHM system for two cases; case 1: real counted numbers; case 2: counted numbers from linearly idealized curve

Case 1: Number of cycles by counting load history								
Sensor unit No.1 (12.6 MPa)	12	22	57	165	231	361	685	733
Sensor unit No.2 (7.88 MPa)	79	150	291	452	524	644	1658	2673
Case2: Number of cycles by curve fitting (Linear equation to fit the fatigue curves)								
Sensor unit No.1 (12.6 MPa)	14	24	53	178	213	403	735	678
Sensor unit No.2 (7.88 MPa)	77	138	294	506	490	771	1935	2214
Errors between cycle counting and curve fitting (%)								
Sensor unit No.1 (12.6 MPa)	16.7	9.1	7.0	7.9	7.8	11.6	7.3	7.5
Sensor unit No.2 (7.88 MPa)	2.9	7.8	1.0	11.2	6.4	19.7	16.7	17.2

4.3. Conclusion

To overcome that the driving electric field affects the polarization fatigue, we proposed to put a comparator circuit that is capable of reading a specific value of voltage from the drive unit corresponding to a stress level on the structural component that is equal to or larger than a certain value. The measurement system was modified to electrically fatigue the sensor unit in pulse trains rather than sinusoidal waves to match the waveforms that the modified SHM system sends to the sensor unit. The performance of the proposed SHM system was demonstrated by a two-sensor-unit SHM system and the verification tests show that the error is ranging from 1.0 to 19.7%, and the average error is less than 10% in general.

Chapter 5 Load Transfer Design

In most of the practical applications, the stresses on the structure are significantly larger than the fracture stress of typical piezoelectric ceramics and (for example, 90 MPa in the case of PZT-C6) and may induce fracture on the ceramic-based drive unit. To protect the fragile drive unit from fracturing under high external stress, a load transfer module where a driver unit is mounted to the structure surface by a thin viscous layer is proposed. The configuration of the load transfer design is shown in Figure 5-1. The high stress / strain in the structural component is relaxed by flow in the viscous layer which progress in a diffusive manner from the edges of the PZT layer inward toward its center. The external loadings applied on the structural components can be generalized into two types: tension/compression and bending modes, which will be discussed in this chapter.

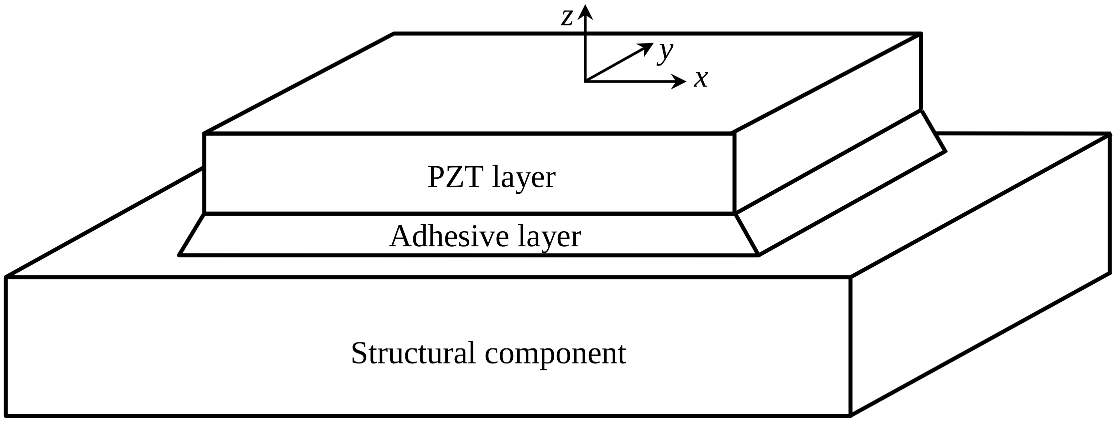

Figure 5-1 Schematic diagram of a PZT layer bounded to a thin viscous slayer which is bounded to a structural component

5.1 Literature Review

The research similar to load transfer design in configuration comes from two different fields of studies: thin film mechanics and lap joint mechanics. Thin film mechanics is to study the mechanical behaviors of layers of thin films deposited on a substrate, which involve the fracture, peeling, fatigue, etc. under external loading and particular under thermal loading. The mechanical analyses of lap joints or adhesive joints are to study stress distributions and suitable fracture criterion to predict stress distribution and a suitable fracture criterion for designers. Both fields of research benefit the study of proposed load transfer design.

The idea of the load transfer design for SHM system comes from the configuration of thin film bonded on a relative thick substrate. The internal stress of the thin films induced by external loading or thermal effect can cause variety types of consequence, including fracture, delamination or peeling. These mechanical behaviors in thin films are studied specifically in thin film mechanics [87].

The study of thin film mechanics originated from Stoney [88], who made observations that a copper film deposited on a substrate was in tension or compression without loads applied to the system, and the internal tension and compression would strain the substrate and induce bending. He also formulated the relationship between the stress in the film and the amount of bending moment in the substrate.

The theoretical descriptions based on stress transfer analysis were first presented by Cox, who applied shear lag model on fiber-reinforced materials [89]. To take consideration of residual strains and initial crack in the two-layer composite, a modified shear lag model was then proposed theoretically and verified experimental [90].

The elastic behavior of a multi-layer thin film on a thick substrate was presented by Townsend and Barnett in 1987. Under the approximations for the case of thin films on a substrate, the governing equations for stresses in multilayered thin-film structure was discussed and the resultant internal and residual stress induced by fabrication process affects the mechanical behavior of the thin-film-substrate structure was studied theoretically and experimentally [91].

The elastic solution of a tri-layer structure with finite dimensions is presented by Wang *et al* [92]. More types of interfacial stresses: shear, peeling, bending, and die cracking stress are studied and result to a governing equation with seventh order differential equation. The analytical expression of each type of stress is also presented.

The literature review shows that due to the application of thin film technology, most of the research assumes that thickness is relative much smaller than length and width of the structure; therefore, infinite length is the fundamental assumption for most of the research. The temperature effect during the fabrication process is also a critical issue in thin-film technology.

As for the lap joints, which can be classified into single and double-lap joints in general shown in Figure 5-2, there have been numerous of models for the adhesive joint been developed since Volkersen [93] and Goland and Reissner [94] presented their analyses on lap joints with flat adherends. Both work laid foundations to the analyses of the lap joint. Volkersen [95] analyzed a single-lap joint case, assuming that the adhesive deforms only in shear, while the adherends deform in tension; both adhesive and adherends behave linear elastically. Since the asymmetric configuration of the lap-joint, applying the force on upper and lower laps may induce bending moment to the adhesive and adherends, the assumption is not practical for sing-lap joints. Based on Volkersen’s work Goland and Reissner [96] consider the bending moment on adherends while force applied to the single-lap joint . By studied tabular joints, Lubkin and Reissner [97], Adams and Peppiatt [98], and Nemes [99] et al. presented their two-dimensional linear elastic analyses, two-dimensional elasto-plastic analyses, three dimensional analyses. The limitations due to the assumptions that Volkersen [95] and Goland and Reissner [96] made was extended by Ojalvo and Eidinoff [100] and Tsai [101]. Ojalvo and Eidinoff [102] Tsai [103] used a more complete shear strain and displacement equations to model the shear and normal deformations of adherend layers, which studied the effect of adherent thickness on the stress distribution. Tsai [103] also used Moiré to investigated the deformation of the adherends and concluded that the proposed model made better approximation than previous researchers did.

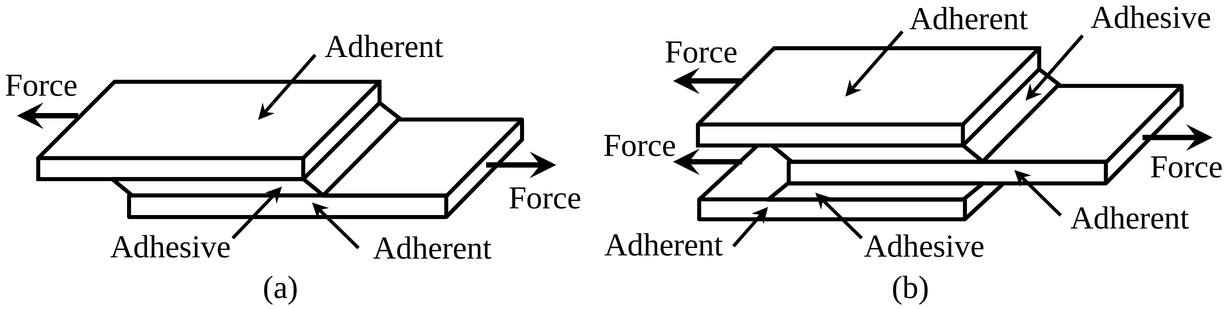

Figure 5-2 Adhesive joints: (a) single-lap joint, and (b) double-lap joint

The viscoelastic analysis of the lap joints was first conducted by finite element method by Nagaraja and Alwar [104] and then the closed-form solution was developed by Delale and Erdogan [105] after the finite element method was published. Nagaraja and Alwar [104] used Prony's series fitting for the viscoelastic material properties of the adhesive joints, and employed finite element analysis to analyze the single-lap joint subjected to tensile loading. Delale and Erdogan [105] formulated the problem of lap-joint considering elastic adherends and viscoelastic adhesives subjected to membrane, bending and shear and transverse shear loading, and solved the problems by standard Laplace transform.

To analyze the proposed load transfer design, we formulate static and dynamic closed-form solutions of both elastic and viscoelastic adhesive in various thickness. The closed-form solutions are verified by finite element software ANSYS.

5.2 Summary of Linear Elasticity

The Kirchhoff theory extends Euler-Bernoulli beam theory from slender beams to tin plates. Assuming that the Kirchhoff deformation hypothesis, plane remains plane assumption, is valid, the displacement field, u, v, and w along the x-, y-, and z- axes are given by

$$\begin{aligned} u &= u^0(x,y) - z\frac{\partial w}{\partial x} \\ v &= v^0(x,y) - z\frac{\partial w}{\partial y} \\ w &= w^0(x,y) = w(x,y) \end{aligned} \tag{5-1}$$

The two-dimensional strain components are obtained from Eq.(5-1) as

$$\begin{aligned} \varepsilon_x &= \frac{\partial u}{\partial x} = \varepsilon_x^0 + z\kappa_x \\ \varepsilon_y &= \frac{\partial u}{\partial y} = \varepsilon_y^0 + z\kappa_y \\ \gamma_{xy} &= 2\varepsilon_{xy} = \gamma_{xy}^0 + 2z\kappa_{xy}\,. \end{aligned} \tag{5-2}$$

where κ_x, κ_y, and κ_{xy} are curvatures defined as

$$\begin{aligned} \kappa_x &= -\frac{\partial^2 w}{\partial x^2} \\ \kappa_y &= -\frac{\partial^2 w}{\partial y^2} \\ \kappa_{xy} &= -\frac{\partial^2 w}{\partial x \partial y}\,. \end{aligned} \tag{5-3}$$

The constitutive equation for the laminate can be written as the in-plane stress-strain relation given by

$$\begin{Bmatrix} \sigma_x \\ \sigma_y \\ \sigma_{xy} \end{Bmatrix} = \begin{bmatrix} C_{11} & C_{12} & 0 \\ C_{21} & C_{22} & 0 \\ 0 & 0 & C_{66} \end{bmatrix} \begin{Bmatrix} \varepsilon_x^0 + z\kappa_x \\ \varepsilon_y^0 + z\kappa_y \\ \gamma_{xy}^0 + 2z\kappa_{xy} \end{Bmatrix} \tag{5-4}$$

The resultant in-plane forces, N_x, N_y, and N_{xy} can be obtained from

$$\begin{Bmatrix} N_x \\ N_y \\ N_{xy} \end{Bmatrix} = \sum_{i=1}^{n} \int_{h_{i-1}}^{h_i} \begin{Bmatrix} \sigma_x \\ \sigma_y \\ \sigma_{xy} \end{Bmatrix} dz\,, \tag{5-5}$$

where h_{i-1} and h_i are z coordinate of bottom and top surface of i^{th} lamina, and n is number of layers of the laminate.

The resultant bending moments, M_x, M_y, and M_{xy} can be obtained from

$$\begin{Bmatrix} M_x \\ M_y \\ M_{xy} \end{Bmatrix} = \sum_{i=1}^{n} \int_{h_{i-1}}^{h_i} z \begin{Bmatrix} \sigma_x \\ \sigma_y \\ \sigma_{xy} \end{Bmatrix} dz\,, \tag{5-6}$$

5.3 Theory of Linear Viscoelasticity

5.3.1 Mechanical Models

The most fundamental models to describe viscoelastic materials are Maxwell and Kelvin model. The Maxwell model can be represented by a viscous damper and elastic spring connected in series, which is suitable to describe relaxation of viscoelastic materials shown in Figure 5-4(a), which gives the following equation for viscoelastic behavior:

$$\frac{d\varepsilon}{dt} = \frac{1}{E}\frac{d\sigma}{dt} + \frac{\sigma}{\eta} \tag{5-7}$$

On the other hand, the Kelvin model consists of a viscous damper and elastic spring connected in parallel shown in Figure 5-4(b), is used to explain creep behavior of viscoelastic materials, which gives the following equation of viscoelastic behavior:

$$\sigma = E\varepsilon + \eta \frac{d\varepsilon}{dt} \tag{5-8}$$

To model both relaxation and creep behaviors of materials, more sophisticated models, generalized Maxwell and Kelvin, are developed to better describe the viscoelastic materials. The generalized Maxwell model shown in Figure 5-6, arranged each single unit of Maxwell model in a parallel fashion, is more popular and will be mainly used in this chapter. Similarly, the generalized Kelvin model, arranged every single unit of Kelvin model in series.

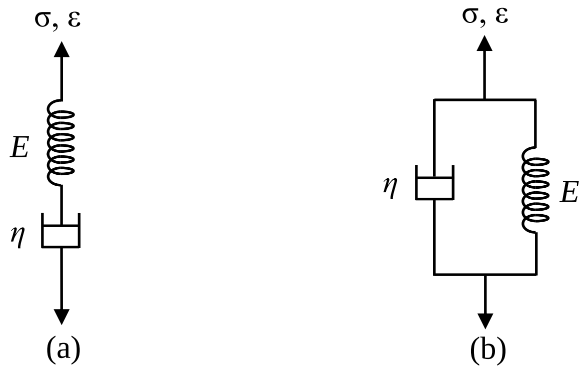

Figure 5-3 Schematic diagram of (a) Maxwell and (b) Kelvin models

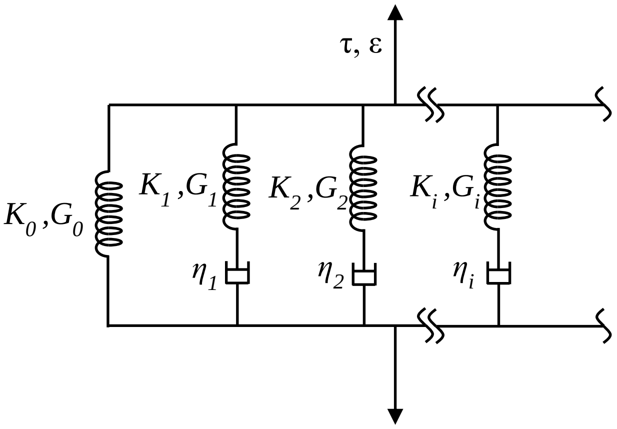

Figure 5-4 Schematic diagram Generalized Maxwell model

The relaxation modulus for the generalized Maxwell model is

$$K(t) = K_\infty + \sum_{i=1}^{n} K_i \exp\left(-\frac{t}{\lambda_i}\right) \; ; \; \lambda_i = \frac{\eta_i}{K_i} \tag{5-9}$$

$$G(t) = G_\infty + \sum_{i=1}^{n} G_i \exp\left(-\frac{t}{\lambda_i}\right) \; ; \; \lambda_i = \frac{\eta_i}{G_i}\,, \tag{5-10}$$

where $K(t)$ denotes the volumetric relaxation modulus, K_∞ denotes equivalent volumetric modulus, K_i denotes the volumetric modulus of the i^{th} element; $G(t)$ denotes shear relaxation modulus, G_∞ denotes equivalent shear modulus, G_i denotes the shear modulus of the i^{th} element; n notes the number of Maxwell models, t denotes reduced time, λ_i and is the relaxation time of i^{th} Maxwell element.

The generalized Maxwell model consider the contributions of stress in exponential function with different relaxation time, which provides a good fit to experimental nature of creep phenomenon if enough terms are used.

5.3.2 Constitutive Equations

The three dimensional Hooke's law of linear elasticity is given by

$$\sigma_{ij} = C_{ijkl}\varepsilon_{kl} \tag{5-11}$$

where C_{ijkl} as the elastic modulus tensor, and the summation convention assumed in which repeated indices are summed over.

For isotropic elastic materials, the constitutive equation is

$$\sigma_{ij} = \lambda(t)\varepsilon_{kk}\delta_{ij} + 2\mu\varepsilon_{ij} \tag{5-12}$$

The elastic tensor can then be expressed as

$$C_{ijkl} = \lambda\delta_{ij}\delta_{kl} + \mu(\delta_{ik}\delta_{jl} + \delta_{il}\delta_{jk}) \ . \tag{5-13}$$

as which λ and μ are two independent Lamé elastic constants.

For constitutive equation of viscoelastic materials, the Boltzmann superposition principle states that the effect of compound strain is the linear combination of the effects of each individual strain. Summing each stress increment due to the strain pulse in time domain, from the Boltzmann superposition principle, the stress and strain relation can be generalized into the form of integral representation. The time-dependent response of stress $\sigma_{ij}(t)$ and strain $\varepsilon_{kl}(t)$ is characterized by the constitutive equation as

$$\sigma_{ij}(x,t) = \int_{0^-}^{\xi} R_{ijkl}(t-t')\frac{\partial\varepsilon_{kl}(t')}{\partial t'}dt \tag{5-14}$$

The above integrals are evaluated for current time *t* based on past time *t'*, where R_{ijkl} is relaxation modulus.

Consider the case of isotropic materials, time-dependent relaxation modulus can be represented by Lamé constants as

$$R_{ijkl}(t) = \lambda(t)\delta_{ij}\delta_{kl} + \mu(t)(\delta_{ik}\delta_{jl} + \delta_{il}\delta_{jk}) \ . \tag{5-15}$$

Rearrange Eq.(5-15), the relaxation modulus R_{jikl} can be rewritten to separate volumetric and deviatoric behavior of viscoelastic materials as

$$R_{ijkl}(t)=\frac{1}{3}[3K(t)-2G(t)]\delta_{ij}\delta_{kl}+G(t)(\delta_{ik}\delta_{jl}+\delta_{il}\delta_{jk})\,. \tag{5-16}$$

where $K(t)$ is time-dependent bulk modulus, which characterizes volumetric response and $G(t)$ is time-dependent shear modulus, which reflects the deviatoric behavior.

Substitute Eqn.(5-16) into Eqn.(5-14), the constitutive equation of the viscoelastic behaviors becomes

$$\begin{aligned}\sigma_{ij}(x,t)&=\int_{0^-}^{t}\frac{1}{3}[3K(t-t')-2G(t-t')]\frac{\partial\varepsilon_{kk}(t')}{\partial t'}dt'\delta_{ij}+\int_{0^-}^{t}2G(t-t')\frac{\partial\varepsilon_{ij}(t')}{\partial t'}dt'\\&=\int_{0^-}^{t}K(t-t')\frac{\partial\varepsilon_{kk}(t')}{\partial t'}dt'\delta_{ij}+\int_{0^-}^{t}2G(t-t')\frac{\partial(\varepsilon_{ij}-\frac{1}{3}\varepsilon_{kk}\delta_{ij})(t')}{\partial t'}dt'\end{aligned}\,. \tag{5-17}$$

Eqn.(5-17) can be expressed by tensor notation as follows

$$\sigma_{ij}(x,t)==\int_{0^-}^{t}K(t-t')\frac{\partial\varepsilon_{kk}(t')}{\partial t'}dt'\delta_{ij}+\int_{0^-}^{t}2G(t-t')\frac{\partial\varepsilon_{ij}(t')}{\partial t'}dt'\,. \tag{5-18}$$

where $\varepsilon_{kk}\delta_{ij}$ is scalar volumetric strain times identity matrix and ε_{ij} is deviatoric strain tensor.

Eqn.(5-18) can be further simplified as follows

$$\sigma(x,t)=\int_{0^-}^{t}K(t-t')\frac{\partial\varepsilon_{V}(t')}{\partial t'}dt'+\int_{0^-}^{t}2G(t-t')\frac{\partial\varepsilon_{d}(t')}{\partial t'}dt'\,. \tag{5-19}$$

where ε_V is the scalar volumetric strain times identity matrix and ε_d is the deviatoric strain tensor as we mentioned in Eqn.(5-18).

The constitutive equation can be rewritten from Eqn.(5-19) as

$$\sigma(x,t)=\int_{0^-}^{t}K(t-t')\frac{\partial\varepsilon_V(t')}{\partial t'}dt'+\int_{0^-}^{t}G(t-t')\frac{\partial\gamma(t')}{\partial t'}dt' \ . \tag{5-20}$$

where $\gamma(t)$ is the shear strain. Eqn.(5-20) depict that the mechanical behavior of viscoelastic materials can be characterize as the first term, volumetric response by bulk modulus $K(t')$, as well as the second term, deviatoric response by shear modulus $G(t')$.

Considering volumetric and deviatoric response separately, the constitutive equations are shown as follows

$$\sigma(x,t)=\int_{0^-}^{t}K(t-t')\frac{\partial\varepsilon_V(t')}{\partial t'}dt' \tag{5-21}$$

$$\tau(x,t)=\int_{0^-}^{t}G(t-t')\frac{\partial\gamma(t')}{\partial t'}dt' \ . \tag{5-22}$$

For many practical applications of viscoelastic materials, deviatoric response dominates and is the only concern. Eqn.(5-20) is a good approximation for viscoelastic materials.

Applying generalized Maxwell model shown in Figure 5-4 to describe viscoelastic behavior of materials, the relaxation moduli $K(t)$ and $G(t)$ given in Eqn.(5-9) and Eqn.(5-10) can be modified to another form as Prony's series shown below

$$K(t)=K_0\left[\alpha_\infty^K+\sum_{i=1}^{n_K}\alpha_i^K\exp\left(-\frac{t}{\tau_i^K}\right)\right] \tag{5-23}$$

$$G(t)=G_0\left[\alpha_\infty^G+\sum_{i=1}^{n_G}\alpha_i^G\exp\left(-\frac{t}{\tau_i^G}\right)\right] \tag{5-24}$$

where K_0 and G_0 are bulk and shear relaxation moduli at $t = 0$, n_K and n_G are number of Prony's terms for bulk and shear moduli, α_i^K and α_i^G are relative bulk and shear moduli, and τ_i^K and τ_i^G are relaxation time for bulk and shear moduli. The physics behind Eqn.(5-23) and Eqn.(5-24) is that the bulk and shear moduli can be represented as a sum of a number of decaying terms, each term with its own relaxation time τ_i.

Correspondence principle The correspondence principle states that the solution to the problem for a linearly elastic viscoelastic material can be obtained by replacing the time-dependent parameters by their Laplace transform multiplied by the variable *s* of the transform. The time-domain response of a certain input can be obtained by transforming back by inverse Laplace transform.

Taking Laplace transform to Eqn.(5-21) and Eqn.(5-22), the constitutive equation in s domain is

$$\hat{\sigma}(x,s) = \hat{K}^*(s)\hat{\varepsilon}(s) = s\hat{K}(s)\hat{\varepsilon}(s) \tag{5-25}$$

$$\hat{\tau}(x,s) = \hat{G}^*(s)\hat{\gamma}(s) = s\hat{G}(s)\hat{\gamma}(s) \tag{5-26}$$

where the Laplace and inverse Laplace transform is defined as

$$L^{-1}\left\{\overline{f}(s)\right\} = \frac{1}{2\pi i}\int_{r-i\infty}^{r+i\infty} e^{st}\,\overline{f}(s)ds = f(t),\ \forall t > 0, r \in R \tag{5-27}$$

$$L^{-1}\left\{\overline{f}(s)\right\} = \frac{1}{2\pi i}\int_{r-i\infty}^{r+i\infty} e^{st}\,\overline{f}(s)ds = f(t),\ \forall t > 0, r \in R \tag{5-28}$$

Therefore, the integral equation between stress and strain for viscoelastic materials has been transformed to a linear elastic relation between stress and strain in s space.

Taking Laplace transform to Eqn.(5-23) and Eqn.(5-24), Prony's series volumetric and diavometric stiffness in *s* domain becomes

$$\hat{K}(s) = K_0\left(\frac{\alpha_\infty^K}{s} + \sum_{i=1}^{n}\frac{\alpha_i^K}{\tau_i^K s + 1}\right) \tag{5-29}$$

$$\hat{G}(s) = G_0\left(\frac{\alpha_\infty^G}{s} + \sum_{i=1}^{n}\frac{\alpha_i^G}{\tau_i^G s + 1}\right) \tag{5-30}$$

Instead of solving the response in time domain, we may transform the equation from time-domain differential equation to s-domain algebraic equation. Inverse transform from s-domain back to time-domain and have the response in time-domain.

5.4 Elastic Solution of Longitudinal deformation

Consider a piezoelectric layer bonded on a structural component by an adhesive layer in between shown in Figure 5-1. An external force is applied on the structural component and the external loading transferred from the structural component to piezoelectric layer by adhesive induces stress reduction.

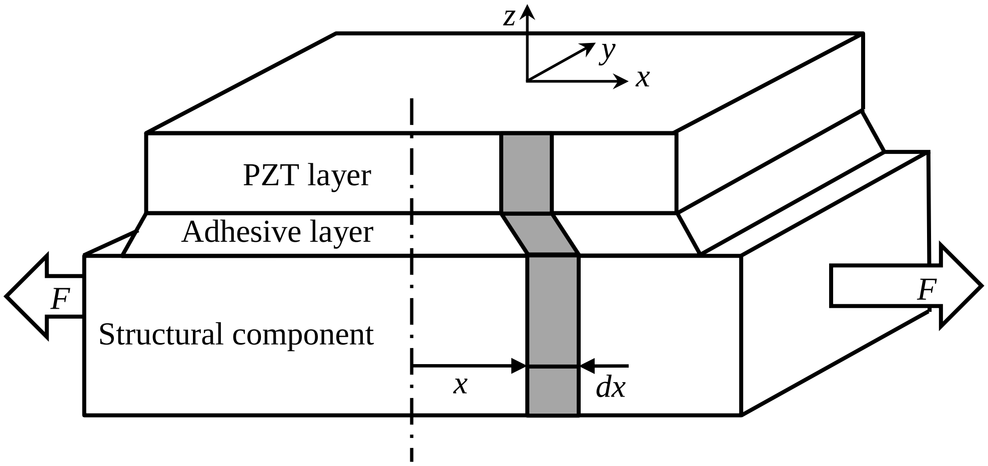

Figure 5-5 Schematic of a SHM system with an external force applied in *x*- (axial) direction.

To simplify the problem, the following assumptions are used to model the viscoelastic behavior of the tri-layer load transfer design.

- Consider the stress applied in *x*-direction only.
- The piezoelectric and structural layers is assumed to have linear elastic behavior.

- The adhesive is assumed to behave linear elastically in this section
- Adhesive does not carry axial force
- Ignore the effect bending moment

Take an element of length *dx*, at position *x* from the center of SHM system on each layer, the free body diagram can be shown in Figure 5-6.

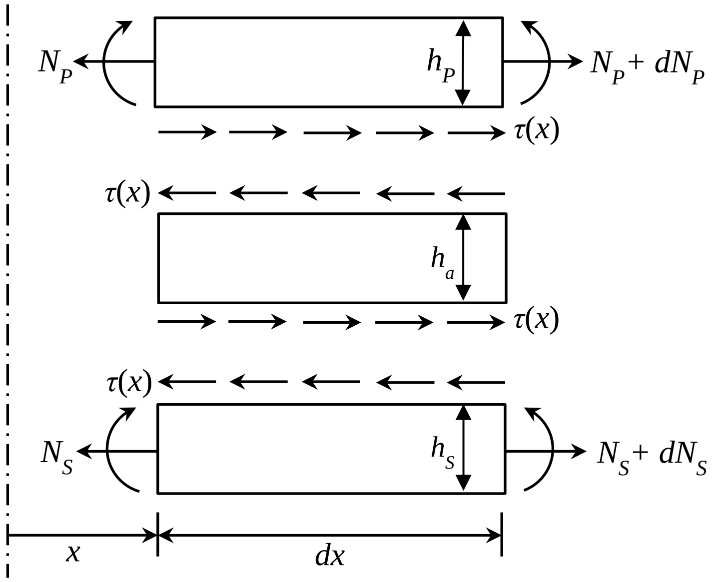

Figure 5-6 Free body diagram of each layer of SHM system

Consider the free-body diagram of the bottom and top layer shown in Figure 5-6 and take equilibrium of forces to each layer in the *x* direction.

$$-N_S + N_S + \frac{\partial N_S}{\partial x}dx - \tau dx = 0 \tag{5-31}$$

$$-N_P + N_P + \frac{\partial N_P}{\partial x}dx + \tau dx = 0 \tag{5-32 }$$

The static equilibrium of motion becomes

$$\frac{\partial N_S}{\partial x} - \tau = 0 \tag{5-33}$$

$$\frac{\partial N_P}{\partial x} + \tau = 0 \tag{5-34 }$$

where N_i (i = S, P) denotes the axial force per unit width, and τ is the shear stress per unit width.

Consider axial forces as well as thermal expansions, total strain in top and bottom layers are given by

$$\varepsilon_S = \frac{du_S}{dx} = \frac{N_S}{K_S h_S} + \alpha_S \Delta T \tag{5-35}$$

$$\varepsilon_P = \frac{du_P}{dx} = \frac{N_P}{K_P h_P} + \alpha_P \Delta T\ , \tag{5-36}$$

where α_S and α_P are thermal expansion coefficient, K_S and K_P are effective Young's modulus of material S and P layer and they are given by

$$K_S = \frac{E_S}{1-\nu_S} \tag{5-37}$$

$$K_P = \frac{E_P}{1-\nu_P} \tag{5-38}$$

Therefore, the displacement at position x in top and bottom layers are given below

$$u_S = \int (\frac{N_S(x)}{K_S h_S} + \alpha_S \Delta T) dx + c_S \tag{5-39}$$

$$u_P = \int (\frac{N_P(x)}{K_P h_P} + \alpha_P \Delta T) dx + c_P\ , \tag{5-40}$$

Consider a symmetric structure about y-axis, the displacement u_S is zero at x = 0, which gives c_S = c_P = 0. Also, external loading is applied at two ends of the structure only, the axial force remains constant in x direction. Therefore, the displacement of each layer at arbitrary position x becomes

$$u_S(x) = (\frac{N_S}{K_S h_S} + \alpha_S \Delta T) x \tag{5-41}$$

$$u_P(x) = (\frac{N_P}{K_P h_P} + \alpha_P \Delta T) x\ , \tag{5-42}$$

From the shear constitutive equation, the shear strain of the bonded layer induced by the displacement of the top and bottom layer can be determined by Hooke's law as

$$\frac{\tau_{xy,A}}{G_A} = \frac{u_S - u_P}{h_A}\,, \tag{5-43}$$

where $\tau_{xy,A}$ are in-plane shear stress in adhesive layer and G_A is the effective shear modulus of the adhesive layer.

Displacement response Apply differential operator d/dx to Eq.(5-35) and Eq.(5-36), we obtain

$$\frac{d^2u_S}{dx^2} = \frac{1}{K_S h_S}\frac{dN_S}{dx} \tag{5-44}$$

$$\frac{d^2u_P}{dx^2} = \frac{1}{K_P h_P}\frac{dN_P}{dx}\,. \tag{5-45}$$

Substitute Eqn.(5-32) into Eqn.(5-45) we obtain

$$\frac{d^2u_P}{dx^2} = -\frac{1}{K_P h_P} G_A \frac{u_S - u_P}{h_A}\,. \tag{5-46}$$

Further simplifies Eqn.(5-46) results to an ordinary differential equation as

$$\frac{d^2}{dx^2}u_P - \frac{G_A}{K_P h_P h_A}u_P = -\frac{G_A}{K_P h_P h_A}u_S\,. \tag{5-47}$$

Eqn.(5-47) is the governing equation which determines the displacement response of the top layer u_P by given the input displacement of the bottom layer u_S.

Shear stress response To examine the response of the shear stress in the adhesive $\tau_{xy,A}$, subtracting Eqn.(5-45) from Eqn.(5-44) results to

$$\frac{d^2}{dx^2}(u_S - u_P) = \frac{1}{K_S h_S}\frac{dN_S}{dx} - \frac{1}{K_P h_P}\frac{dN_P}{dx} \qquad (5\text{-}48)$$

Apply Eqn.(5-31) and Eqn.(5-32) to the right hand side of Eqn.(5-48), Eqn.(5-43) into left hand side of Eqn.(5-48), Eqn.(5-48) becomes

$$\frac{h_A}{G_A}\frac{d^2}{dx^2}\tau_A - (\frac{1}{K_S h_S} + \frac{1}{K_P h_P})\tau_A = 0 \qquad (5\text{-}49)$$

Second order differential equation governs the shear stress in the adhesive can be rewritten as

$$\frac{d^2}{dx^2}\tau_A - \frac{G_A}{h_A}(\frac{1}{K_S h_S} + \frac{1}{K_P h_P})\tau_A = 0\,, \qquad (5\text{-}50)$$

and Eqn.(5-41) and Eqn.(5-42) provide displacement boundary conditions to solve the Eq.(5-50).

Eqn.(5-47) and Eqn.(5-50) summarize the second order differential equations which govern displacement on the top layer and shear stress in the adhesive, respectively. For proposed SHM system, the purpose of the load transfer design is to study the reduction ratio of stress, which is defined by stress at the top-most layer to the stress on the bottom; therefore, the displacement response of the top layer u_P by given the displacement of the bottom structure u_S matters to evaluate the design. To further solve the displacement response of the top layer u_P shown in Eqn.(5-47), assume the structural component is under a constant local strain ε_x and that the symmetry of stress distribution with respect to the center of the device is applied, the displacement distribution in *x*-direction u_S on the structural component layer is

$$u_S = x\varepsilon_S\,. \qquad (5\text{-}51)$$

Substitute Eqn.(5-51) into Eqn.(5-47) the governing equation of the adhesive layer yields to

$$\frac{d^2 u_P(x)}{dx^2} - \alpha^2 u_P(x) = -\alpha^2 \varepsilon_S x\,, \tag{5-52}$$

where $\alpha^2 = \dfrac{G_A}{h_P h_A K_P}$.

To solve the ordinary differential equation shown in Eqn.(5-52), we assume general solution $u_{P,h}(x)$ and particular solution are $u_{P,p}(x)$

$$u_{P,h}(x) = A \sinh \alpha x + B \cosh \alpha x\,. \tag{5-53}$$

$$u_{P,p}(x) = Cx\,. \tag{5-54}$$

Apply Eq.(5-54) to Eq.(5-52), we obtain $C = \varepsilon_S$ and the particular solution yields to

$$u_{P,p}(x) = \varepsilon_S x\,. \tag{5-55}$$

With the symmetric boundary condition $u_S(0) = 0$, the homogeneous solution for $u_{S,h}(x)$ is found to be

$$u_{P,h}(x) = A \sinh \alpha x\,. \tag{5-56}$$

The general solution including homogeneous and particular terms result to

$$u_P(x) = A \sinh \alpha x + \varepsilon_S x\,. \tag{5-57}$$

The strain ε_S can be found by definition as $\varepsilon_S = du_S / dx$

$$\varepsilon_P(x) = \alpha A \cosh \alpha x + \varepsilon_S\,. \tag{5-58}$$

The normal and shear stress distribution on the top layer yields to

$$\sigma_{x,P}(x) = \alpha K_P A \cosh \alpha x + K_P \varepsilon_S\,. \tag{5-59}$$

By traction free boundary condition $\sigma_P(L) = 0$, unknown constant can be found as

$$A = -\frac{\varepsilon_S}{\alpha \cosh \alpha L}\,. \tag{5-60}$$

Apply Eqn.(5-60) into Eqn.(5-58) and Eqn.(5-59), strain $\varepsilon_x(x)$ and stress distribution $\sigma_x(x)$ on the top layer leads to

$$\varepsilon_x(x) = \varepsilon_S(1 - \frac{\cosh \alpha x}{\cosh \alpha L}) \tag{5-61}$$

$$\sigma_x(x) = K_P \varepsilon_S (1 - \frac{\cosh \alpha x}{\cosh \alpha L}) . \tag{5-62}$$

Apply Eq.(5-57) to Eq.(5-43), the shear stress in the adhesive layer can be found as

$$\tau_{xy,A}(x) = \sqrt{\frac{h_P}{h_A} K_P G_A} \frac{\varepsilon_S}{\cosh \alpha L} \sinh \alpha x . \tag{5-63}$$

The reduction factor of the strain from bottom layer to top layer R_ε is defined as

$$R_\varepsilon = \frac{\varepsilon_{P,\max}}{\varepsilon_{S,\max}} , \tag{5-64}$$

The maximum strain on both top and bottom layer can be found from Eq.(5-58) as

$$\varepsilon_{P,\max} = \varepsilon_P(x=0) = \varepsilon_S(1 - \frac{1}{\cosh \alpha L}) , \tag{5-65}$$

where the strain in the bottom layer ε_P is given, and we assume the strain distribution on the bottom layer keeps constant in *x*-direction as below

$$\varepsilon_{S,\max} = \varepsilon_S . \tag{5-66}$$

Therefore, Eqn.(5-64) becomes

$$R_\varepsilon = (1 - \frac{1}{\cosh \alpha L}) . \tag{5-67}$$

Eq.(5-65) shows that the strain distribution along the top surface of the piezoelectric lamina is an even function, i.e. symmetric about x = 0, the middle of the tri-layer structure, and the strain reaches its maximum value at the symmetric axis.

Similarly, we define the reduction factor of the stress from bottom layer to top layer R_σ as

$$R_\sigma = \frac{\sigma_{P,\max}}{\sigma_{S,\max}}, \tag{5-68}$$

The maximum strain on both top and bottom layer can be found as

$$\sigma_{P,\max} = \sigma_P(x=0) = K_P \varepsilon_S (1 - \frac{1}{\cosh \alpha L}), \tag{5-69}$$

where the strain in the bottom layer ε_S is given, and we assume the strain distribution on the bottom layer keeps constant in *x*-direction as shown below

$$\sigma_{P,\max} = K_P \varepsilon_P. \tag{5-70}$$

Therefore, the stress reduction factor defined in Eq.(5-64) becomes

$$R_\sigma = \frac{K_p}{K_s}(1 - \frac{1}{\cosh \alpha L}). \tag{5-71}$$

Eqn.(5-69) shows that similar to the strain distribution, the stress distribution along the top surface of the piezoelectric lamina is an even function, i.e. symmetric about *x* = 0, the middle of the tri-layer structure, and the strain reaches its maximum value at the symmetric axis.

5.5 Finite Element Result of Load Transfer Design in Elastic Assumption

In order to verify the stress and strain reduction of load transfer design in Eqn.(5-65) and Eqn.(5-71). The ANSYS finite element program is used to analyze stress and strain distribution on the top surface of the piezoelectric ceramic.

A piezoelectric plate is bonded on a structural component by an adhesive layer in between. To model a practical case that the dimensions of piezoelectric ceramic and adhesive is relative much smaller than the component, the boundary conditions are set as: 1. all of the three layers are symmetric about *x* and *z* axis, and 2. displacement of the bottom of the structural component is constrained in *y* direction. The loadings of the FEM model is set to apply a pair of tension forces in *x* direction, uniformly distributed on the cross section of the structural component.

Figure 5-7 (a) and (b) show the physical model of the load transfer design in isoparametric and side view respectively, while Figure 5-7 (c) and (d) show FEM model presented by the mesh pattern and pattern with boundary conditions and external loadings, respectively.

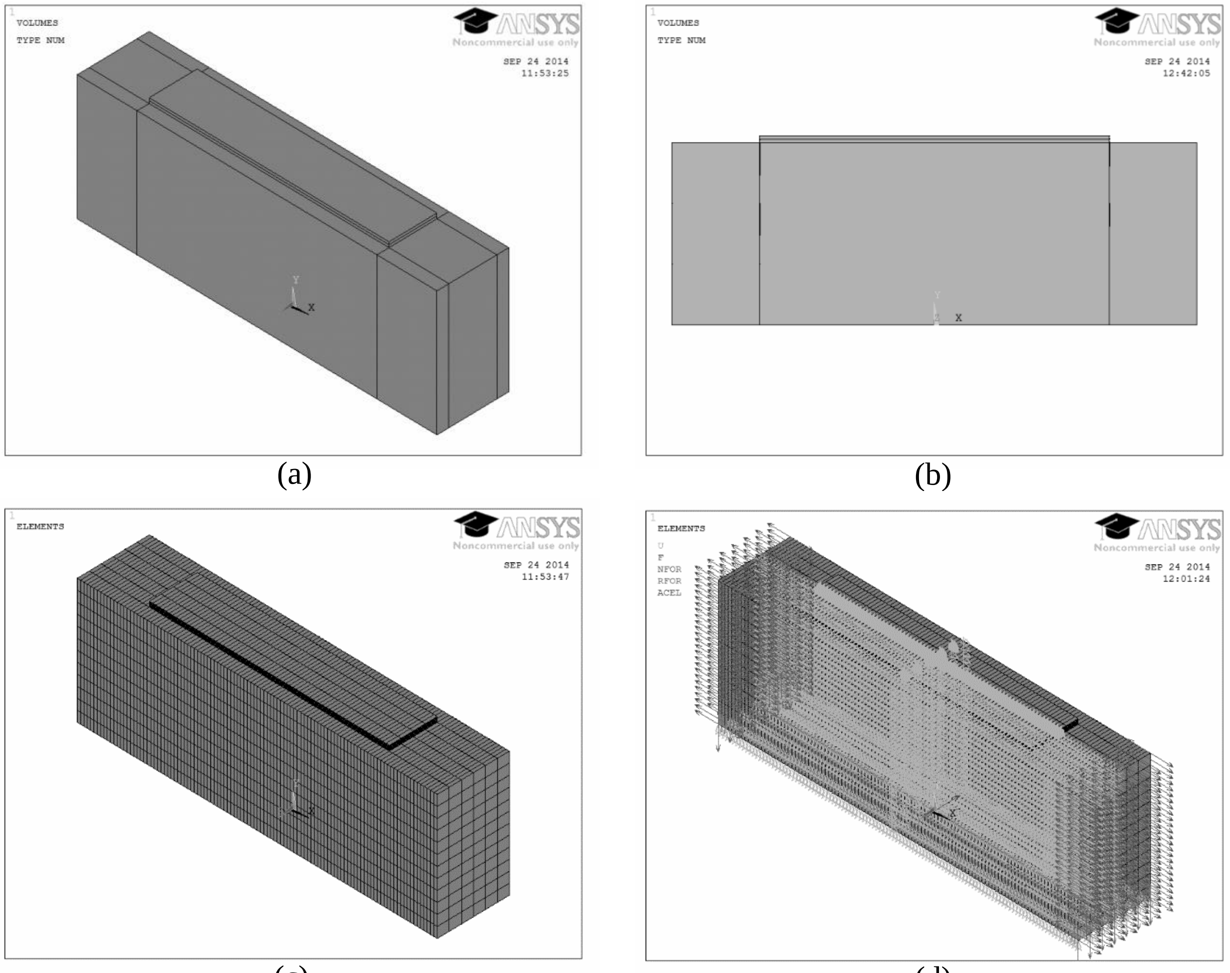

(a) (b)

(c) (d)

Figure 5-7 (a) Physical model of load transfer design (isoparametric view), (b) Physical model of load transfer design (side view), (c) FEM model of load transfer design with mesh pattern, (d) FEM model of load transfer design with boundary conditions and loadings.

Figure 5-7 (a) and (b) indicate that a relative thicker structural component than a piece of piezoelectric ceramic and an adhesive layer in between. The FEM model shown in Figure 5-7 (c) and (d) depicts that the mesh pattern has 29835 nodes, 12240 20-noded elements type of

`SOLID186` with boundary conditions and external loadings mentioned above. Detailed APDL script on an example of rubber solid as the adhesive material with 0.5 mm in thickness is list in Appendix V. Two materials, rubber solid and FM-73 epoxy, one is much compliant than the other shown in Table 5-1are chosen for adhesives.

Table 5-1 Elastic materials of adhesives

Case 1: Rubber solid
Young's Modulus: 140 MPa Poisson ratio: 0.45 Density: 1100 kg/m^3
Case 2: FM-73 epoxy structural adhesive
Young's Modulus: 2.7 GPa Poisson ratio: 0.35 Density: 875 kg/m^3

Static loading are simulated by applying a pair of force, which induces 100 MPa tensile stress on both ends of the cross section of the structural component.

Figure 5-8 shows the normalized stain distribution $\varepsilon_{P,max} / \varepsilon_S$ on the top surface of the piezoelectric ceramic against the normalized location x/L with various thickness of adhesive layer h_A = 0.5 mm ~ 5.0 mm, by theoretical derivation in Eqn.(5-65) and FEM results. The results of theoretical model and FEM are represent in different types of lines and markers, respectively. It is obvious from Figure 5-8 that the thicker the adhesive layer is, the more strain is reduced. The typical thickness of the adhesive layer is around 0.1mm~1.0mm and the corresponding strain reduction factor is ranging from 90% down to 35%. Figure 5-8 also shows good agreement between theoretical model and FEM results. The theoretical results overestimate the stress on the piezoelectric ceramic if the adhesive is getting thicker, since under the assumption we made previously that the adhesive holds shear force only, the piezoelectric holds more stress than that the adhesive should hold.

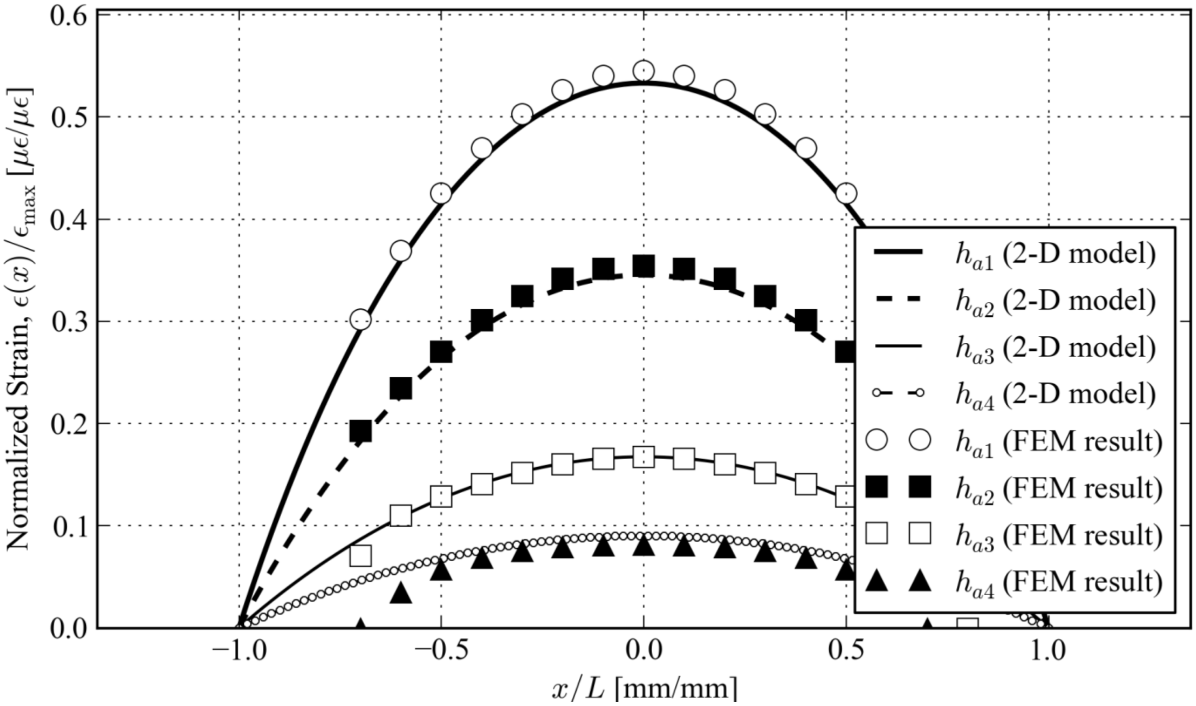

Figure 5-8 Normalized strain distribution along the top surface of the piezoelectric layer; theoretical model by lines, and FEM results by markers
(h_{a1} = 0.5 mm, h_{a2} = 1.0 mm, h_{a3} = 2.0 mm, h_{a4} = 5.0 mm; adhesive: rubber solid)

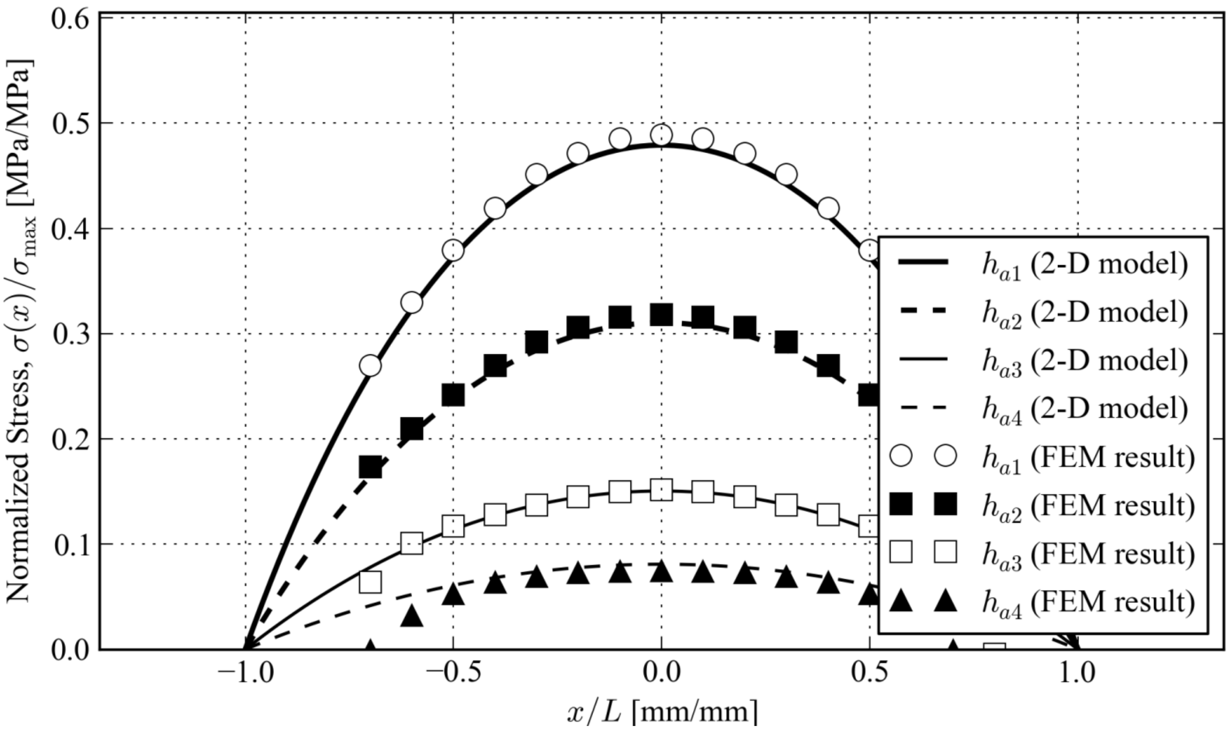

Figure 5-9 Normalized stress distribution along the top surface of the piezoelectric layer; theoretical model by lines, and FEM results by markers
(h_{a1} = 0.5 mm, h_{a2} = 1.0 mm, h_{a3} = 2.0 mm, h_{a4} = 5.0 mm; adhesive: rubber solid)

Similar to Figure 5-8 , Figure 5-10 shows the normalized stress distribution $\sigma_{P,\max} / \sigma_S$ on the top surface of the piezoelectric ceramic against the normalized location x/L with various thickness of adhesive layer h_A = 0.5 mm ~ 5.0 mm, by theoretical derivation in Eq.(5-69) and FEM results.

The results of theoretical model and FEM are represent in different types of lines and markers, respectively. It is obvious from Figure 5-8 that the thicker the adhesive layer is, the more stress is reduced. The typical thickness of the adhesive layer is around 0.5 mm~1.0 mm and the corresponding strain reduction factor is ranging from 80% down to 30%. The 5% reduction difference between strain and stress comes from the stiffness ratio K_p / K_s, which dominates the stress reduction factor shown in Eqn.(5-69). Theoretical prediction shows agrees the FEM results. The theoretical results predicts a little more stress more on the piezoelectric ceramic if the adhesive is getting thicker, as we see in strain reduction.

Figure 5-10 and Figure 5-11 show the theoretical prediction and FEM results with different adhesive material, FM-73 epoxy structural adhesive shown in Table 5-1and all of the boundary conditions and loadings are exactly the same as the case of rubber solid. Figure 5-10 and Figure 5-11 show that the stiff adhesive material (FM-73) may reduce less strain and stress than compliant adhesive material (rubber solid, see Figure 5-8 and Figure 5-10). The theoretical prediction for FM-73 adhesive overestimates the stress and strain more than that for rubber solid does. Since the stiffer adhesive holds much more stress, which is ignored in theoretical model.

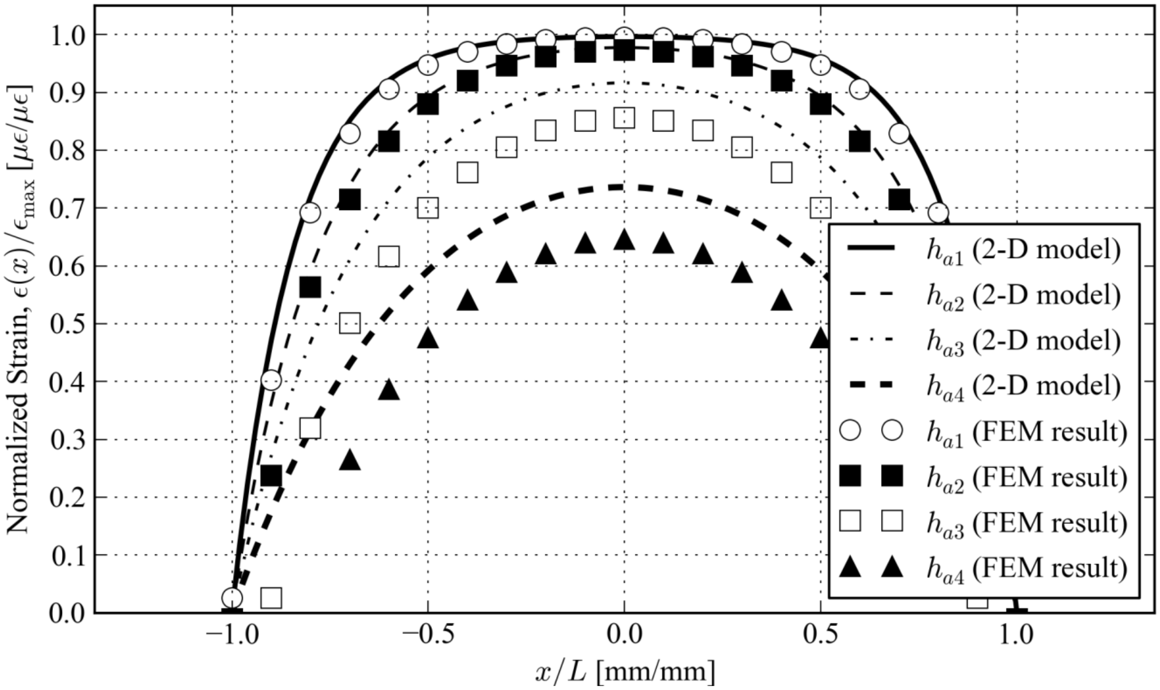

Figure 5-10 Normalized strain distribution along the top surface of the piezoelectric layer; theoretical model by lines, and FEM results by markers
(h_{a1} = 0.5 mm, h_{a2} = 1.0 mm, h_{a3} = 2.5 mm, h_{a4} = 5.0 mm; adhesive: FM-73 epoxy)

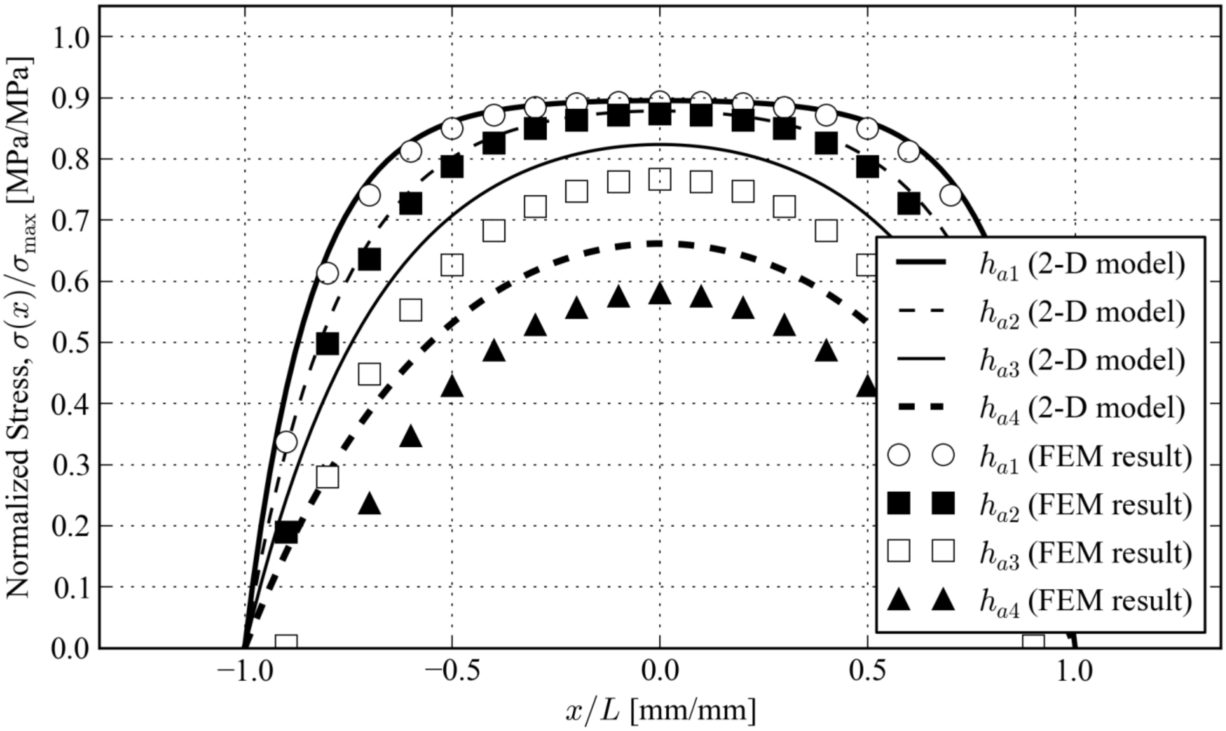

Figure 5-11 Normalized strain distribution along the top surface of the piezoelectric layer; theoretical model by lines, and FEM results by markers (h_{a1} = 0.5 mm, h_{a2} = 1.0 mm, h_{a3} = 2.5 mm, h_{a4} = 5.0 mm; adhesive: FM-73 epoxy)

5.6 Viscoelastic Solution of Longitudinal Deformation

To simplify the problem, the following assumptions are used to model the viscoelastic behavior of the tri-layer load transfer design.

- Consider the stress applied in *x*-direction only.
- The piezoelectric and structural layers are assumed to have linear elastic behavior.
- The adhesive is assumed to have linear viscoelastic behavior
- The generalized Maxwell model and Prony's series are used to model the shear relaxation behavior of the adhesive.
- Adhesive does not carry axial force
- Ignore the effect bending moment

$$\hat{\tau}(x,s) = \hat{G}^*(s)\hat{\gamma}(x,s) = s\hat{G}(s)\hat{\gamma}(s) \tag{5-72}$$

Define the Laplace transform of an arbitrary function $f(t)$ is $\hat{f}(s)$ as below

$$\hat{f}(s) = L\{f(t)\} \equiv \int_0^\infty e^{-st} f(t)dt \tag{5-73}$$

Taking Laplace transform to Eqn.(5-33) and Eqn.(5-34), the equation of force equilibrium for adherent layers can be written as

$$\frac{\partial \hat{N}_S}{\partial x} - \hat{\tau} = 0 \tag{5-74}$$

$$\frac{\partial \hat{N}_P}{\partial x} + \hat{\tau} = 0 \tag{5-75}$$

Eqn.(5-35) and Eqn.(5-36) in Laplace domain can be written as

$$\hat{\varepsilon}_S(x,s) = \frac{d\hat{u}_S(x,s)}{dx} = \frac{\hat{N}_S(x,s)}{K_S h_S} + \hat{\alpha}_S(x,s)\Delta T \tag{5-76}$$

$$\hat{\varepsilon}_P(x,s) = \frac{d\hat{u}_P(x,s)}{dx} = \frac{\hat{N}_P(x,s)}{K_P h_P} + \hat{\alpha}_P(x,s)\Delta T\ , \tag{5-77}$$

Similarly, taking Laplace transform to Eq.(5-43) and constitutive equation of adhesive can be written as

$$\hat{\gamma}_{xy,A}(x,s) = \frac{\hat{u}_S(x,s) - \hat{u}_P(x,s)}{h_A}\ . \tag{5-78}$$

In order to apply correspondence principle presented in Eqn.(5-25) and Eqn.(5-26), multiply $s\hat{G}(s)$ to both sides of the Eqn.(5-78), we have

$$s\hat{G}(s)\hat{\gamma}_{xy,A}(x,s) = \frac{s\hat{G}(s)}{h_A}[\hat{u}_S(x,s) - \hat{u}_P(x,s)]\ , \tag{5-79}$$

which leads to the shear stress in Laplace domain as

$$\hat{\tau}_{xy,A}(x,s)=\frac{s\hat{G}_A(s)}{h_A}[\hat{u}_S(x,s)-\hat{u}_P(x,s)]. \tag{5-80}$$

Applying Eqn.(5-74) ~ Eqn.(5-77) to Eqn.(5-80) becomes

$$\frac{d^2\hat{u}_S(x,s)}{dx^2}=\frac{1}{K_S h_S}\frac{d\hat{N}_S(x,s)}{dx} \tag{5-81}$$

$$\frac{d^2\hat{u}_P(x,s)}{dx^2}=\frac{1}{K_P h_P}\frac{d\hat{N}_P(x,s)}{dx} \tag{5-82}$$

Taking the first spatial derivative to (5-77) and applying to Eqn.(5-80), we obtain

$$\frac{d^2 u_P(x,s)}{dx^2}=-\frac{s\hat{G}_A(s)}{K_P h_P}\frac{\hat{u}_S(x,s)-\hat{u}_P(x,s)}{h_A}. \tag{5-83}$$

Further simplifying Eqn.(5-83) results to an ordinary differential equation as

$$\frac{d^2}{dx^2}\hat{u}_P(s)-\frac{s\hat{G}_A(s)}{K_P h_P h_A}\hat{u}_P(x,s)=-\frac{s\hat{G}_A(s)}{K_P h_P h_A}\hat{u}_S(x,s), \tag{5-84}$$

which governs the relation of displacement between structural component and piezoelectric ceramic.

Shear stress response in s domain

To determine the relation between shear stress in adhesive and normal stress in structural component and piezoelectric ceramic, substituting Eqn.(5-81) from Eqn.(5-82) results to

$$\frac{d^2}{dx^2}\left(\hat{u}_S(x,s)-\hat{u}_P(x,s)\right)=\frac{1}{K_S h_S}\frac{d\hat{N}_S(x,s)}{dx}-\frac{1}{K_P h_P}\frac{d\hat{N}_P(x,s)}{dx} \tag{5-85}$$

Reduction factor

Solving the ordinary differential equation governs the displacement at *x*-direction on piezoelectric layer with the symmetric conditions about *x*-axis shown in Eqn.(5-84), and assuming the structural component is under a constant local strain ε_x, we have the general solution as follows

$$\hat{u}_P(x,s) = \hat{\varepsilon}_S(s)(x - \frac{1}{\hat{\alpha}\cosh\hat{\alpha}L}\sinh\hat{\alpha}x)\,. \tag{5-86}$$

The strain and stress distribution on the piezoelectric layer in Laplace domain is

$$\hat{\varepsilon}_x(x,s) = \hat{\varepsilon}_S(s)(1 - \frac{\cosh\hat{\alpha}x}{\cosh\hat{\alpha}L}) \tag{5-87}$$

$$\hat{\sigma}_x(x,s) = K_P\hat{\varepsilon}_S(s)(1 - \frac{\cosh\hat{\alpha}x}{\cosh\hat{\alpha}L})\,. \tag{5-88}$$

The strain and stress reduction factor in Laplace domain can then be obtained as

$$\hat{R}_\varepsilon = (1 - \frac{\cosh\hat{\alpha}x}{\cosh\hat{\alpha}L}) \tag{5-89}$$

$$\hat{R}_\sigma = \frac{K_P}{K_S}(1 - \frac{\cosh\hat{\alpha}x}{\cosh\hat{\alpha}L})\,. \tag{5-90}$$

Taking the inverse Laplace transform, we can obtain the response in time domain for specific input strain; however, numerical method is required to perform the inverse Laplace transform.

5.7 Finite Element Result of Load Transfer Design in Viscoelastic Assumption

To verify the viscoelastic behavior of stress and strain reduction of load transfer design from Eqn.(5-87) to Eqn.(5-90). The ANSYS finite element program is used to analyze dynamic response of stress and strain on the top surface of the piezoelectric ceramic.

We use the same physical, FEM model and boundary conditions as we analyzed in linear elastic case shown in Figure 5-7. The physical model has a relative thicker structural component than a piece of piezoelectric ceramic and an adhesive layer in between, while the FEM model has 29835 nodes, 12240 20-noded elements type of `SOLID186` with symmetric about x-y and y-z plane.

To study the behaviors of placing viscoelastic materials in between, we specify time-dependent elastic modulus to the adhesive layer instead of oversimplifying to linear elastic case. Two viscoelastic materials are used: a rubber solid and structural adhesive epoxy FM-73.

We use generalized Maxwell model shown in Figure 5-4 to approximate the relaxation modulus for the adhesive; therefore, the Prony series in Eqn.(5-24) are adopted. The Prony constants for rubber solid and FM-73 epoxy film adhesive are shown in Table 5-2 and Table 5-3, respectively. The time-dependent relaxation moduli of rubber solid and FM-73 are shown in Figure 5-12.

Table 5-2 Prony series for rubber solid [106]

i	τ_i (sec.)	α_i (MPa/MPa)
1	0.2	0.33
2	0.4	0.33
E_0 = 140 MPa, v = 0.45, ρ = 1100 kg/m^3		

Table 5-3 Prony series for FM-73 epoxy film adhesive [107][108]

i	τ_i (sec.)	α_i (GPa/GPa)
1	0.009730	0.02728
2	0.090992	0.08933
3	0.878503	0.10980
4	7.491197	0.19120
E_0 = 2.7 GPa, v = 0.35, ρ = 875 kg/m^3		

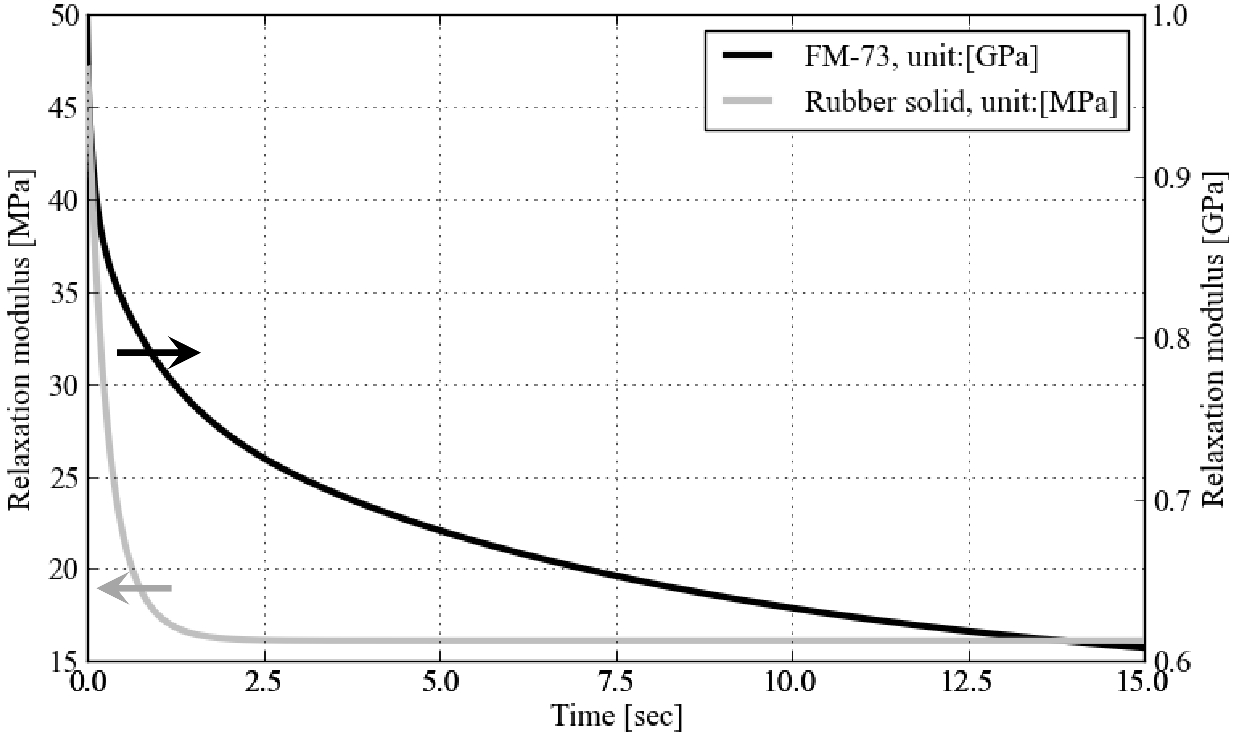

Figure 5-12 Relaxation stiffness of rubber solid and FM-73 adhesive

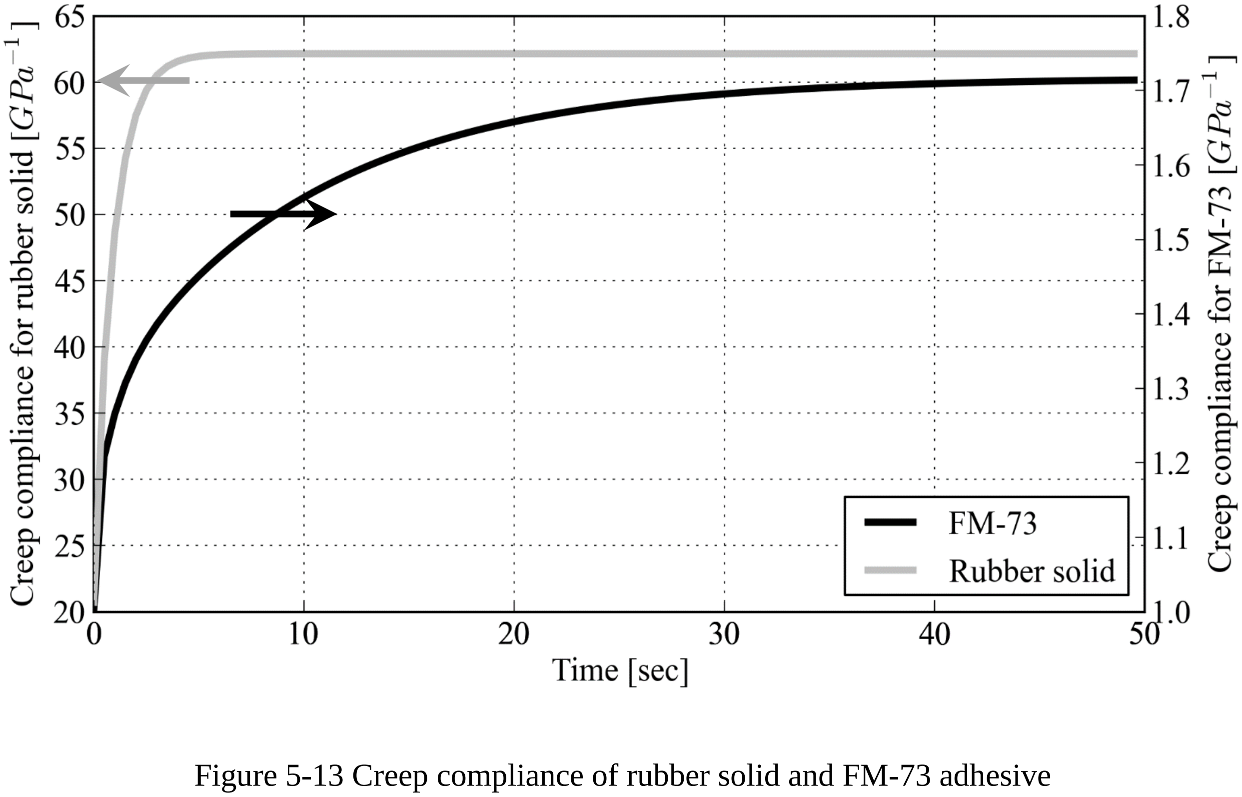

Figure 5-13 Creep compliance of rubber solid and FM-73 adhesive

Transient response

To study the transient response of stress and strain on each layer with various thickness of adhesive, we apply sinusoidal axial loadings of frequency 1.0 Hz to *x*-direction on the structural component, which induces uniform 675 $\mu\varepsilon$ of strain equivalent to 466 MPa of stress on the structural component. All of the induced stress and strain on the adhesive and piezoelectric ceramic are normalized by the stress and strain on the structural component, so that we can see not only the response but also the reduction factors of them. Figure 5-14 to Figure 5-17 (rubber solid as the adhesive material) and Figure 5-19 to Figure 5-22 (FM-73 as the adhesive material) show the transient response of stress and strain on the piezoelectric ceramic from 0 ~ 3.5 second. A normalized input with unity amplitude in 1.0 Hz of frequency in Figure 5-14 to Figure 5-17 and Figure 5-19 to Figure 5-22 is plotted to see the phase angle of stress and strain. Figure 5-18 and Figure 5-23 summarized Figure 5-14 to Figure 5-17 and Figure 5-19 to Figure 5-22, respectively, showing how Lissajous loops evolve in thickness under the same condition. This applies sinusoidal axial loadings frequency of 1.0 Hz to the *x*-direction on the structural component, which induces uniform 675 $\mu\varepsilon$ of strain equivalent to 466 MPa of stress on the structural component. In the Lissajous figure shown in Figure 5-18, normalized stress on the structural component is shown on the *x*-axis and normalized stress on the piezoelectric patch on the y-axis. This pattern was elliptical in the first and third quarters and rotating clockwise throughout the curve, which illustrates that the sinusoidal stress on the piezoelectric patch phase leads the sinusoidal stress on the structural component. The length ratio of minor axis to major axis of each eclipse illustrates that the thicker adhesive induces more phase lead of the stress on the piezoelectric patch (using structural component as a reference). Figure 5-18 and Figure 5-23 also illustrate that the more compliant adhesive (rubber solid) has more phase lead of stress on the piezoelectric patch to that on structural component than the less compliant adhesive (FM-73).

Detailed APDL script on an example of rubber solid as the adhesive material with 0.5 mm in thickness is list in Appendix VI.

To compare the results of theoretical model and FEM, we take inverse Laplace transform of Eqn.(5-87) to Eqn.(5-90) by a Python programmed Talbot approach, a numerical method of taking inverse Laplace transform. Detailed program is list in Appendix VII.

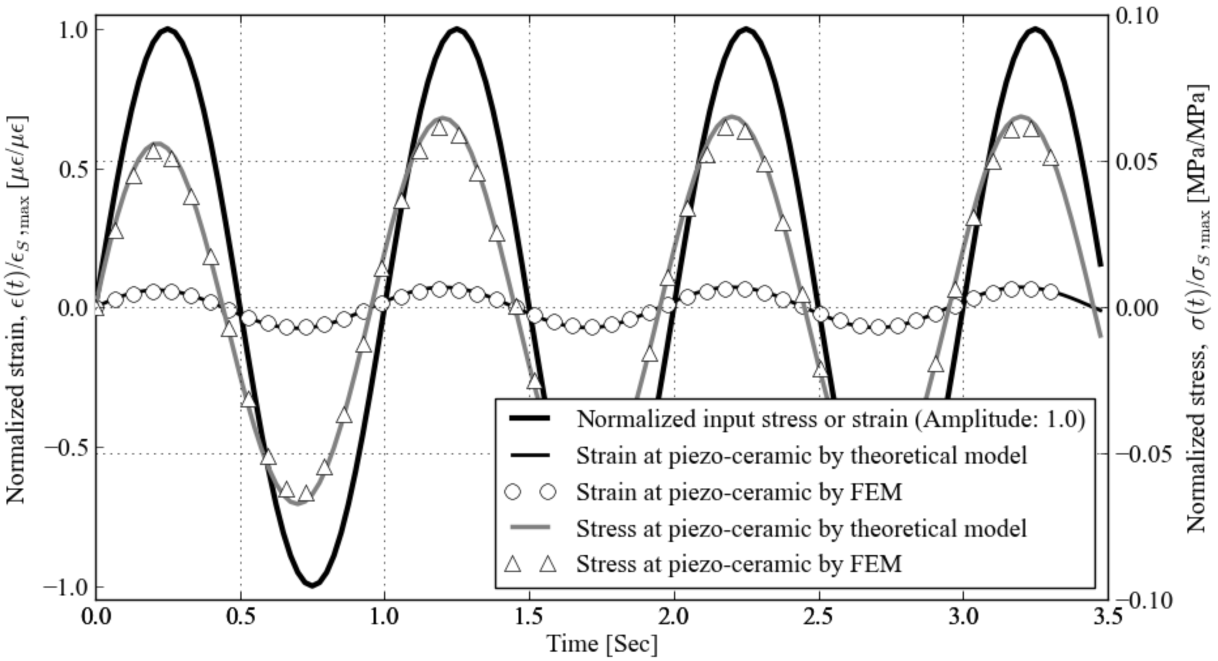

Figure 5-14 Transient respond of load transfer design (stress is normalized by 466 MPa, strain is normalized by 675 με; adhesive material: rubber solid, thickness of adhesive: 5.0 mm).

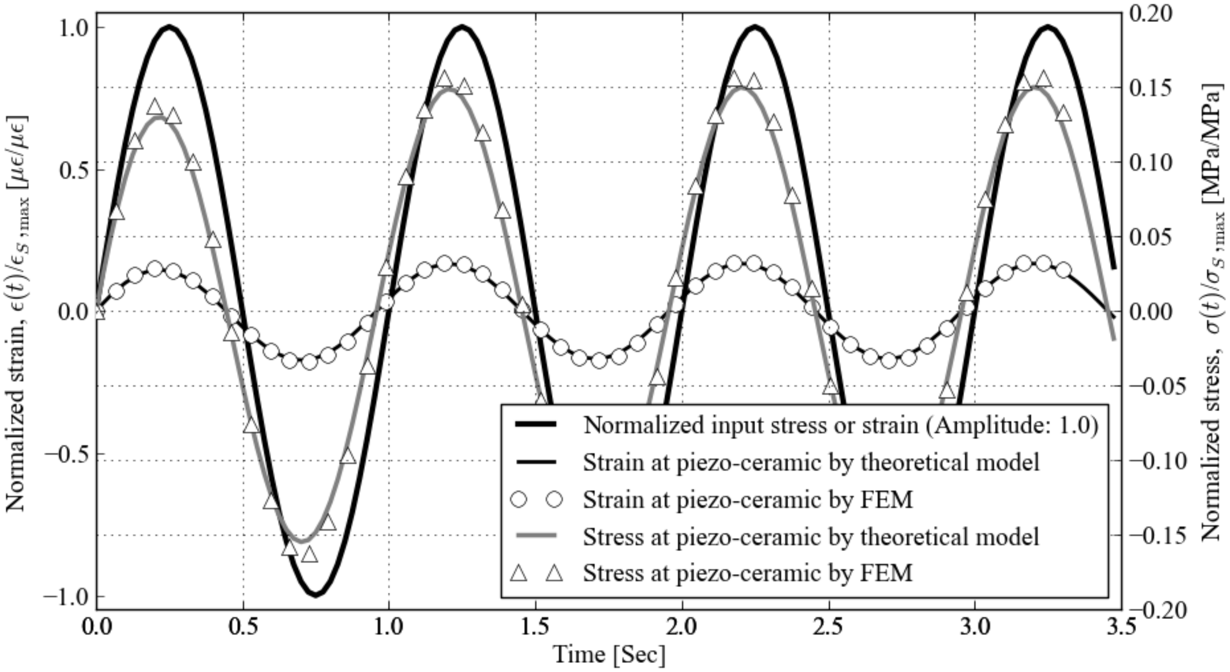

Figure 5-15 Transient respond of load transfer design (stress is normalized by 466 MPa, strain is normalized by 675 με; adhesive material: rubber solid, thickness of adhesive: 2.0 mm).

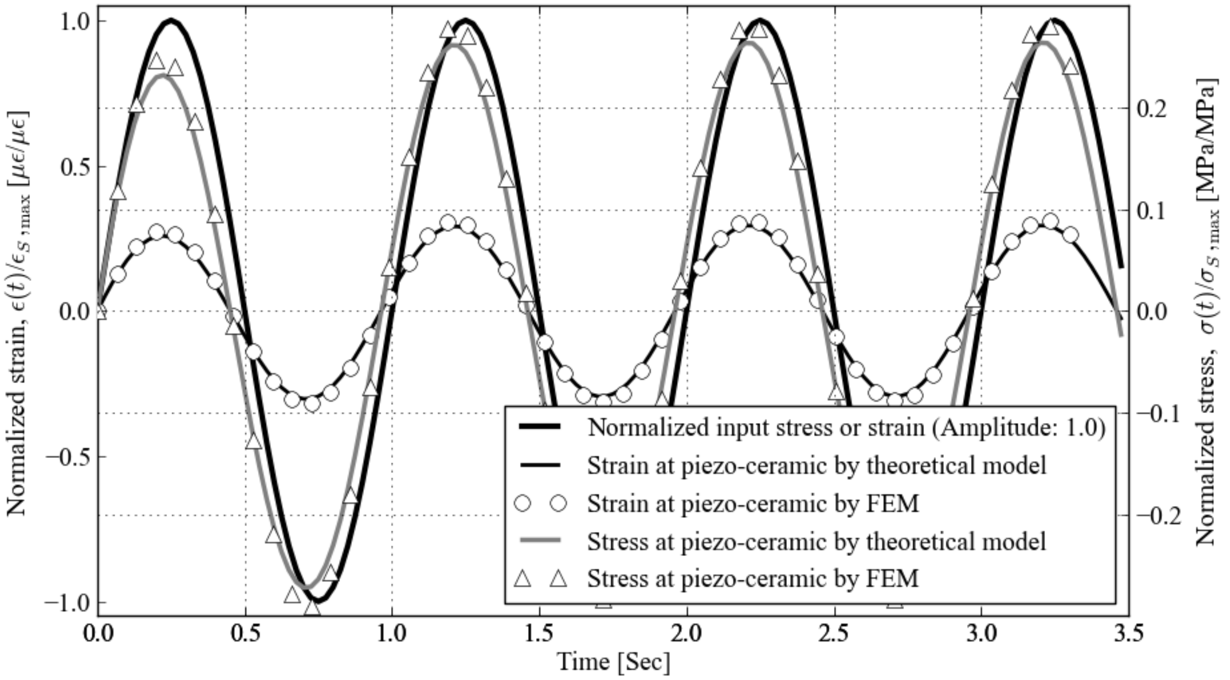

Figure 5-16 Transient respond of load transfer design (stress is normalized by 466 MPa, strain is normalized by 675 με; adhesive material: rubber solid, thickness of adhesive: 1.0 mm).

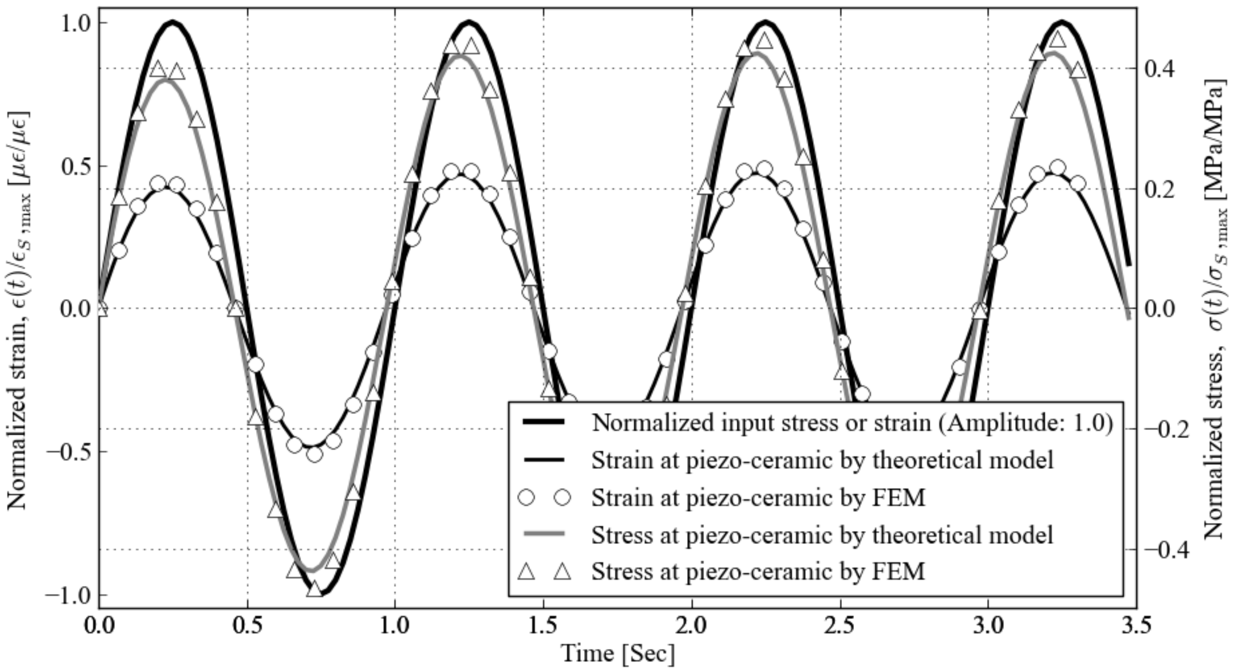

Figure 5-17 Transient respond of load transfer design (stress is normalized by 466 MPa, strain is normalized by 675 με; adhesive material: rubber solid, thickness of adhesive: 0.5 mm).

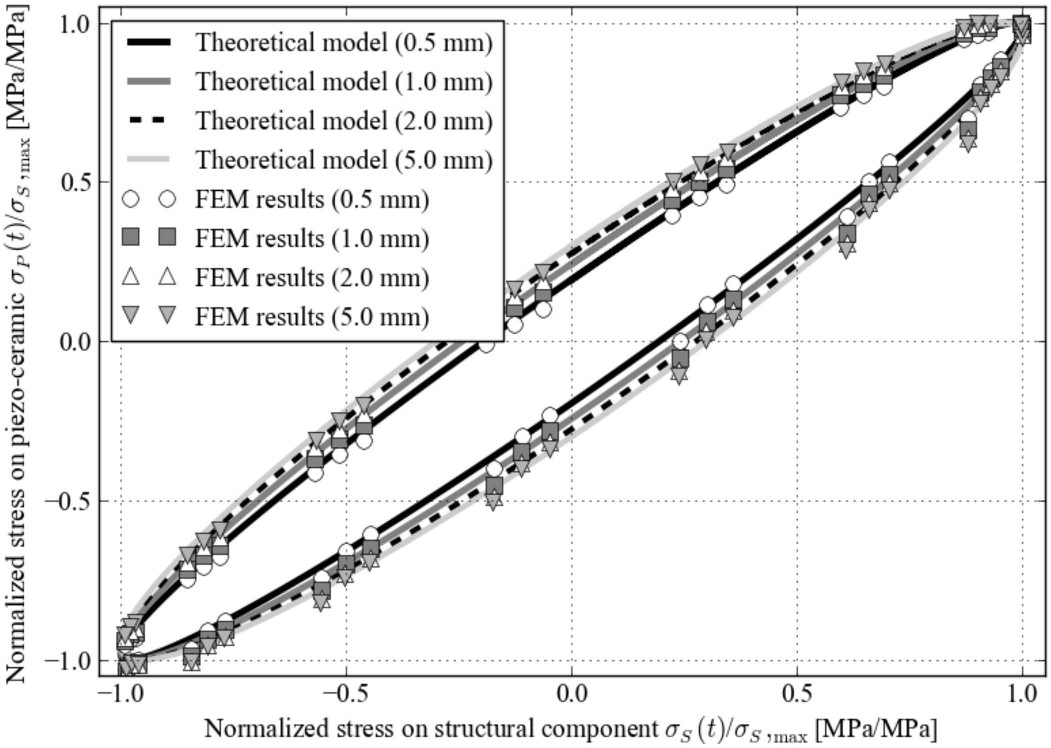

Figure 5-18 Stress on the piezo-ceramic σ_P vs stress on the structural component σ_S (both in *x* direction). Elliptical Lissajous figures for various thickness of rubber solid adhesive.

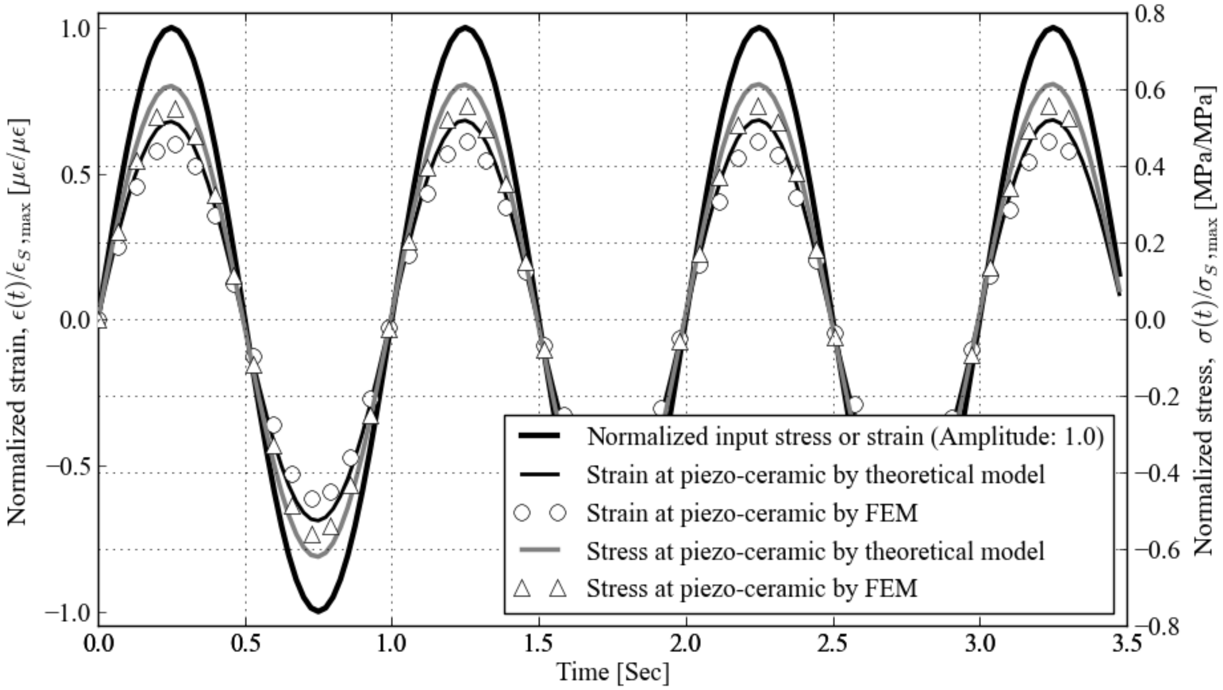

Figure 5-19 Transient respond of load transfer design (stress is normalized by 466 MPa, strain is normalized by 675 με; adhesive material: FM-73 epoxy film, thickness of adhesive: 5.0 mm).

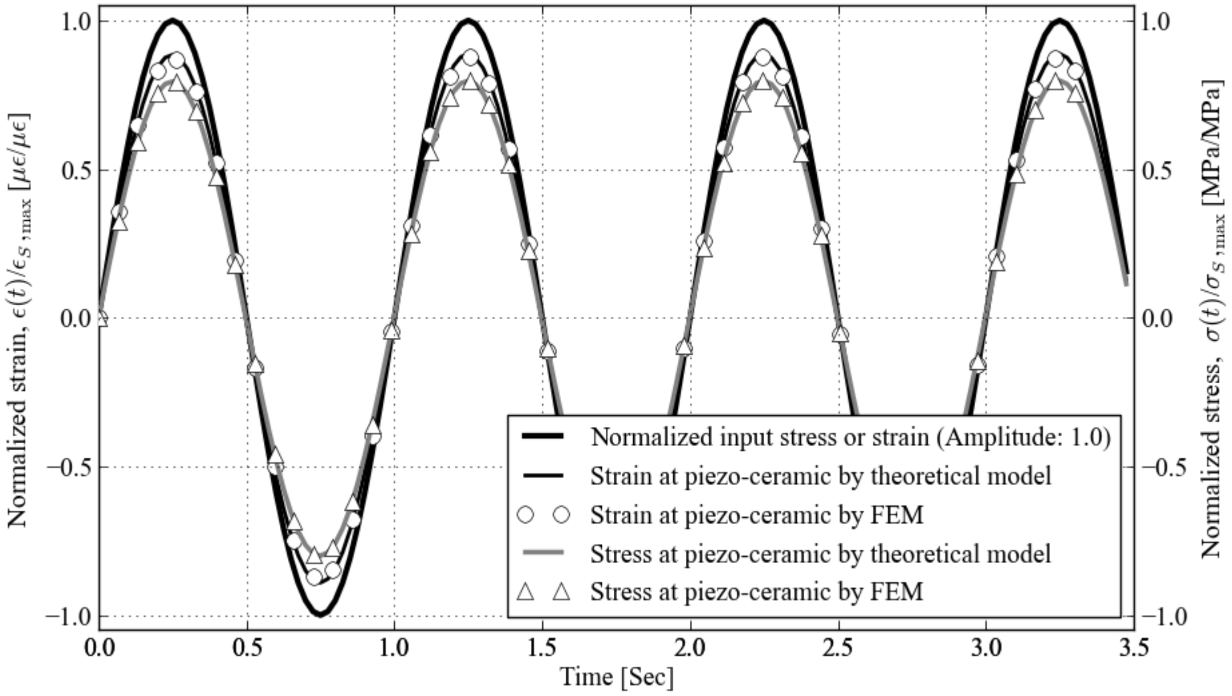

Figure 5-20 Transient respond of load transfer design (stress is normalized by 466 MPa, strain is normalized by 675 με; adhesive material: FM-73 epoxy film, thickness of adhesive: 2.0 mm).

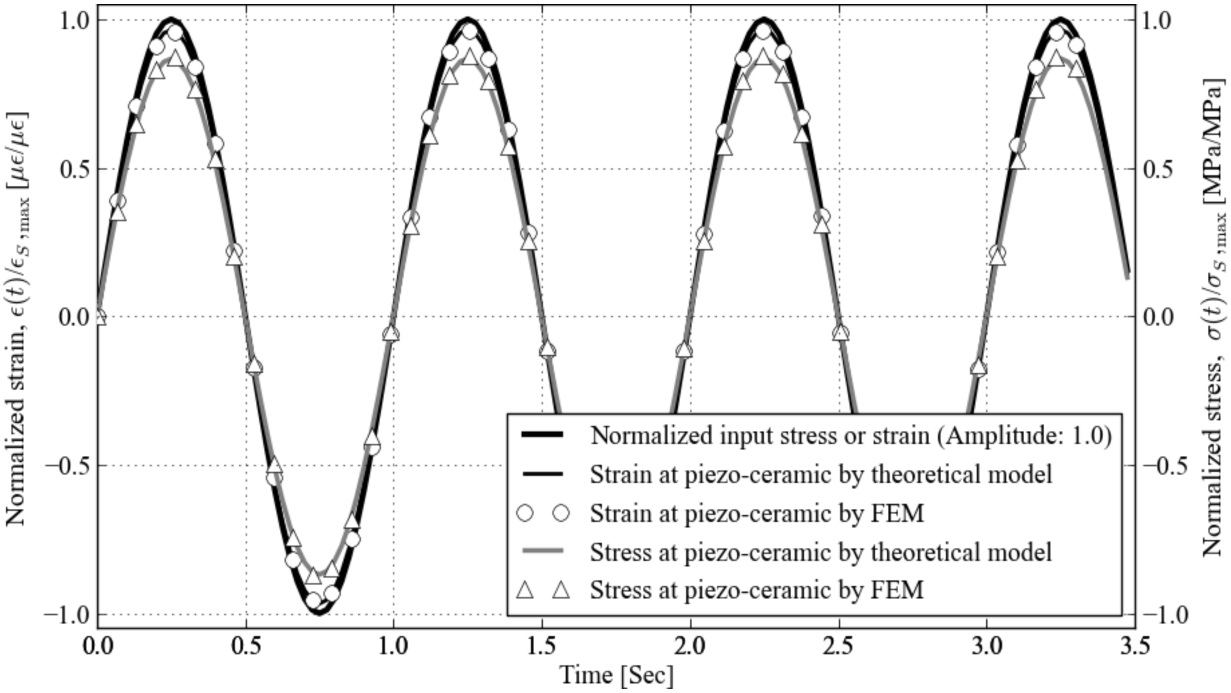

Figure 5-21 Transient respond of load transfer design (stress is normalized by 466 MPa, strain is normalized by 675 με; adhesive material: FM-73 epoxy film, thickness of adhesive: 1.0 mm).

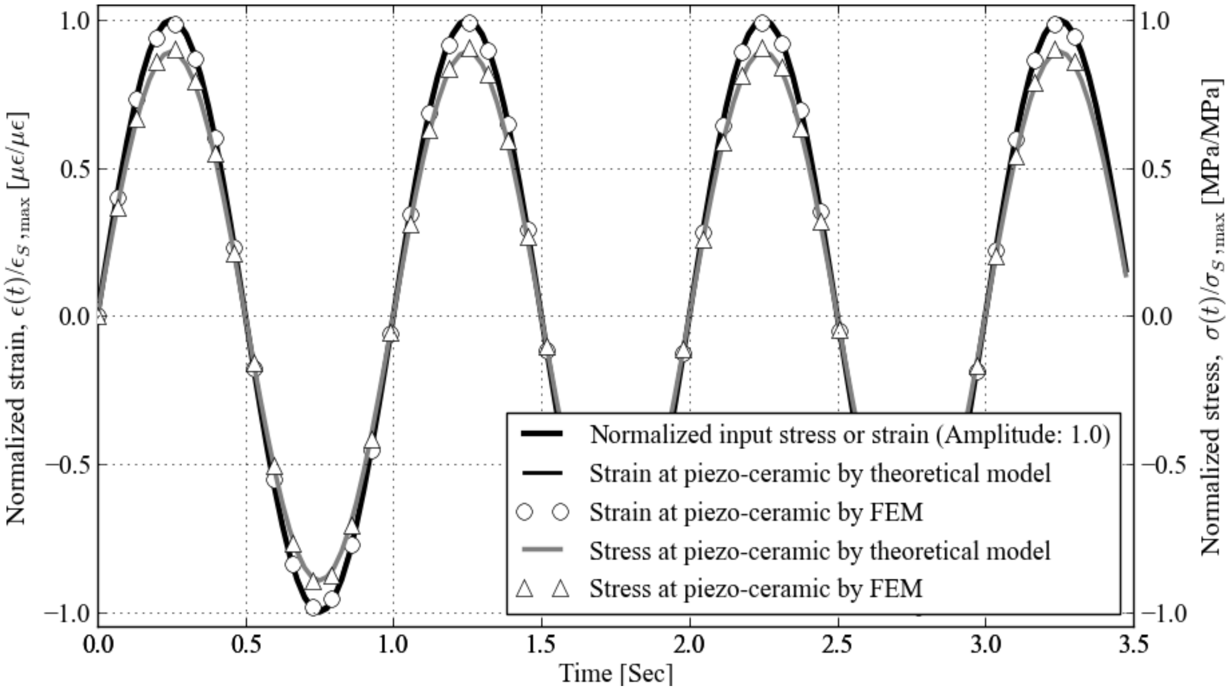

Figure 5-22 Transient respond of load transfer design (stress is normalized by 466 MPa, strain is normalized by 675 με; adhesive material: FM-73 epoxy film, thickness of adhesive: 0.5 mm).

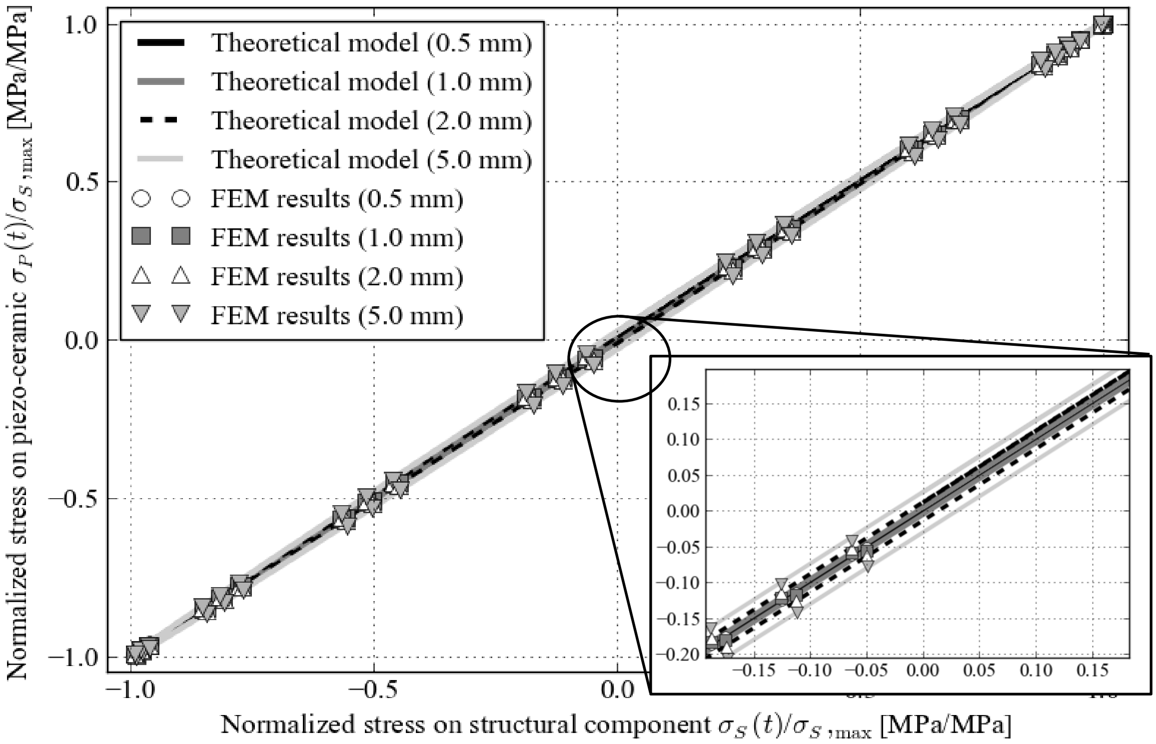

Figure 5-23 Stress on the piezo-ceramic σ_P vs stress on the structural component σ_S (both in x direction). Elliptical Lissajous figures for various thickness of FM-73 adhesive.

Table 5-4 summarizes the theoretical predictions and FEM results of stress reduction factors with various thickness of rubber solid or FM-73 epoxy. The numbers outside the parentheses are results from elastic solutions, while numbers in the parentheses are results from viscoelastic solutions. The viscoelastic model of the materials considers the energy dissipation so that it results to a higher stress reduction than the elastic model. Table 5-4 also appears that the thicker adhesive reduces larger stress. Theoretical predictions and FEM results show good agreement and the errors between them are less than 10% in general.

Table 5-4 Summary of the stress reduction factor of load transfer design
[elastic solution (viscoelastic solution)]

Thickness of adhesive, h_a	Rubber Solid		FM-73 Epoxy	
	Theoretical model	FEM	Theoretical model	FEM
5.0 mm	0.095 (0.07)	0.08 (0.065)	0.66 (0.60)	0.58 (0.55)
2.0 mm	0.18 (0.15)	0.18 (0.16)	0.76 (0.75)	0.82 (0.75)
1.0 mm	0.36 (0.26)	0.36 (0.28)	0.88 (0.90)	0.88 (0.87)
0.5 mm	0.54 (0.42)	0.55 (0.45)	0.90 (0.90)	0.90 (0.90)

5.8 Conclusions

In chapter five, we proposed a load transfer design, an adhesive layer glued between piezoelectric ceramic and a structural component. Under the assumption that the thickness of adhesive is relatively smaller than adherents, we develop both elastic and viscoelastic models to simulate the static and transient behaviors of the load transfer design. We also conduct finite element analysis to verify the results of the theoretical model. Both theoretical predictions and FEM simulations show that the load transfer design with a conventional 0.5 mm thickness for adhesive achieves 40% of stress reduction factor for rubber solid based adhesive, or 90% of stress reduction factor for FM-73 based adhesive. In conclusion, the thicker and less relaxation modulus adhesive materials lead to more reduction factors.

Chapter 6 Conclusions

We proposed an SHM system composed of a drive unit electrically connected to a sensor unit by an interface circuit. The design components of this low-power and light weight SHM system were proposed and experimentally verified.

A piezoelectric ceramic based drive unit converts mechanical energy to electric energy that electrically fatigues the ferroelectric based (PZT thin film) sensor unit. We coupled mechanics of piezoelectric materials to an electric circuit equation as well as coupled the electric response to mechanical vibrations. By this electro-mechanical coupling effect, we modeled the dynamic output voltage of the drive unit. The four-point-bending fixtures approximated the case of most practical applications that stress distribution is uniformly distributed on the piezoelectric patches if the structural component is relatively larger and thicker than the piezoelectric patches. By conducting the four-point-bending tests, we demonstrated that the output voltage is proportional to the stress at a specific frequency. We also built up a finite element model to simulate the electrical output of the piezoelectric based drive unit, which shows agreement with the experimental results.

The ferroelectric based (PZT thin films) sensor unit was tested and its polarization fatigue nature makes it a good candidate for cycle counter devices with some modifications. We developed an automatic measurement system that is able to conduct millions of cycles of electric fatigue tests, and measured hysteresis loops and the corresponding remnant polarizations at a specific number of cycles. Using this automatic measurement system, we applied millions of cycles of electric field to electrically fatigue the PZT thin film. The results show that the driven electric field accelerates the polarization fatigue of the PZT film. To best use the electric fatigue behaviors of the PZT thin film, we pretrained the PZT thin film to make it pass through the plateau region and directly operate linearly in the sensor region.

An interface circuit was also proposed that makes the design of the SHM system more flexible and more accurately predict cycles of the loadings. The window comparator based interface circuit sends out a certain amplitude of pulse trains if the amplitude of stress on the structural component is larger than a specific value, called threshold stress. Therefore, the number of cycles of multiple stress levels can be recorded by multiple PZT thin films with a specific interface circuit designed for each PZT film. A two-PZT-film sensor unit with a drive unit was driven under a random amplitude of loadings and the performance of the proposed SHM system was verified.

To protect the fragile piezoelectric ceramic based drive unit, we propose a load transfer design. In this design, the piezoelectric patches are mounted on the structural component by a viscoelastic adhesive in between. The static and dynamic behaviors of the stress and strain distributions on the piezoelectric patch and stress/strain reduction factor were analyzed elastically as well as viscoelastically. Three dimensional finite element models were developed to verify the theoretical model, which show good agreement.

It has been verified that the weight of the SHM system is significantly reduced, which requires a low power and no memory system, but the system still performs reliable accuracy. Besides the research on core components of the SHM (the drive and sensor unit), the extended study on the theoretical model of electro-mechanical coupling effect of piezoelectric beam and the viscoelastic analysis on the load transfer design to protect the drive unit, was conducted as well. The proposed SHM provides a reliable candidate to monitor the amplitude and number of cycles of stress that a structural component undergone. The issues that have to be further investigated are the polarization fatigue under the variation of temperature and humidity.

Reference

[1] NTSB, Aircraft Accident Report -United Airlines Flight 232 McDonnel Douglas DC-10-10 Sioux Gateway Airport Sioux City Uowa July 19, 1989, 1990.

[2] ASC, In-flight structural breakup, Boeing 747-200 B18255, May 25, 2012 in the Taiwan Straits approximately 23nm northwest of Makung, Taipei, 2002.

[3] W.A.J. Albert, Uber Treibseile am Harz. Archiv ffir Mineralogie, Georgnosie, Bergbau Und Hiittenkd. 10 (1837) 215–234.

[4] A. Wohler, Uber die festigkeitversuche mit eisen und stahl, Zeitschrift Fur Bauwes. XX (1870) 73–106.

[5] J. Bauschinger, Uber die Veranderung der Elastizitatsgrenze und der Festigkeit des Eisens und Stahls durch Strecken und Quetschen, durch Erwarmen und Abkuhlen und durch oftmals wiederholte Beanspruchung, Mitt. Mech.-Tech. Lab. Miinch. 13 (1886) 1–115.

[6] A. Palmgren, Die Lebensdauer von Kugellagern, VDI-Zeitschrift. 68 (1924) 339–341.

[7] M.A. Miner, Cumulative damage in fatigue, J. Appl. Mech. 12 (1945) A159–A164.

[8] M. Matsuishi, T. Endo, Fatigue of metals subjected to varying stress, in: Japan Soc. Mech. Eng., Jukvoka, Japan, 1968.

[9] F.-K. Chang, Structural Health Monitoring: A Summary Report on the First Stanford Workshop on Structural Health Monitoring, September 18-20, 1997, in: Struct. Heal. Monit. A Summ. Rep. First Stanford Work. Struct. Heal. Monit. Sept. 18-20, 1997, 1997.

[10] D. Balageas, C.P. Fritzen, A. Guemes, Structure Health Monitoring, 2006.

[11] J.K. Vandiver, Detection of Structural Failure on Fixed Platforms by Measurement of Dynamic Response, J. Pet. Technol. XXIX (1977).

[12] A.K. Pandey, M. Biswas, M.M. Samman, Damage Detection from Changes in Curvatures Mode Shapes, J. Sound Vib. 145 (1991) 321–332.

[13] Y.K. Ho, D.J. Ewins, On the structural damage identification with mode shapes, in: Proc. Eur. COST F3 Conf. Syst. Identif. Struct. Heal. Monit., Universidad Politecnica de Madrid, Spain, 2000: pp. 677–684.

[14] S.W. Doebling, L.D. Peterson, K.F. Alvin, Estimation of reciprocal residual flexibility from experimental modal data, AIAA J. 34 (1996) 1678–1685. doi:10.2514/3.13289.

[15] M. Sanayei, a. Esfandiari, a. Rahai, F. Bakhtiari-Nejad, Quasi-linear sensitivity-based structural model updating using experimental transfer functions, Struct. Heal. Monit. 11 (2012) 656–670. doi:10.1177/1475921712451952.

[16] B. Xu, G. Song, S.F. Masri, Damage detection for a frame structure model using vibration displacement measurement, Struct. Heal. Monit. 11 (2012) 281–292. doi:10.1177/1475921711430437.

[17] Y.K. Ho, D.J. Ewins, On the structural damage identification with mode shapes, in: Proc. Eur. COST F3 Conf. Syst. Identif. Struct. Heal. Monit., Universidad Politecnica de Madrid, Spain, 2000: pp. 677–684.

[18] A.K. Pandey, M. Biswas, Damage detecton in structures using changes in flexibility, J. Sound Vib. 169 (1994) 3–17.

[19] J. Zhao, J.T. DeWolf, Sensitivity study for vibrational parameters used in damage detection, J. Struct. Eng. 125 (1999) 410–416.

[20] D. Bernal, B. Gunes, DAMAGE LOCALIZATION IN OUTPUT-ONLY SYSTEMS : A FLEXIBILITY BASED APPROACH, in: Proc. 20th Modal Anal. Conf., Los Angeles, 2002: pp. 1185–1191.

[21] D. Bernal, B. Gunes, A Flexibility Based Approach for the Localization and Quantification of Damage: Application in a Benchmark Structure, J. Eng. Mech. 130 (2004) 61–70.

[22] C.. Butter, G.B. Hocker, Fiber-optic strain gauge, Appl. Opt. 17 (1978) 2867–2869.

[23] G.B. Hocker, Fiber-optic sensing of pressure and temperature., Appl. Opt. 18 (1979) 1445–1448.

[24] M. LeBlanc, S.Y. Huang, R.M. Measures, Fiber optic Bragg intra-grating strain gradient sensing, in: Smart Struct. Mater. 1995 Smart Sensing, Process. Instrumentation; Proc. Meet. SPIE-2444, San Diego, CA, n.d. pp. 136–147.

[25] B. Glisic, Y. Yao, Fiber optic method for health assessment of pipelines subjected to earthquake-induced ground movement, Struct. Heal. Monit. 11 (2012) 696–711. doi:10.1177/1475921712455683.

[26] C.E. Davis, P. Norman, C. Ratcliffe, R. Crane, Broad area damage detection in composites using fibre Bragg grating arrays, Struct. Heal. Monit. 11 (2012) 724–732. doi:10.1177/1475921712455681.

[27] G.A. John, Surface Effectship vibro-impact monitoring with distributed arrays of fiber Bragg gratings, in: Proc. 18th Int. Modal Anal. Conf., San Antonio, TX, 2000.

[28] D.C. Betz, G. Thursby, B. Culshaw, W.J. Staszewski, Acousto-ultrasonic sensing using fiber Bragg gratings, Smart Mater. Struct. 12 (2003) 122–128. doi:10.1088/0964-1726/12/1/314.

[29] M. Fink, Time Reversal of Ultrasonic Fields-Part I: Basic Principles, IEEE Trans. Ultrason. Ferroelectr. Freq. Control. 39 (1992) 555–566.

[30] X. Lin, F.G. Yuan, Diagnostic Lamb waves in an integrated piezoelectric sensor / actuator plate: analytical and experimental studies, Smart Mater. Struct. 10 (2001) 907–913.

[31] V. Giurgiutiu, A.N. Zagrai, Characterization of Piezoelectric Wafer Active Sensors, J. Intell. Mater. Syst. Struct. 11 (2000) 959–975.

[32] C.H. Wang, J.T. Rose, F.-K. Chang, A synthetic time-reversal imaging method for structural health monitoring, Smart Mater. Struct. 13 (2004) 415–423. doi:10.1088/0964-1726/13/2/020.

[33] C.M. Yeum, H. Sohn, J.B. Ihn, Lamb wave mode decomposition using concentric ring and circular piezoelectric transducers, Wave Motion. 48 (2011) 358–370. doi:10.1016/j.wavemoti.2011.01.001.

[34] A.J. Dawson, J.E. Michaels, Lamb wave mode decomposition using annular transducers and quadrature signals, AIP Conf. Proc. 1511 (2013) 628–635. doi:10.1063/1.4789105.

[35] C. Liang, C.A. Rogers, Coupled Electro-Mechanical Analysis of Adaptive Material Systems — Determination of the Actuator Power Consumption and System Energy Transfer, J. Intell. Mater. Syst. Struct. 5 (1994) 12–20.

[36] F. Sun, C.A. Robers, C. Liang, Structural frequency response function acquisition via electric impedance measurement of surface-bonded piezoelectric sensor/actuator, in: Proceeding AIAA/ASME/ASCE/AHS/ASC Struct. Struct. Dyn. Mater. Conf., New Orleans, LA, 1995: pp. 3450–3461.

[37] F. Sun, C.A. Robers, C. Liang, Structural frequency response function acquisition via electric impedance measurement of surface-bonded piezoelectric sensor/actuator, in: Proceeding AIAA/ASME/ASCE/AHS/ASC Struct. Struct. Dyn. Mater. Conf., New Orleans, LA, 1995: pp. 3450–3461.

[38] Z. Chaudhry, F. Lalande, F. Ganino, C.A. Rogers, J. Chung, Monitoring the Integrity of Composite Patch Structural Repair via Piezoelectric Actuators/Sensors, in: Proceesings AIAAASME/ASCE/AHS/ASC 36th Struct. Struct. Struct. Dyn. Mater. Conf. Adapt. Struct. Forum, New Orleans, LA, 1995: pp. 2243–2248.

[39] G. Park, H.C. Harley, D.J. Inman, Impedance-Based Health Monitoring of Civil Structural Components, J. Infrastruct. Syst. 6 (2000) 153–160.

[40] Y. Yang, Y. Hu, Y. Lu, Sensitivity of PZT Impedance Sensors for Damage Detection of Concrete Structures, Sensors. 8 (2008) 327–346.

[41] G. Park, H.H. Cudney, D.J. Inman, An Integrated Health Monitoring Technique Using Structural Impedance Sensors, J. Intell. Mater. Syst. Struct. 11 (2000) 448–455. doi:10.1106/QXMV-R3GC-VXXG-W3AQ.

[42] G. Park, H. Sohn, C.R. Farrar, D.J. Inman, Overview of Piezoelectric Impedance-Based Health Monitoring and Path Forward, Shock Vib. Dig. 35 (2003) 451–463. doi:10.1177/05831024030356001.

[43] D.M. Pecairs, G. Park, D.J. Inman, Improving Accessibility of the Impedance-Based Structural Health Monitoring Method, J. Intell. Mater. Syst. Struct. 15 (2004) 129–139. doi:10.1177/1045389X04039914.

[44] G. Park, A.C. Rutherford, H. Sohn, C.R. Farrar, An outlier analysis framework for impedance-based structural health monitoring, J. Sound Vib. 286 (2005) 229–250. doi:10.1016/j.jsv.2004.10.013.

[45] C. Wakabayashi, H. Sato, M. Taya, Design of a new structural health monitoring based on piezoelectric sensors for detection of strain of various amplitudes, in: M.J. Dapino, Z. Ounaies (Eds.), Behav. Mech. Multifunct. Compos. Mater. Proc. SPIE 6929, San Diego, CA, 2008: p. 69290I–69290I–7. doi:10.1117/12.778524.

[46] Y.Y. Lin, M. Taya, J.B. Ihn, Design of a Self-Powered Load Monitoring System for Hot Spot application, in: F.-K. Chang (Ed.), Proc. 8th Int. Work. Struct. Heal. Monit., Stanford, 2011: pp. 333–342.

[47] W.G. Cady, Piezoelectricity, Dover Publication, Inc, New York, 1964.

[48] C.B. William, R.B. Yates, Analysis of a micro-electric generator for microsystems, Sensors Actuators A Phys. 52 (1996) 8–11.

[49] V.P. Generation, R. Amirtharajah, A.P. Chandrakasan, Self-Powered Signal Processing Using, 33 (1998) 687–695.

[50] P. Glynne-Jones, S.P. Beeby, N.M. White, Towards a piezoelectric vibration-powered microgenerator, IEE Proc. - Sci. Meas. Technol. 148 (2001) 68. doi:10.1049/ip-smt:20010323.

[51] S. Roundy, P.K. Wright, J. Rabaey, A study of low level vibrations as a power source for wireless sensor nodes, Comput. Commun. 26 (2003) 1131–1144. doi:10.1016/S0140-3664(02)00248-7.

[52] ANSI/IEEE Standard 176, Piezoelectricity, (1987).

[53] N.E. Dutoit, B.L. Wardle, S.-G. Kim, Design Considerations for Mems-Scale Piezoelectric Mechanical Vibration Energy Harvesters, Integr. Ferroelectr. 71 (2005) 121–160. doi:10.1080/10584580590964574.

[54] F. Lu, H.P. Lee, S.P. Lim, Modeling and analysis of micro piezoelectric power generators for micro-electromechanical-systems applications, Smart Mater. Struct. 13 (2004) 57–63. doi:10.1088/0964-1726/13/1/007.

[55] a Erturk, D.J. Inman, Issues in mathematical modeling of piezoelectric energy harvesters, Smart Mater. Struct. 17 (2008) 065016. doi:10.1088/0964-1726/17/6/065016.

[56] A. Erturk, D.J. Inman, A Distributed Parameter Electromechanical Model for Cantilevered Piezoelectric Energy Harvesters, J. Vib. Acoust. 130 (2008) 041002. doi:10.1115/1.2890402.

[57] a Erturk, D.J. Inman, An Experimentally Validated Bimorph Cantilever Model for Piezoelectric Energy Harvesting from Base Excitations, Smart Mater. Struct. 18 (2009) 025009. doi:10.1088/0964-1726/18/2/025009.

[58] H.F. Tiersten, Linear Piezoelectric Plate Vibrations, Plenum Press, New York, 1969.

[59] S.R. Anton, H. a Sodano, A Review of Power Harvesting Using Piezoelectric Materials (2003–2006), Smart Mater. Struct. 16 (2007) R1–R21. doi:10.1088/0964-1726/16/3/R01.

[60] a. Erturk, D.J. Inman, On Mechanical Modeling of Cantilevered Piezoelectric Vibration Energy Harvesters, J. Intell. Mater. Syst. Struct. 19 (2008) 1311–1325. doi:10.1177/1045389X07085639.

[61] K.F. Graff, Wave Motion in Elastic Solids, Dover Publication, Inc, New York, 1975.

[62] D.J. Griffiths, Introduction to Electridynamics, 3rd ed., Addison-Wesley, Upper Saddle River, New Jersey, 1999.

[63] L. Meirovitch, Principles and Techniques of Vibrations, Prentice Hall, Upper Saddle River, New Jersey, 1996.

[64] J. Valasek, Piezo-Electric and Allied Phenomena in Rochelle Salt, Phys. Rev. 17 (1921) 475–481.

[65] J. Anderson, M. Merz, Ferroelectric Storage Devices, Bell Lab. Rep. 33 (1955) 335–337, 339–342.

[66] T. Mihara, H. Watanabe, C.A.P. de Araujo, Polarization Fatigue Characteristics of Sol-Gel Ferroelectric Pb (Zr 0 . 4 Ti 0 . 6) O 3 Thin-Film Capacitors, Jpn. J. Appl. Phys. 33 (1994) 1996–4002.

[67] M. Grossmann, D. Bolten, O. Lohse, U. Boettger, R. Waser, S. Tiedke, Correlation between switching and fatigue in PbZr[sub 0.3]Ti[sub 0.7]O[sub 3] thin films, Appl. Phys. Lett. 77 (2000) 1894. doi:10.1063/1.1290154.

[68] B.G. Chae, C.H. Park, Y.S. Yang, M.S. Jang, Asymmetry in fatigue and recovery in ferroelectric Pb(Zr,Ti)O[sub 3] thin-film capacitors, Appl. Phys. Lett. 75 (1999) 2135. doi:10.1063/1.124941.

[69] K. Amanuma, T. Hase, Y. Miyasaka, Fatigue Characteristics of Sol-Gel Derived Pb (Zr , Ti) O 3 Thin Films, Jpn. J. Appl. Phys. 33 (1994) 5211–5214.

[70] P.J. Schorn, D. Bräuhaus, U. Böttger, R. Waser, G. Beitel, N. Nagel, et al., Fatigue effect in ferroelectric PbZr[sub 1−x]Ti[sub x]O[sub 3] thin films, J. Appl. Phys. 99 (2006) 114104. doi:10.1063/1.2200470.

[71] P.K. Larsen, G.J.M. Dormans, D.J. Taylor, P.J. van Veldhoven, Ferroelectric properties and fatigue of PbZr0.51Ti0.49O3 thin films of varying thickness: Blocking layer model, J. Appl. Phys. 76 (1994) 2405. doi:10.1063/1.357589.

[72] K. Tominaga, A. Shirayanagi, T. Takagi, M. Okada, Switching and Fatigue Characteristics of (Pb , La)(Zr , Ti) O3 Thin Films by Metalorganic Chemical Vapor Deposition, Jpn. J. Appl. Phys. 32 (1993) 4082–4085.

[73] E.L. Colla, A.K. Tagantsev, A.L. Kholkin, N. Setter, DC-voltage and cycling induced recovery of switched polarisation in fatigued ferroelectric thin films, Integr. Ferroelectr. 10 (1995) 289–294.

[74] C. Pawlaczyk, A.K. Tagantsev, K. Brooks, I.M. Reaney, Fatigue, rejuvenation and self-restoring in ferroelectric thin films, Integr. Ferroelectr. 9 (1995) 293–316.

[75] A. Morimoto, Y. Yamanaka, T. Shimizu, Fatigue Behavior in Lead-Zirconate-Titanate Thin-Film Capacitors Prepared by Pulsed Laser Ablation on Ni-Alloy Electrodes, Jpn. J. Appl. Phys. 34 (1995) 4108–4113.

[76] R. Ramesh, W.K. Chan, B. Wilkens, T. Sands, J.M. Tarascona, V.G. Keramidasa, et al., Fatigue and aging in ferroelectric PbZr0.2Ti0.8O3/YBa2Cu3O7 heterostructures, Integr. Ferroelectr. 1 (1992) 1–15.

[77] K. Lee, B.R. Rhee, C. Lee, Characteristics of ferroelectric Pb(Zr,Ti)O[sub 3] thin films having Pt/PtO[sub x] electrode barriers, Appl. Phys. Lett. 79 (2001) 821. doi:10.1063/1.1391226.

[78] S.B. Majumder, Y.N. Mohapatra, D.C. Agrawal, Fatigue resistance in lead zirconate titanate thin ferroelectric films: Effect of cerium doping and frequency dependence, Appl. Phys. Lett. 70 (1997) 138. doi:10.1063/1.119287.

[79] H.N. Al-Shareef, O. Auciello, A.I. Kingon, Electrical properties of ferroelectric thin-film capacitors with hybrid (Pt,RuO2) electrodes for nonvolatile memory applications, J. Appl. Phys. 77 (1995) 2146–2154. doi:10.1063/1.359572.

[80] W.L. Warren, D. Dimos, B. a. Tuttle, G.E. Pike, R.W. Schwartz, P.J. Clews, et al., Polarization suppression in Pb(Zr,Ti)O3 thin films, J. Appl. Phys. 77 (1995) 6695. doi:10.1063/1.359083.

[81] D. Dimos, H.N. Al-Shareef, W.L. Warren, B. a. Tuttle, Photoinduced changes in the fatigue behavior of SrBi2Ta2O9 and Pb(Zr,Ti)O3 thin films, J. Appl. Phys. 80 (1996) 1682. doi:10.1063/1.362968.

[82] W.L. Warren, D. Dimos, B.A. Tuttle, G.E. Pike, H.N. Al-shareef, Relationships among ferroelectric fatigue, electronic charge trapping, defect-dipoles, and oxygen vacancies in perovskite oxide, Integr. Ferroelectr. 16 (1997) 77–86.

[83] C.H. Park, D.J. Chadi, Microscoptic study of oxygen-vacancy defects in ferroelectric perovskites, Phys. Rev. B Condens. MATTER Mater. Phys. 57 (1998) 961–964.

[84] Q. Jiang, W. Cao, I.E. Cross, Electric Fatigue in Lead Zirconate Titanate Ceramics, J. Am. Ceram. Soc. 77 (1994) 211–215.

[85] M.D. Hill, G.S. White, C.-S. Hwang, Cyclic Damage in Lead Zirconate Titanate, J. Am. Ceram. Soc. 79 (1996) 1915–1920.

[86] C.B. Sawyer, C.H. Tower, Rochelle Salt as a Dielectric, Phys. Rev. 35 (1930). doi:http://dx.doi.org/10.1103/PhysRev.35.269.

[87] L.B. Freund, S. Suresh, Thin Film Materials, Cambridge University Press, New Yok, 2003.

[88] G. Stoney, The tension of metallic films deposited by electrolysis, Proc. R. Soc. London. Ser. A. (1909) 172–175.

[89] H.L. Cox, The elasticity and strength of paper and other fibrous materials, Br. J. Appl. Phisics. 72 (1951) 72–79.

[90] M. Yanaka, Y. Tsukahara, N. Nakaso, Cracking phenomena of brittle films in nanostructure composites analysed by a modified shear lag model with residual strain, J. Mater. Sci. 33 (1998) 2111–2119.

[91] P.H. Townsend, D.M. Barnett, T. a. Brunner, Elastic relationships in layered composite media with approximation for the case of thin films on a thick substrate, J. Appl. Phys. 62 (1987) 4438. doi:10.1063/1.339082.

[92] K.P. Wang, Y.Y. Huang, A. Chandra, K.X. Hu, Interfacial shear stress, peeling stress, and die cracking stress in trilayer electronic assemblies, IEEE Trans. Components Packag. Technol. 23 (2000) 309–316. doi:10.1109/6144.846769.

[93] O. VOLKERSEN, Die Nietkraftverteilung in zugbeanspruchten Nietverbindungen mit konstanten Laschenquerschnitten, Luftfahrtsforschung. 15 (1938) 41–47.

[94] M. GOLAND, E. REISSNER, The Stresses in Cemented Joints, J. Appl. Mech. 66 (1944) A17–A27.

[95] O. VOLKERSEN, Die Nietkraftverteilung in zugbeanspruchten Nietverbindungen mit konstanten Laschenquerschnitten, Luftfahrtsforschung. 15 (1938) 41–47.

[96] M. GOLAND, E. REISSNER, The Stresses in Cemented Joints, J. Appl. Mech. 66 (1944) A17–A27.

[97] E. Lubkin, J.L. Reisssner, Stress distribution and design data for adhesive lap joints between circular tubes, Trans. ASME. 78 (1956) 1213–1221.

[98] R.D. Adams, N.A. Peppiatt, Stress analysis of bonded tubular lap joints, J. Adhes. 9 (1977) 1–18.

[99] O. Nemeş, F. Lachaud, a. Mojtabi, Contribution to the study of cylindrical adhesive joining, Int. J. Adhes. Adhes. 26 (2006) 474–480. doi:10.1016/j.ijadhadh.2005.07.009.

[100] I.U. Ojalvo, H.L. Eidinoff, Bond Thickness Effects upon Stresses in Single-Lap Adhesive Joints, AIAA J. 16 (1978) 204–211.

[101] M.Y. Tsai, D.W. Oplinger, J. Morton, and J. MORTON, Int. J. Solids Struct. 35 (1998) 1163–1185.

[102] I.U. Ojalvo, H.L. Eidinoff, Bond Thickness Effects upon Stresses in Single-Lap Adhesive Joints, AIAA J. 16 (1978) 204–211.

[103] M.Y. Tsai, D.W. Oplinger, J. Morton, and J. MORTON, Int. J. Solids Struct. 35 (1998) 1163–1185.

[104] Y.R. Nagaraja, R.S. Alwar, Viscoelastic Analysis of an Adhesive-Bonded Plane Lap Joint, Comput. Struct. 11 (1980) 621–627.

[105] F. Delale, F. Erdogan, Viscoelastic Analysis of Adhesively Bonded Joints, J. Appl. Mech. 42 (1981) 331–338.

[106] K.N.J. Morman, The generalized strain measure with application to nonhomogeneous deformations in rubber-like solids, J. Appl. Mech. 53 (1986) 726–728.

[107] F. Cheng, Ö.Ö. Özsoy, J.N. Reddy, Finite Element Modeling of Viscoelastic Behavior and Interface Damage in Adhesively Bonded Joints, in: S. Kumar, K.L. Mittal (Eds.), Adv. Model. Des. Adhes. Bond. Syst., Wiley-Scrivener, Hoboken, NJ, 2013: pp. 23–44.

[108] S. Roy, J.N. Reddy, Nonlinear Viscoelastic Finite Element Analysis of Adhesive Joints, Tire Sci. Technol. 16 (1988) 146–170.

Appendix

Appendix I APDL script – FEM model of beam in four-point-bending fixture

```
FINISH
/CLEAR
/PREP7

! Parameterize dimensions,
! material constants, etc
! Dimensions of beam
beamLength = 15E-2
beamHeight = 1E-3
beamWidth = 5E-2

! Dimensions of piezoelectric
! plate
piezoLength = 5E-2
piezoHeight =0.5E-3
piezoWidth = 1.0E-2
Gap = 0.5E-2

! Positions of BCs
fixtureSpan1 = 10E-2
fixtureSpan2 = 7.5E-2

! PZT IS Polarized in the Y
! direction
! Compliance matrix
SE11=  16.4e-12
SE12= -5.74e-12
SE13= -7.22e-12
SE21= SE12
SE22= SE11
SE23= SE13
SE32= SE23
SE33= 18.8e-12
SE44= 47.5e-12
SE55= 44.3e-12
SE66= SE55

! Permittivity matrix
FREE=8.854E-12   !Free-space
permittivity
REPS11=2270
REPS33=2130

D13=-210E-12
D33=472E-12
D23=D13
D51=758E-12
D42=D51

! Material density of PZT
DSTYPZT=7650

C0=20.4E-9*3
R0=18.5E6/3
ZL=1E6

! Define coordinate system for
! poling direction
LOCAL,11
LOCAL,12,,,,,180
! End of Parameterize dimensions,
! material constants, etc



! Element Types
ET,101,SHELL63   !Dummy ET 101
R,101,1
alumETID = 1
piezoETID = 2

ET, alumETID, SOLID186
      ! for aluminum beam
ET, piezoETID, SOLID226,1001
      ! for piezoelectric material
! End of Element Types


! Material Properties
piezoMatID = 1
alumMatID = 2


! Material No.1 - PZT
MP,DENS,piezoMatID,DSTYPZT
MP,PRXY,piezoMatID,0.32
MP,PRYZ,piezoMatID,0.32
MP,PRXZ,piezoMatID,0.32

TB,ANEL,piezoMatID,1,,1
TBDATA, 1,SE11,SE13,SE12
TBDATA, 7,SE33,SE32
TBDATA,12,SE22
TBDATA,16,SE55
TBDATA,19,SE44
TBDATA,21,SE66

TB,PIEZ,piezoMatID,,,1
TBDA,1,0,D13,0,0,D33,0
TBDA,7,0,D23,0,D51,0,0
TBDA,13,0,0,D42,0,0,0
```

```
EMUNIT,EPZRO,FREE
MP,PERX,piezoMatID ,REPS11
MP,PERY,piezoMatID ,REPS11
MP,PERZ,piezoMatID ,REPS33

! Material for aluminum
MP,EX,alumMatID,69E9
MP,PRXY,alumMatID,0.3
MP,DENS,alumMatID,2700

! Material No.101 for areas
MP,EX,101,5408          !Dummy MAT
101
MP,PRXY,101,0.3
! End of Material Properties

! Create Solid models and FEM
! models
CSYS,11
! Create keypoints
K,1,-beamLength/2,0,beamWidth/2
K,2,-fixtureSpan1/2,0,beamWidth/2
K,3,-fixtureSpan2/2,0,beamWidth/2
K,4,-piezoLength/2,0,beamWidth/2
K,5,piezoLength/2,0,beamWidth/2
K,6,fixtureSpan2/2,0,beamWidth/2
K,7,fixtureSpan1/2,0,beamWidth/2
K,8,beamLength/2,0,beamWidth/2

K,9,-
beamLength/2,0,piezoWidth/2+Gap+pi
ezoWidth
K,10,-
fixtureSpan1/2,0,piezoWidth/2+Gap+
piezoWidth
K,11,-
fixtureSpan2/2,0,piezoWidth/2+Gap+
piezoWidth
K,12,-
piezoLength/2,0,piezoWidth/2+Gap+p
iezoWidth
K,13,piezoLength/2,0,piezoWidth/2+
Gap+piezoWidth
K,14,fixtureSpan2/2,0,piezoWidth/2
+Gap+piezoWidth
K,15,fixtureSpan1/2,0,piezoWidth/2
+Gap+piezoWidth
K,16,beamLength/2,0,piezoWidth/2+G
ap+piezoWidth

K,17,-
beamLength/2,0,piezoWidth/2+Gap
K,18,-
fixtureSpan1/2,0,piezoWidth/2+Gap
K,19,-
fixtureSpan2/2,0,piezoWidth/2+Gap
K,20,-
piezoLength/2,0,piezoWidth/2+Gap
K,21,piezoLength/2,0,piezoWidth/2+
Gap
K,22,fixtureSpan2/2,0,piezoWidth/2
+Gap
K,23,fixtureSpan1/2,0,piezoWidth/2
+Gap
K,24,beamLength/2,0,piezoWidth/2+G
ap

K,25,-beamLength/2,0,piezoWidth/2
K,26,-
fixtureSpan1/2,0,piezoWidth/2
K,27,-
fixtureSpan2/2,0,piezoWidth/2
K,28,-piezoLength/2,0,piezoWidth/2
K,29,piezoLength/2,0,piezoWidth/2
K,30,fixtureSpan2/2,0,piezoWidth/2
K,31,fixtureSpan1/2,0,piezoWidth/2
K,32,beamLength/2,0,piezoWidth/2

K,33,-beamLength/2,0,-piezoWidth/2
K,34,-fixtureSpan1/2,0,-
piezoWidth/2
K,35,-fixtureSpan2/2,0,-
piezoWidth/2
K,36,-piezoLength/2,0,-
piezoWidth/2
K,37,piezoLength/2,0,-piezoWidth/2
K,38,fixtureSpan2/2,0,-
piezoWidth/2
K,39,fixtureSpan1/2,0,-
piezoWidth/2
K,40,beamLength/2,0,-piezoWidth/2

K,41,-beamLength/2,0,-
piezoWidth/2-Gap
K,42,-fixtureSpan1/2,0,-
piezoWidth/2-Gap
K,43,-fixtureSpan2/2,0,-
piezoWidth/2-Gap
K,44,-piezoLength/2,0,-
piezoWidth/2-Gap
K,45,piezoLength/2,0,-
piezoWidth/2-Gap
K,46,fixtureSpan2/2,0,-
piezoWidth/2-Gap
K,47,fixtureSpan1/2,0,-
piezoWidth/2-Gap
K,48,beamLength/2,0,-piezoWidth/2-
Gap
```

```
K,49,-beamLength/2,0,-piezoWidth/2-Gap-piezoWidth
K,50,-fixtureSpan1/2,0,-piezoWidth/2-Gap-piezoWidth
K,51,-fixtureSpan2/2,0,-piezoWidth/2-Gap-piezoWidth
K,52,-piezoLength/2,0,-piezoWidth/2-Gap-piezoWidth
K,53,piezoLength/2,0,-piezoWidth/2-Gap-piezoWidth
K,54,fixtureSpan2/2,0,-piezoWidth/2-Gap-piezoWidth
K,55,fixtureSpan1/2,0,-piezoWidth/2-Gap-piezoWidth
K,56,beamLength/2,0,-piezoWidth/2-Gap-piezoWidth

K,57,-beamLength/2,0,-beamWidth/2
K,58,-fixtureSpan1/2,0,-beamWidth/2
K,59,-fixtureSpan2/2,0,-beamWidth/2
K,60,-piezoLength/2,0,-beamWidth/2
K,61,piezoLength/2,0,-beamWidth/2
K,62,fixtureSpan2/2,0,-beamWidth/2
K,63,fixtureSpan1/2,0,-beamWidth/2
K,64,beamLength/2,0,-beamWidth/2

! Create areas for extrusion
I=0
*DO,I,1,7
      A,I,I+1,I+9,I+8
*ENDDO

I=0
*DO,I,9,15
      A,I,I+1,I+9,I+8
*ENDDO

I=0
*DO,I,17,23
      A,I,I+1,I+9,I+8
*ENDDO
I=0
*DO,I,25,31
      A,I,I+1,I+9,I+8
*ENDDO

I=0
*DO,I,33,39
      A,I,I+1,I+9,I+8
*ENDDO
I=0
*DO,I,41,47
      A,I,I+1,I+9,I+8
*ENDDO

I=0
*DO,I,49,55
      A,I,I+1,I+9,I+8
*ENDDO
AGLUE,ALL

! mesh areas
LSEL,ALL
LSEL,S,TAN1,Z,0
LESIZE,ALL,piezoLength/24

LSEL,ALL
LSEL,S,TAN1,X,0
LESIZE,ALL,Gap/4,,

! mesh attribute
ASEL,ALL
AATT,101,101,101
MSHAPE,0,2D
MSHKEY,1
AMESH,ALL

! extrude aluminum structure
ASEL,S,LOC,Y,0
ESIZE,,4
VEXT,ALL,,,,beamHeight,
ALLSEL,ALL

! Create area components to extrude piezoelectric plates
ASEL,S,LOC,Y,beamHeight,beamHeight
ASEL,R,LOC,X,-piezoLength/2,piezoLength/2
ASEL,R,LOC,Z,-piezoWidth/2-Gap-piezoWidth,-piezoWidth/2-Gap
CM,PIEZOAREA1,AREA

ASEL,S,LOC,Y,beamHeight,beamHeight
ASEL,R,LOC,X,-piezoLength/2,piezoLength/2
ASEL,R,LOC,Z,-piezoWidth/2,piezoWidth/2
CM,PIEZOAREA2,AREA

ASEL,S,LOC,Y,beamHeight,beamHeight
ASEL,R,LOC,X,-piezoLength/2,piezoLength/2
ASEL,R,LOC,Z,piezoWidth/2+Gap,piezoWidth/2+Gap+piezoWidth
```

```
CM,PIEZOAREA3,AREA

! Select area components for
! piezoelectric plate and extude
CMSEL,S,PIEZOAREA1
CMSEL,A,PIEZOAREA2
CMSEL,A,PIEZOAREA3
ESIZE,,4
VEXT,ALL,,,,piezoHeight,
ACLEAR,ALL
ALLSEL,ALL
! End of Create Solid models and
! FEM models


! circuit
N,100002,0,-piezoLength/2,0
N,100003,0,-piezoLength,0
N,100004,0,-3*piezoLength/2,0

ET,3,CIRCU94,2
R,2,C0
! Real Const = 2 initial
capacitance
TYPE,3
REAL,2
E,NODE(0,beamHeight+piezoHeight,0)
,NODE(0,-piezoLength/2,0)

ET,4,CIRCU94,0
R,1,R0
TYPE,4
REAL,1
E,NODE(0,-
piezoLength/2,0),NODE(0,-
piezoLength,0)

ET,5,CIRCU94,0
R,1,ZL
TYPE,5
REAL,1
E,NODE(0,-piezoLength,0),NODE(0,-
3*piezoLength/2,0)


D,NODE(0,-
3*piezoLength/2,0),VOLT,0
! End of circuit

! Create Volume CoMponents
! Create volume component for
! aluminum structure
VSEL,S,LOC,Y,0,beamHeight
VSEL,R,LOC,X,-
beamLength/2,beamLength/2
CM,BEAMVOLU,VOLU

! Create volume components for
three piezoelectric plates
VSEL,S,LOC,Y,beamHeight,beamHeight
+piezoHeight
VSEL,R,LOC,X,-
piezoLength/2,piezoLength/2
VSEL,R,LOC,Z,-piezoWidth/2-Gap-
piezoWidth,-piezoWidth/2-Gap
CM,PIEZOVOLU1,VOLU

VSEL,S,LOC,Y,beamHeight,beamHeight
+piezoHeight
VSEL,R,LOC,X,-
piezoLength/2,piezoLength/2
VSEL,R,LOC,Z,-
piezoWidth/2,piezoWidth/2
CM,PIEZOVOLU2,VOLU

VSEL,S,LOC,Y,beamHeight,beamHeight
+piezoHeight
VSEL,R,LOC,X,-
piezoLength/2,piezoLength/2
VSEL,R,LOC,Z,piezoWidth/2+Gap,piez
oWidth/2+Gap+piezoWidth
CM,PIEZOVOLU3,VOLU
! End of Create Volume CoMponents

! Modify element types
! modify correct mat and type for
! piezoelectric plates
CMSEL,S,PIEZOVOLU1
CMSEL,A,PIEZOVOLU2
CMSEL,A,PIEZOVOLU3
ESLV,S
EMODIF,ALL,MAT,piezoMatID
EMODIF,ALL,TYPE,piezoETID
EMODIF,ALL,ESYS,12

! modify correct mat and type for
! aluminum structure
CMSEL,S,BEAMVOLU
ESLV,S
EMODIF,ALL,MAT,alumMatID
EMODIF,ALL,TYPE,alumETID
! End of modify element types

! Couple
! couple voltage DOF for top
! electrode
CMSEL,S,PIEZOVOLU1
```

```
CMSEL,A,PIEZOVOLU2
CMSEL,A,PIEZOVOLU3
ASEL,S,EXT
ASEL,R,LOC,Y,beamHeight+piezoHeight
NSLA,S,1
CM,Top_ELECTRODE,NODE
CP,1,VOLT,ALL
n_supply=ndnext(0)
NSEL,ALL

! couple voltage DOF for bottom
! electrode
CMSEL,S,PIEZOVOLU1
CMSEL,A,PIEZOVOLU2
CMSEL,A,PIEZOVOLU3
ASEL,S,EXT
ASEL,R,LOC,Y,beamHeight
CM,BOTTOM_ELECTRODE,NODE
NSLA,S,1
CP,2,VOLT,ALL
n_ground=ndnext(0)
NSEL,ALL

! couple UY DOF for fixture span 2
CMSEL,S,BEAMVOLU
ASEL,S,EXT
NSLA,S,1
NSEL,S,LOC,X,-fixtureSpan2/2
NSEL,A,LOC,X,fixtureSpan2/2
NSEL,R,LOC,Y,0
CM,LOADINGS,NODE
CP,3,UY,ALL
n_load=ndnext(0)
NSEL,ALL
! End of Couple DOF
```

Appendix II APDL script – Modal Analysis of beam in four-point-bending fixture

```
/SOLU
ANTYPE,MODAL
MODOPT,LANB,6
MXPAND,6
ALPHAD,0,
BETAD,0,
DMPRAT,0.0005,   ! damping ratio

! Electrical and Mechanical BCs
! Ground the bottom electrode
D,n_ground,VOLT,0

! BCs -- Symmetric about x axis
NSEL,S,LOC,X,0
D,ALL,UX,0
NSEL,ALL

! BCs -- Symmetric about z axis
NSEL,S,LOC,Z,0
D,ALL,UZ,0
NSEL,ALL

! BCs -- Left constrained of four-
! point-bending fixture
CMSEL,S,BEAMVOLU
ASEL,S,EXT
NSLA,S,1
NSEL,R,LOC,Y,0
NSEL,R,LOC,X,-fixtureSpan1/2
D,ALL,UY,0
NSEL,ALL

! BCs -- Right constrained of
! four-point-bending fixture
CMSEL,S,BEAMVOLU
ASEL,S,EXT
NSLA,S,1
NSEL,R,LOC,Y,0
NSEL,R,LOC,X,fixtureSpan1/2
D,ALL,UY,0
NSEL,ALL
! End of Electrical and Mechanical
! BCs

SOLVE
FINISH

/POST1
SET,LIST

/VIEW,1,1,1,1
/ANGLE,1

SET,FIRST
PLDISP,2

SET,NEXT
PLDISP,2
```

Appendix III APDL script – Harmonic response of drive unit in four-point-bending fixture

```
/SOLU
ANTYPE,HARMIC
TRNOPT,FULL
NLGEOM,ON
SSTIF,ON

ACEL,,,9.81
HARFRQ,0,1000,
NSUBST,100,
KBC,1
ALPHAD,0,
BETAD,0,
DMPRAT,0.0005,   ! damping ratio

! Electrical and Mechanical BCs
! Ground the bottom electrode
D,n_ground,VOLT,0

! BCs -- Symmetric about x axis
NSEL,S,LOC,X,0
D,ALL,UX,0
NSEL,ALL

! BCs -- Symmetric about z axis
NSEL,S,LOC,Z,0
D,ALL,UZ,0
NSEL,ALL

! BCs -- Left constrained of four-point-bending fixture
CMSEL,S,BEAMVOLU
ASEL,S,EXT
NSLA,S,1
NSEL,R,LOC,Y,0
NSEL,R,LOC,X,-fixtureSpan1/2
D,ALL,UY,0
NSEL,ALL

! BCs -- Right constrained of four-point-bending fixture
CMSEL,S,BEAMVOLU
ASEL,S,EXT
NSLA,S,1
NSEL,R,LOC,Y,0
NSEL,R,LOC,X,fixtureSpan1/2
D,ALL,UY,0
NSEL,ALL
! End of Electrical and Mechanical
! BCs
! Harmonic excitations

! === Create Marco
FORCEY=10
F,n_load,FY,FORCEY
! End of Marco

ALLSEL,ALL
SOLVE
FINISH

/POST26
NUMVAR,200
SOLU,200,NCMIT
STORE,MERGE
FILLDATA,200,,,,1,1
REALVAR,200,200

NSOL,2,NODE(0,beamHeight+piezoHeight,0),U,Y,DispY
STORE,MERGE

NSOL,3,NODE(0,beamHeight+piezoHeight,0),VOLT,,VoltP
STORE,MERGE

ANSOL,4,NODE(0,beamHeight+piezoHeight,0),S,X,StresX
STORE,MERGE

NSOL,5,NODE(0,-2*piezoLength/3,0),VOLT,,VoltL
STORE,MERGE

XVAR,1      ! 1: FREQ
PLVAR,2,    ! 2: UY

XVAR,1      ! 1: FREQ
PLVAR,3,    ! 3: Voltage

XVAR,1      ! 1: FREQ
PLVAR,4,    ! 4: Stress

XVAR,1      ! 1: FREQ
PLVAR,5,    ! 5: Stress
```

Appendix IV APDL script – Transient response of drive unit in four-point-bending fixture

```
/SOLU
ANTYPE,TRANS
TRNOPT,FULL
NLGEOM,ON
SSTIF,ON
ACEL,,-9.81,

ALPHAD,0,
BETAD,0,
DMPRAT,0 !0.0005,      ! damping
ratio

! Electrical and Mechanical BCs
! Ground the bottom electrode
D,n_ground,VOLT,0

! BCs -- Symmetric about x axis
NSEL,S,LOC,X,0
D,ALL,UX,0
NSEL,ALL

! BCs -- Symmetric about z axis
NSEL,S,LOC,Z,0
D,ALL,UZ,0
NSEL,ALL

! BCs -- Left constrained of four-
point-bending fixture
CMSEL,S,BEAMVOLU
ASEL,S,EXT
NSLA,S,1
NSEL,R,LOC,Y,0
NSEL,R,LOC,X,-fixtureSpan1/2
D,ALL,UY,0
NSEL,ALL

! BCs -- Right constrained of
four-point-bending fixture
CMSEL,S,BEAMVOLU
ASEL,S,EXT
NSLA,S,1
NSEL,R,LOC,Y,0
NSEL,R,LOC,X,fixtureSpan1/2
D,ALL,UY,0
NSEL,ALL
! End of Electrical and Mechanical
! BCs ========== !

! Sinusoidal excitations
freq = 1
! frequency of the sine wave
pi = ASIN(1)
dispamp = 1E-
3*0.6**(20/68)*(8/6)*(8/38)
! amplitude of the sine
!wave/((2*pi*freq)^2)

T=1E-8
C=0
N=500
COUNTER=4*1/N
! 2*pi/N
! Create Marco

*CREATE,LOAD
TIME,T

! Func. of Displacement
DISP=dispamp*SIN(2*pi*freq*T)

! Apply displacement loadings
!CMSEL,S,LOADINGS
D,n_load,UY,DISP

T=T+COUNTER
C=C+1
OUTRES,ALL
ALLSEL,ALL
SOLVE
*END
! End of Marco

! Active Macro with DO-ENDDO LOOP
*DO,I,1,N+1
 *USE,LOAD
*ENDDO
! End of Sinusoidal excitations

/POST26
!FILE,'SpringAPDL','rst','.'
!/UI,COLL,1
NUMVAR,200
SOLU,200,NCMIT
STORE,MERGE
FILLDATA,200,,,,1,1
REALVAR,200,200

NSOL,2,NODE(0,beamHeight+piezoHeig
ht,0),U,Y,DispY
STORE,MERGE
```

```
NSOL,3,NODE(0,beamHeight+piezoHeig
ht,0),VOLT,,VoltP
STORE,MERGE
NSOL,4,NODE(0,beamHeight+piezoHeig
ht,0),S,X,StressX
STORE,MERGE

NSOL,5,NODE(0,-
piezoLength,0),S,X,VoltP
STORE,MERGE

XVAR,1      ! 1: time
PLVAR,2,    ! 2: UY

XVAR,1      ! 1: time
PLVAR,3,    ! 3: Voltage Open

XVAR,1      ! 1: time
PLVAR,4,    ! 4: Stress on PZT

XVAR,1      ! 1: time
PLVAR,5,    ! 4: VOltage Close
```

Appendix V APDL script – Reduction factors of elastic load transfer design

```
FINISH
/CLEAR

/PREP7
StresX_S = 100E6

ET,101,SHELL63   !Dummy ET 101
R,101,1
MP,EX,101,5408   !Dummy MAT 101
MP,PRXY,101,0.3

ET, 1, SOLID186

MP,EX,1,69E9 ! aluminum alloy
MP,PRXY,1,0.3
MP,DENS,7780
rubberMatID=2

Young = 140E6
NU = 0.45
DENS = 1100

MP,EX,rubberMatID,Young
MP,PRXY,rubberMatID,NU
MP,DENS,rubberMatID,DENS

MP,EX,3,62E9  ! pzt 63e9
MP,PRXY,3,0.3
MP,DENS,7650

beamLength = 7.5E-2
beamHeight = 1.0E-2
beamWidth = 2.0E-2

piezoLength = 5E-2
piezoHeight = 0.5E-3
piezoWidth = 1E-2

adhHeight = 5E-3

K,1,-beamLength/2,0,beamWidth/2
K,2,-piezoLength/2,0,beamWidth/2
K,3,piezoLength/2,0,beamWidth/2
K,4,beamLength/2,0,beamWidth/2

K,5,-beamLength/2,0,piezoWidth/2
K,6,-piezoLength/2,0,piezoWidth/2
K,7,piezoLength/2,0,piezoWidth/2
K,8,beamLength/2,0,piezoWidth/2

K,9,-beamLength/2,0,-piezoWidth/2
```

```
K,10,-piezoLength/2,0,-piezoWidth/2
K,11,piezoLength/2,0,-piezoWidth/2
K,12,beamLength/2,0,-piezoWidth/2

K,13,-beamLength/2,0,-beamWidth/2
K,14,-piezoLength/2,0,-beamWidth/2
K,15,piezoLength/2,0,-beamWidth/2
K,16,beamLength/2,0,-beamWidth/2

A,1,2,6,5
A,2,3,7,6
A,3,4,8,7

A,5,6,10,9
A,6,7,11,10
A,7,8,12,11

A,9,10,14,13
A,10,11,15,14
A,11,12,16,15
AGLUE,ALL

LSEL,ALL
LSEL,S,TAN1,Z,0
LESIZE,ALL,piezoLength/72

LSEL,ALL
LSEL,S,TAN1,X,0
LESIZE,ALL,piezoWidth/12,,


ASEL,ALL
AATT,101,101,101
MSHAPE,0,2D
MSHKEY,1
AMESH,ALL

ASEL,S,LOC,Y,0
ESIZE,,10
VEXT,ALL,,,,beamHeight,
ALLSEL,ALL

ASEL,S,LOC,Y,beamHeight
ESIZE,,4
VEXT,ALL,,,,adhHeight,
ALLSEL,ALL

ASEL,S,LOC,Y,beamHeight+adhHeight
ESIZE,,4
VEXT,ALL,,,,piezoHeight,
```

```
ALLSEL,ALL
ACLEAR,ALL
ALLSEL,ALL

VSEL,S,LOC,Y,0,beamHeight
VSEL,R,LOC,X,-beamLength/2,beamLength/2
CM,BEAMVOLU,VOLU

VSEL,S,LOC,Y,beamHeight,beamHeight+adhHeight
VSEL,R,LOC,X,-piezoLength/2,piezoLength/2
VSEL,R,LOC,Z,-piezoWidth/2,piezoWidth/2
CM,ADHVOLU,VOLU

VSEL,S,LOC,Y,beamHeight+adhHeight,beamHeight+adhHeight+piezoHeight
VSEL,R,LOC,X,-piezoLength/2,piezoLength/2
VSEL,R,LOC,Z,-piezoWidth/2,piezoWidth/2
CM,PIEZOVOLU,VOLU

VSEL,ALL
CMSEL,U,BEAMVOLU
CMSEL,U,ADHVOLU
CMSEL,U,PIEZOVOLU
CM,VDELETED,VOLU

CMSEL,S,VDELETED
ESLV,S
VCLEAR,ALL
VDELE,ALL,,,1

! Modify correct ET and MP for
! FEM model
CMSEL,S,BEAMVOLU
ESLV,S
EMODIF,ALL,MAT,1
EMODIF,ALL,TYPE,1

CMSEL,S,ADHVOLU
ESLV,S
EMODIF,ALL,MAT,2
EMODIF,ALL,TYPE,1

CMSEL,S,PIEZOVOLU
ESLV,S
EMODIF,ALL,MAT,3
EMODIF,ALL,TYPE,1
! End of modifying correct ET and
! MP for FEM model
FINISH

/SOLU
NSEL,S,LOC,Y,0
D,ALL,UY,0
NSEL,ALL

NSEL,S,LOC,X,0
D,ALL,UX,0
NSEL,ALL

NSEL,S,LOC,X,0
NSEL,R,LOC,Y,0
D,ALL,UY,0
NSEL,ALL

NSEL,S,LOC,X,0
NSEL,R,LOC,Z,0
D,ALL,UZ,0
NSEL,ALL

NSEL,S,LOC,X,beamLength/2
!F,ALL,FX,5E6
F,ALL,FX,StresX_S*beamWidth*beamHeight
NSEL,ALL

NSEL,S,LOC,X,-beamLength/2
!D,ALL,UX,-5E-3
F,ALL,FX,-StresX_S*beamWidth*beamHeight

ALLSEL,ALL
SOLVE
FINISH

/POST1
ESEL,S,MAT,,2
PLNSOL, S,XZ, 0,1.0

ESEL,S,MAT,,3
PLNSOL, S,X, 0,1.0

PATH,path01,2,,20

! Define startpoint on the path
PPATH,1,,-piezoLength/2,beamHeight+adhHeight+piezoHeight,0

! Define endpoint on the path
PPATH,2,,piezoLength/2,beamHeight+adhHeight+piezoHeight,0
```

```
! Display x component of stress
! named "SX" along the path
PDEF,StresX_P,S,X
PDEF,StnX_P,EPEL,X

PLPATH,STRESX_P

/POST1
PATH,path02,2,,20

! Define startpoint on the path
PDEF,StnX_S,EPEL,X

PLPATH,STRESX_S
PPATH,1,,-beamLength/2,beamHeight/2,0

! Define endpoint on the path
PPATH,2,,beamLength/2,beamHeight/2,0

! Display x component of stress named "SX" along the path
PDEF,StresX_S,S,X
```

Appendix VI APDL script –Transient response of visco- load transfer design)

```
/CLEAR
/PREP7

ET,101,SHELL63   !Dummy ET 101
R,101,1
MP,EX,101,5408   !Dummy MAT 101
MP,PRXY,101,0.3

ET, 1, SOLID186

MP,EX,1,69E9 ! aluminum alloy
MP,PRXY,1,0.3
MP,DENS,7780

! visco-elastic material -- rubber
! solid
rubberMatID=2

Young = 140E6
NU = 0.45
DENS = 1100

MP,EX,rubberMatID,Young
MP,PRXY,rubberMatID,NU
MP,DENS,rubberMatID,DENS

*DIM,Gmod,ARRAY,2!Shear modulus

tau1= 0.4
tau2= 0.2

Gmod(1)     =     1/3
Gmod(2)     =     1/3

TB,PRONY,rubberMatID,,2,SHEAR
TBDATA,1,Gmod(1),tau1,Gmod(2),tau2

MP,EX,3,62E9  ! pzt 63e9
MP,PRXY,3,0.3
MP,DENS,7780

beamLength = 7.5E-2
beamHeight = 2.5E-2
beamWidth = 1.5E-2

piezoLength = 5E-2
piezoHeight = 0.5E-3
piezoWidth = 1E-2
piezoPosition =8E-2

adhHeight = 1E-3/10
```

```
K,1,-beamLength/2,0,beamWidth/2
K,2,-piezoLength/2,0,beamWidth/2
K,3,piezoLength/2,0,beamWidth/2
K,4,beamLength/2,0,beamWidth/2

K,5,-beamLength/2,0,piezoWidth/2
K,6,-piezoLength/2,0,piezoWidth/2
K,7,piezoLength/2,0,piezoWidth/2
K,8,beamLength/2,0,piezoWidth/2

K,9,-beamLength/2,0,-piezoWidth/2
K,10,-piezoLength/2,0,-
piezoWidth/2
K,11,piezoLength/2,0,-piezoWidth/2
K,12,beamLength/2,0,-piezoWidth/2

K,13,-beamLength/2,0,-beamWidth/2
K,14,-piezoLength/2,0,-beamWidth/2
K,15,piezoLength/2,0,-beamWidth/2
K,16,beamLength/2,0,-beamWidth/2

A,1,2,6,5
A,2,3,7,6
A,3,4,8,7

A,5,6,10,9
A,6,7,11,10
A,7,8,12,11

A,9,10,14,13
A,10,11,15,14
A,11,12,16,15
AGLUE,ALL

LSEL,ALL
LSEL,S,TAN1,Z,0
LESIZE,ALL,piezoLength/72

LSEL,ALL
LSEL,S,TAN1,X,0
LESIZE,ALL,piezoWidth/4,,


ASEL,ALL
AATT,101,101,101
MSHAPE,0,2D
MSHKEY,1
AMESH,ALL

ASEL,S,LOC,Y,0
ESIZE,,12
VEXT,ALL,,,,beamHeight,
```

```
ALLSEL,ALL

ASEL,S,LOC,Y,beamHeight
ESIZE,,4
VEXT,ALL,,,,adhHeight,
ALLSEL,ALL

ASEL,S,LOC,Y,beamHeight+adhHeight
ESIZE,,4
VEXT,ALL,,,,piezoHeight,
ALLSEL,ALL

VSEL,S,LOC,Y,0,beamHeight
VSEL,R,LOC,X,-
beamLength/2,beamLength/2
CM,BEAMVOLU,VOLU

VSEL,S,LOC,Y,beamHeight,beamHeight
+adhHeight
VSEL,R,LOC,X,-
piezoLength/2,piezoLength/2
VSEL,R,LOC,Z,-
piezoWidth/2,piezoWidth/2
CM,ADHVOLU,VOLU

VSEL,S,LOC,Y,beamHeight+adhHeight,
beamHeight+adhHeight+piezoHeight
VSEL,R,LOC,X,-
piezoLength/2,piezoLength/2
VSEL,R,LOC,Z,-
piezoWidth/2,piezoWidth/2
CM,PIEZOVOLU,VOLU

VSEL,ALL
CMSEL,U,BEAMVOLU
CMSEL,U,ADHVOLU
CMSEL,U,PIEZOVOLU
CM,VDELETED,VOLU

CMSEL,S,VDELETED
ESLV,S
VCLEAR,ALL
VDELE,ALL,,,1


! === Modify correct ET and MP for
FEM model === !
CMSEL,S,BEAMVOLU
ESLV,S
EMODIF,ALL,MAT,1
EMODIF,ALL,TYPE,1

CMSEL,S,ADHVOLU
ESLV,S
EMODIF,ALL,MAT,2
EMODIF,ALL,TYPE,1

CMSEL,S,PIEZOVOLU
ESLV,S
EMODIF,ALL,MAT,3
EMODIF,ALL,TYPE,1
! End of modifying correct ET
! and MP for FEM model
FINISH


/SOLU
ANTYPE,TRANS
TRNOPT,FULL
NLGEOM,ON
SSTIF,ON
ACEL,,,-9.81

ALPHAD,0
BETAD,0
DMPRAT,0.00005

! Mechanical BCs!
! BCs
NSEL,S,LOC,X,0
D,ALL,UX,0
NSEL,ALL

!NSEL,S,LOC,X,0
NSEL,S,LOC,Y,0
D,ALL,UY,0
NSEL,ALL

!NSEL,S,LOC,X,0
NSEL,S,LOC,Z,0
D,ALL,UZ,0
NSEL,ALL

ALLSEL,ALL
SAVE
! End of Mechanical BCs

! Sinusoidal excitations
freq = 1
! frequency of the sine wave

pi = ASIN(1)*2
dispamp = 1E0
!E-3! amplitude of the sine wave
!((2*pi*freq)^2)

T=1E-8
C=0
```

```
N=50
COUNTER=3.3/N

! Create Marco
*CREATE,LOAD
TIME,T

! Func. of Displacement
DISP=dispamp*SIN(2*pi*freq*T)

! Apply displacement loadings
NSEL,S,LOC,X,beamLength/2
F,ALL,FX,DISP
NSEL,ALL

NSEL,S,LOC,X,-beamLength/2
F,ALL,FX,-DISP
NSEL,ALL

T=T+COUNTER
C=C+1
OUTRES,ALL,ALL
ALLSEL,ALL
SAVE
SOLVE
*END
! === End of Marco

! === Active Macro with DO-ENDDO
LOOP
*DO,I,1,N+1
 *USE,LOAD
*ENDDO
! End of Sinusoidal excitations

FINISH
/POST26
ANSOL,2,NODE(0,beamHeight+adhHeigh
t+piezoHeight,0),S,X,StrsX_P,
STORE,MERGE

ANSOL,3,NODE(0,beamHeight+adhHeigh
t+piezoHeight,0),EPEL,X,StnX_P,

STORE,MERGE

NSOL,4,NODE(piezoLength/2,beamHeig
ht+adhHeight+piezoHeight,0),U,X,Di
spX_P,

STORE,MERGE

ANSOL,5,NODE(0,11*beamHeight/12,0,
),S,X,StrsX_S,
```

```
STORE,MERGE

ANSOL,6,NODE(0,11*beamHeight/12,0)
,EPEL,X,StnX_S,

STORE,MERGE

NSOL,7,NODE(piezoLength/2,beamHeig
ht,0),U,X,DispX_S,

STORE,MERGE

!ANSOL,8,NODE(7*piezoLength/20,bea
mHeight+adhHeight/2,piezoWidth/2),

S,XZ,ShrStrsXZ_A
!STORE,MERGE

!ANSOL,9,NODE(7*piezoLength/20,bea
mHeight+adhHeight/2,piezoWidth/2),
EPEL,XZ,ShrStnXZ_A

STORE,MERGE

ANSOL,8,NODE(0,beamHeight+adhHeigh
t/2,0),S,X,StrsX_Adh,

STORE,MERGE

ANSOL,9,NODE(0,beamHeight+adhHeigh
t/2,0),EPEL,X,StnX_Adh,

STORE,MERGE


XVAR,1      ! 1: TIME
PLVAR,2,    ! 2: Stress on PZT

XVAR,1      ! 1: TIME
PLVAR,3,    ! 3: Strain on PZT

XVAR,1      ! 1: TIME
PLVAR,4,    ! 4: Displ on PZT

XVAR,1      ! 1: TIME
PLVAR,5,    ! 5: Stress on
substrate

XVAR,1      ! 1: TIME
PLVAR,6,    ! 6: Strain on
substrate

XVAR,1      ! 1: TIME
```

```
PLVAR,7,    ! 7: Displ on
substrate


XVAR,8      ! 8: Stress on Adh
PLVAR,9,    ! 9: Strain on Adh

XVAR,9      ! 9: Strain on Adh
PLVAR,8,    ! 8: Stress on Adh
```

```
!XVAR,8     ! 10: Shear Stress on
Adh
!PLVAR,9,   ! 11: Shear Strain on
Adh

!XVAR,9           ! 11: Shear
Strain on Adh
!PLVAR,8,   ! 10: Shear Stress on
Adh
```

Appendix VII Inverse Laplace transform (Talbot method by Python)

```
import numpy as np
from pylab import*
from cmath import*
from matplotlib.ticker import MultipleLocator, FuncFormatter

rcParams['font.family']     = 'times new roman'
rcParams['font.size']       = 12
rcParams['lines.linewidth'] = 1.5
rcParams['legend.fontsize'] = 12
rcParams['xtick.labelsize'] = 12
rcParams['ytick.labelsize'] = 12

Ep = 62e9 # pzt-5;
nup = 0.3;
hp = 0.5e-3;
ha = 5e-3;
Gp = Ep/2/(1+nup)
Kp = Ep/(1-nup**2)
Es = 69e9 #aluminum alloy 6061; nus = 0.3; L = 0.05/2

def Talbot(t,N):
    h = 2*pi/N;
    shift = 0.0;
    ans =   0.0;

    if t == 0:
        print "ERROR:   Inverse transform can not be calculated for t=0"
        return ("Error");

    for k in range(0,N):
        theta = -pi + (k+1./2)*h;
        z = shift + N/t*(0.5017*theta*cot(0.6407*theta) - 0.6122 + \
           0.2645j*theta);
        dz = N/t*(-0.5017*0.6407*theta*(csc(0.6407*theta)**2)+ \
           0.5017*cot(0.6407*theta)+0.2645j);
        ans = ans + exp(z*t)*F(z)*dz;
    return ((h/(2j*pi))*ans).real

freq = 1.0;
Young_adh = 140e6;
NUA = 0.45;
ShearMod = Young_adh/2/(1+NUA)

alph1 = 1.0/3.0;
alph2 = 1.0/3.0;
alph3 = 0;
alph4 = 0
tau1 = 0.4;
tau2 = 0.2;
tau3 = 0;
tau4 = 0
```

```
def F(s):
    Ga = ShearMod*(1/s-alph1*(1/s-tau1/(tau1*s+1))-alph2*(1/s- \
      tau2/(tau2*s+1))-alph3*(1/s-tau3/(tau3*s+1))-alph4*(1/s- \
      tau4/(tau4*s+1)))
    alpha = sqrt(s*Ga/hp/ha/Kp)
    return ((1-1/cosh(alpha*L))*(2*pi*freq/(s*s+(2*pi*freq)*(2*pi*freq))))

def cot(phi):
    return 1.0/tan(phi)

def csc(phi):
    return 1.0/sin(phi)

time = np.arange(1e-4,3.3*(1/freq),0.05)
y1   = zeros(len(time))
y2   = zeros(len(time))

# Laplace inversion
for i in range(len(time)):
    y1[i] = Talbot(time[i],144)
    y2[i] = 1.*real((sin(2*pi*freq*time[i])))
figure('Result')

grid(True)
plot(y2,y1,'k-',label='inv')

xlabel("Normalized stress on substreate [MPa/MPa]")
ylabel("Normalized stress on piezo ceramic [MPa/MPa]")
show()
```